Optimization and implementation of emerging technologies to improve radiation therapy of head-and-neck cancer

Steven Michiels

Leuven
2020

KU Leuven

Biomedical Sciences Group
Faculty of Medicine

Department of Oncology
Laboratory of Experimental Radiotherapy

Optimization and implementation of emerging technologies to improve radiation therapy of head-and-neck cancer

Steven Michiels

Promotor: Prof. Tom Depuydt, ir., PhD
Co-promotors: Prof. Sandra Nuyts, MD, PhD
                      Prof. Kenneth Poels, PhD

Chair: Prof. Karin Haustermans, MD, PhD

Jury members:
Prof. Ria Bogaerts, PhD
Prof. Dirk Daelemans, ir., PhD
Prof. Harry van Lenthe, ir., PhD
Prof. Fréderic Duprez, MD, PhD (UGent)
Prof. Antony Lomax, PhD (ETH Zürich)

Dissertation presented in partial fulfilment of the requirements for the degree of Doctor in Biomedical Sciences

March 2020

Voor Julia en Aline

Table of contents

List of abbreviations

3D	Three-Dimensional
3D-CRT	Three-Dimensional Conformal RadioTherapy
3DPrIm	3D Printed Immobilization
μ_{tr}	Photon linear attenuation coefficient
ρ_e	Relative electron density to water
σ_{at}	Atomic mass cross section
σ_{el}	Electronic mass cross section
AAA	Anisotropic Analytical Algorithm
ASTM	American Society for Testing and Materials
ART	Adaptive RadioTherapy
CBCT	Cone-Beam Computed Tomography
CI	Conformity Index
CNN	Convolutional Neural Network
CT	Computed Tomography
CTV	Clinical Target Volume
$D_{x\%}$	Dose to x % of the volume
DCS	Dynamic Collimation System
DECT	Dual Energy Computed Tomography
DIR	Deformable Image Registration
DNA	DeoxyriboNucleic Acid
DOF	Degrees Of Freedom
FDM	Fused Deposition Modeling
FEM	Finite Element Analysis
FFF	Flattening Filter Free
$\Gamma_{3\%,\ 3mm}$	Gamma-index using 3% (local) dose difference and 3 mm distance-to-agreement criteria

GTV	Gross Tumor Volume
HA2	Dual-arc VMAT on HAlcyon
HA3	Triple-arc VMAT on HAlcyon
HI	Homogeneity Index
HNC	Head-and-Neck Cancer
HU	Hounsfield Units
ICRU	International Commission on Radiation Units and measurements
IGRT	Image-Guided RadioTherapy
I$_m$	Mean ionization energy for the medium m
IMPT	Intensity-Modulated Proton Therapy
IMRT	Intensity-Modulated RadioTherapy
kV	Kilovoltage
LAHNC	Locally Advanced Head-and-Neck cancer
Linac	LINear ACcelerator
MC	Monte Carlo
MCS	Multiple Coulomb Scattering
MLC	Multi-Leaf Collimator
MRI	Magnetic Resonance Imaging
MU	Monitor Unit
MV	MegaVoltage
NTCP	Normal Tissue Complication Probability
OAR	Organ-At-Risk
PBS	Pencil Beam Scanning
PET-CT	Positron Emission Tomography - Computed Tomography
PJ	PolyJet™
PLA	PolyLactic Acid
PT	Proton Therapy
PTV	Planning Target Volume

PTV$_{Boost}$	Planning Target Volume for the primary tumor and the positive neck
PTV$_{Elective}$	Planning Target Volume for the elective neck
PTV$_{Total}$	Total Planning Target Volume
PW	Plastic Water
QA	Quality Assurance
RBE	Relative Biologic Effectiveness
regROI	Region-OF-Interest used for the image registration
ROI	Region-Of-Interest
RS	Range Shifter
RT	RadioTherapy
RTT	Radiation Therapy Technologist
SIB	Simultaneous Integrated Boost
SLA	StereoLithogrAphy
SLS	Selective Laser Sintering
SOBP	Spread-Out Bragg Peak
SPR	Stopping Power Ratio
SSD	Source-to-Surface Distance
TB2	Dual-arc VMAT on TrueBeam
TCP	Tumor Control Probability
TM	Thermoplastic Mask
TPS	Treatment Planning System
TSM	Tissue Substitute Method
UICC	International Union Against Cancer
UV	Ultra-Violet
VMAT	Volumetric Modulated Arc Therapy
VOI	Volume-Of-Interest
Z$_{eff}$	Effective atomic number

Summary

External beam radiotherapy (RT) is considered a cornerstone in the treatment of head-and-neck cancer (HNC). The main goal of RT is to administer a sufficient dose to induce a cell killing effect in the targeted malignant cells, hereby maximizing tumor control, while limiting the dose to the healthy organs-at-risk (OAR), hereby minimizing radiation-induced toxicities. Enhanced geometric targeting has been crucial to reduce toxicities in photon beam RT of HNC, through technical developments such as radiation beam intensity-modulation and image-guided treatment delivery. The increased time demands of these more complex treatment approaches conflict with the under-provision of RT, however, such that improved time-efficiency of state-of-the-art photon beam RT of HNC is required. In addition, the dose distributions achievable with photon beam RT are ultimately limited by the governing exponential dose deposition profile, which advocates the implementation of alternative RT beam modalities. The absence of exit dose in intensity-modulated proton therapy (IMPT), for instance, due to the finite range of protons, could allow for improved OAR sparing compared with photon beam RT and may therefore reduce toxicities for a subpopulation of the patients with HNC. The relatively immature technique of IMPT, however, still requires optimization of many technologic and physical aspects, such as the lateral penumbra and the workflow efficiency when using a range shifter (RS) to treat superficial target volumes. This dissertation focusses on the optimization and implementation of emerging technologies to improve the abovementioned aspects in photon and proton beam RT of HNC.

Implementation of emerging O-ring linac technology may increase the time-efficiency of image-guided volumetric intensity-modulated arc therapy (VMAT) with photon beams. The encapsulation of the moving parts, namely, allows for higher gantry rotation speeds than with conventional C-arm linacs. In chapter II of this thesis, a fast-rotating O-ring linac was clinically implemented and compared with a C-arm linac in terms of plan quality and delivery time. For a cohort of 30 patients, treatment plans for VMAT of HNC on both systems were optimized, plan delivery accuracy was verified and plan delivery times were measured. The results show that for VMAT of HNC, the fast-rotating O-ring linac at least maintains the plan quality of dual-arc VMAT on a C-

arm linac while reducing the volumetric image acquisition and plan delivery time. The expected reduction in treatment time associated with the fast-rotating O-ring linac could increase clinical throughput of image-guided, highly conformal photon beam RT of HNC and could contribute to improved patient comfort in standard- or hyper-fractionated RT of HNC. In addition, the fast-rotating O-ring linac provides inherent availability of daily volumetric images, which could facilitate clinical deployment of adaptive RT of HNC.

IMPT of HNC may be optimized by using bolus RS, integrated within the patient immobilization. Such integrated device could reduce the spot size and the number of hardware manipulations – with collision risk – compared with conventional nozzle-mounted RS. In chapters III, IV and V of this thesis, the emerging manufacturing technology of 3D printing was implemented towards the realization of such device. Firstly, the normal tissue sparing with 3D printed, patient-specific bolus RS for IMPT of HNC was compared with nozzle-mounted RS using Monte Carlo based plan optimization. The results show clinically relevant toxicity reductions and thus motivate the development of patient-specific bolus RS for IMPT of HNC. Secondly, the suitability of 3D printing to achieve RS integrated patient immobilization was evaluated for a range of 3D printed materials and techniques. Dual-energy computed tomography based range shift predictions were verified with proton beam measurements, and mechanical stiffness measurements were performed before and after irradiation with a therapeutic dose. The results show a proof-of-concept for the use of 3D printed RS and immobilization in a clinical workflow. Thirdly, the feasibility of 3D printed immobilization (3DPrIm) was evaluated in a pilot study on patients with HNC, using weekly cone-beam computed tomography imaging and a patient questionnaire. The results show that 3DPrIm is feasible in terms of workflow, patient comfort and setup reproducibility. As such, with the implementation of 3D printing technology, important steps were taken towards a single, patient-specific device that achieves spot size reduction, hardware manipulation minimization and patient immobilization for IMPT of HNC. While the clinical implementation of such device is yet to be achieved, the enhanced toxicity reduction could increase the overall number of patients eligible for IMPT of HNC. Moreover, the potentially increased clinical throughput could facilitate the clinical evidence gathering for IMPT of HNC.

Samenvatting

Radiotherapie (RT) met externe bundels wordt beschouwd als een hoeksteen van de behandeling van hoofd- en halskanker (HHK). Het hoofddoel van RT is het toedienen van een voldoende dosis aan de kwaadaardige cellen om een celdodend effect te induceren, waardoor de tumorcontrole wordt gemaximaliseerd, terwijl de dosis aan de gezonde risico-organen zo veel mogelijk wordt beperkt, waardoor bestralingsgeïnduceerde toxiciteiten worden geminimaliseerd. Verbeterde geometrische doelgerichtheid is cruciaal gebleken om toxiciteiten in fotonenbundel RT van HHK te verminderen, door middel van technische ontwikkelingen zoals intensiteitsmodulatie van de bestralingsbundels en beeldgeleide toediening van de behandeling. De toegenomen tijdsvraag van deze meer complexe behandelingsbenaderingen is echter in strijd met het huidige onderaanbod van RT, zodat een verbeterde tijdefficiëntie van moderne fotonenbundel RT van HHK aangewezen is. Bovendien worden de met fotonenbundel RT realiseerbare dosisdistributies finaal beperkt door het heersende exponentiële dosisafzettingsprofiel, hetgeen pleit voor de implementatie van alternatieve RT bundelmodaliteiten. De afwezigheid van uitgangsdosis in intensiteitsgemoduleerde protonentherapie (IMPT), bijvoorbeeld, door het eindige bereik van protonen, laat mogelijk een verbeterd sparen van risico-organen toe met in vergelijking met fotonenbundel RT en zou derhalve bestralingsgeïnduceerde toxiciteiten kunnen verminderen voor een subpopulatie van de patiënten met HHK. De relatief immature techniek van IMPT vereist echter nog steeds optimalisatie van vele technologische en fysieke aspecten, zoals de protonenpenceelbundelgrootte en de werkstroom-efficiëntie bij het gebruik van een energie pre-absorbeerder of 'range shifter' (RS) voor de behandeling van oppervlak gelegen doelvolumes. Dit proefschrift richt zich op de optimalisatie en implementatie van opkomende technologieën om de bovengenoemde aspecten in fotonen- en protonenbundel RT van HHK te verbeteren.

Implementatie van opkomende O-ring lineaire versneller (linac) technologie kan de tijdsefficiëntie van beeldgeleide, volumetrisch intensiteitsgemoduleerde boogtherapie (VMAT) met fotonenbundels mogelijk verhogen. De inkapseling van de bewegende

delen zorgt namelijk voor hogere rotatiesnelheden van het bestralingstoestel dan bij conventionele C-arm linacs. In hoofdstuk II van dit proefschrift werd een snel roterende O-ring linac klinisch geïmplementeerd en vergeleken met een C-arm linac wat betreft plankwaliteit en toedieningstijd. Voor een cohorte van 30 patiënten werden behandelplannen voor VMAT van HHK op beide systemen geoptimaliseerd, werd de nauwkeurigheid van de plantoediening geverifieerd en werden de plantoedieningstijden opgemeten. De resultaten tonen aan dat voor VMAT van HHK, de snel roterende O-ring linac tenminste de plankwaliteit van twee-bogen VMAT op een C-arm linac handhaaft, terwijl de volumetrische beeldacquisitie en de plantoedieningstijd worden verkort. De verwachte reductie van de behandelingsduur geassocieerd met de snel roterende O-ring linac zou de klinische doorstroom van beeldgeleide, zeer conforme fotonenbundel RT van HHK kunnen verhogen en zou kunnen bijdragen aan een verbeterd patiëntencomfort in standaard- of hyper-gefractioneerde RT van HHK. Bovendien biedt de snel roterende O-ring linac inherente beschikbaarheid van dagelijks volumetrische beelden, wat het klinisch inzetten van adaptieve RT van HHK zou kunnen vergemakkelijken.

IMPT van HHK kan worden geoptimaliseerd met behulp van bolus RS, geïntegreerd in het patiëntimmobilisatiemateriaal. Een dergelijk geïntegreerd apparaat zou de protonenpenceelbundelgrootte en het aantal hardwaremanipulaties - met botsingsrisico – kunnen verminderen in vergelijking met een conventionele, op het bestralingstoestel gemonteerde RS. In hoofdstuk III, IV en V van dit proefschrift werd de opkomende productietechnologie van 3D-printen geïmplementeerd ter realisatie van een dergelijk apparaat. In eerste instantie werd het sparen van de normale weefsels met 3D-geprinte, patiëntspecifieke RS voor IMPT van HHK vergeleken met conventionele RS met behulp van op Monte Carlo gebaseerde planoptimalisatie. De resultaten tonen klinisch relevante toxiciteitsreducties en motiveren dus de ontwikkeling van patiëntspecifieke bolus RS voor IMPT van HHK. In tweede instantie werd dan de geschiktheid van 3D-printen ter realisatie van RS-geïntegreerd patiëntimmobilisatiemateriaal geëvalueerd voor een reeks 3D-geprinte materialen en technieken. Op duale-energie computertomografie gebaseerde predicties van protonenbereikverschuivingen werden geverifieerd met protonenbundelmetingen en mechanische stijfheidsmetingen werden uitgevoerd voor en na bestraling met een therapeutische dosis. De resultaten tonen een proof-of-concept voor het gebruik van

3D-geprinte RS en immobilisatiemateriaal in een klinische workflow. In derde en laatste instantie werd de haalbaarheid van 3D-geprinte patiëntimmobilisatie (3DPrIm) geëvalueerd in een pilootstudie bij patiënten met HHK, met behulp van wekelijkse volumetrische beeldvorming en een patiëntenvragenlijst. De resultaten tonen aan dat 3DPrIm haalbaar is in termen van werkstroom, patiëntencomfort en reproduceerbaarheid van de instelling van de patiënt. Als zodanig werden met de implementatie van 3D-printtechnologie belangrijke stappen gezet in de richting van een enkel, patiëntspecifiek apparaat dat reductie van de protonenpenceelbundelgrootte, minimalisering van hardwaremanipulatie en patiëntimmobilisatie voor IMPT van HHK realiseert. Hoewel de klinische implementatie van een dergelijk apparaat nog moet worden gerealiseerd, zou de verbeterde toxiciteitsreductie het totale aantal patiënten kunnen verhogen dat in aanmerking komt voor IMPT van HHK. Bovendien zou de potentieel verhoogde klinische doorstroom het verzamelen van klinische evidentie voor IMPT van HHK kunnen faciliteren.

CANCER IS A COMPLEX DISEASE IN WHICH AFFECTED CELLS OF THE BODY proliferate in an uncontrolled manner [1]. This disease is expected to rank as the leading cause of mortality in the current century and to be the most important barrier to increasing life expectancy worldwide [2]. According to the World Health Organization, cancer was responsible for the death of 9 million people worldwide in the year 2016 [3]. Five percent of these cancer-related deaths are attributed to head-and-neck cancer (HNC), a broad term that refers to a heterogeneous group of malignancies originating from the oral cavity, nasal cavity, paranasal sinuses, nasopharynx, oropharynx, hypopharynx and larynx, anatomic regions visualized in Figure 1 [4].
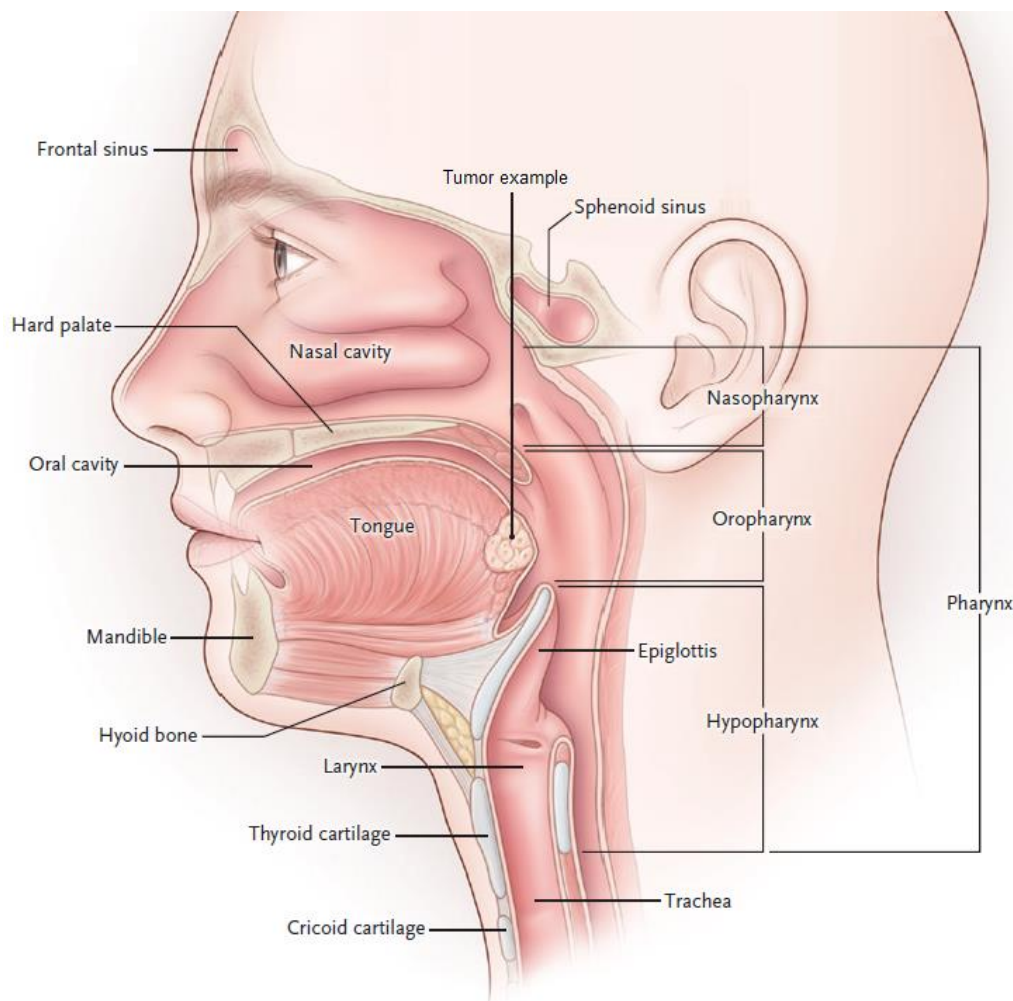

Figure 1. Visualization of the anatomic regions where head-and-neck cancer can originate from. Reproduced and adapted with permission from [5], Copyright Massachusetts Medical Society.

Pathologic diagnosis of HNC is performed based on a surgical biopsy sample. Type and extent of the disease largely determines the prognosis of an individual patient and is assessed by staging. HNC staging takes into consideration anatomic subsite, tumor size, cervical lymph node involvement and the presence of distant metastasis [6,7]. Routine staging activities involve physical examination, chest X-ray or computed tomography (CT), head-and-neck endoscopy and head-and-neck CT or magnetic resonance imaging (MRI) [8]. The treatment decision is then made by the multidisciplinary oncology board of the treating center.

Treatment of HNC may consist of surgery, chemotherapy, radiotherapy (RT), immunotherapy or a selected combination of these modalities [9]. The use of a single modality, i.e. surgery or radiotherapy, can achieve fairly high local control and overall survival in the case of early-stage disease [8,10–13]. The majority of patients with HNC, however, present with loco-regionally advanced disease at the time of diagnosis [8,14]. Generally, for these later-stage cases a combined modality treatment is selected, consisting of either definitive RT with concomitant chemotherapy or cetuximab (a monoclonal antibody targeting the epidermal growth factor receptor), or surgery followed by adjuvant (chemo-)RT [6,8,11,15–19]. Overall, it is estimated that RT forms part of the treatment for 75% of patients with HNC [20,21].

RT uses ionizing radiation to pursue eradication of the malignant cells. External beam RT is the type of RT most commonly used for the treatment of HNC. In this technique, the ionizing radiation is administered to the patient using an external source of high-energy waves or particles. As these waves or particles interact with the body tissues, damage is inflicted to the cells' DNA, which may or may not be lethal [22]. The cell damaging effect of ionizing radiation, however, does not differentiate between malignant cells and normal tissue cells. Nevertheless, the biologic outcome of each irradiated cell is affected by several factors, such as the cell type and the associated radio-sensitivity, the dose received per fraction, the total dose and the total time in which the RT course is administered [23–25]. The clinical outcome at the level of the patient can be predicted by means of dose-volume models for tumor control probability (TCP) and normal tissue complication probabilities (NTCP) [26–29]. Common normal tissue complications – or toxicities – associated with RT of HNC are xerostomia and dysphagia [30]. The main goal of RT is to administer a sufficient dose to induce a cell

killing effect in the targeted malignant cells, hereby maximizing tumor control, while limiting the damage to normal cells, hereby minimizing radiation-induced toxicities.

I.1 Radiotherapy of head-and-neck cancer

I.1.1 Radiotherapy prescription

Following the decision for RT from the multidisciplinary oncology board, the treating physician sees the patient on consultation and determines the dose prescription, which depends on tumor stage and location, treatment intent and selected treatment approach [31]. Specifically for HNC, the administration of RT in several fractions of relatively low dose is known to improve the repair capability of normal tissue cells relative to that of malignant cells [23–25]. For definitive (chemo-)RT of locally advanced head-and-neck cancer (LAHNC), a commonly used prescription is a therapeutic dose of 70 Gy, to be delivered in fractions of 2 Gy to the primary tumor volume and pathologic lymph nodes. Additionally, a prophylactic dose of 54.25 Gy, to be simultaneously delivered in fractions of 1.55 Gy, is prescribed to the lymph nodes which are considered to be unaffected but which are at risk for harboring subclinical disease, the so-called elective lymph nodes [32]. Submission of the physician's dose prescription is then followed by the treatment preparation phase.

I.1.2 Treatment preparation

I.1.2.1 Planning CT acquisition

The first step of the treatment preparation phase consists of the creation of a digital model of the patient. To this end, a CT-scan of the patient in treatment position is acquired, commonly referred to as the reference or planning CT. This planning CT is used for all subsequent steps in the treatment preparation phase. Physician approval of the treatment plan prior to actual treatment, hence, assumes that the planning CT is representative of the patient's anatomy during the delivery of all treatment fractions. Minimization of any differences between the planned and the actually delivered treatment therefore requires the planning CT to be acquired with the patient in a position that is both reproducible and stable, i.e. with minimal inter- and intra-fractional variation, respectively [33–36]. A common way to pursue this in RT of HNC is by positioning the patient in supination, by means of a standard or customized headrest and a 5-points thermoplastic mask [35,37–39]. Any of these patient-specific

immobilization devices are molded around the patient's body outline before acquisition of the planning CT (see Figure 2). Based on the acquired planning CT, a localization point is then defined by the attending physician, preferably centrally in the primary tumor. The localization point is stored in the treatment planning software (TPS) as the initial isocenter of the treatment plan, projected onto the patient using the laser system present and marked on the immobilization mask, as a reference for patient setup during each treatment session.
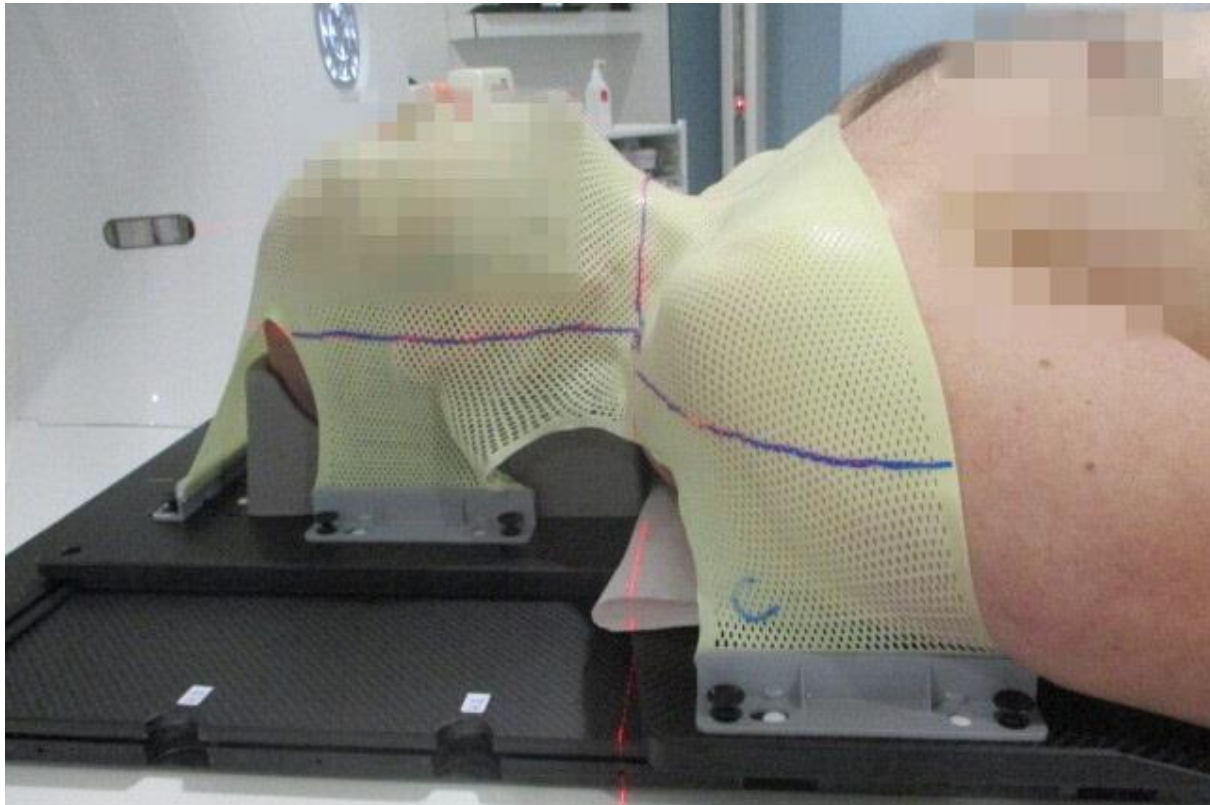

Figure 2. Picture of a patient with head-and-neck cancer during acquisition of the planning CT. A 5-points thermoplastic mask, molded around the patient's body outline, is used for stable and reproducible patient positioning. The localization point is marked on the mask as a reference for patient setup during each treatment session. Patient-specific characteristics have been censored for reasons of privacy.

I.1.2.2   Delineation of target volume(s) and organs at risk

The second step of the treatment preparation phase comprises the delineation of the anatomic structures relevant to the treatment planning. In this delineation process, the physician first contours the primary and/or the nodal gross tumor volume (GTV). To this end, both clinical information and additional imaging such as MRI and positron emission tomography-CT (PET-CT) gathered during pre-treatment work-up are used [8, 31]. Subsequently, the GTV is expanded to include microscopic extension of the

tumor with correction for natural anatomic boundaries [40–42]. The resulting high-risk clinical target volume (CTV) is then given a therapeutic dose prescription. Additionally, elective lymph node levels are selected for delineation depending on the primary tumor stage and location [41]. The resulting low-risk CTV is given a prophylactic dose prescription [43]. Organs-at-risk (OAR), such as the parotid glands, pharyngeal constrictor muscles and oral cavity, are delineated as well [44]. As dose-effect relationships are known for these OARs, such as the probability of xerostomia in function of the contralateral parotid gland, sparing of these OARs is pursued to limit NTCPs related to the treatment [28,29]. The typical complexity of the anatomy in RT of LAHNC, however, with large, complex-shaped target volumes in close proximity to several OARs as shown in Figure 3, often results in a compromise between fulfilling the target dose prescription and reducing the dose to OARs.
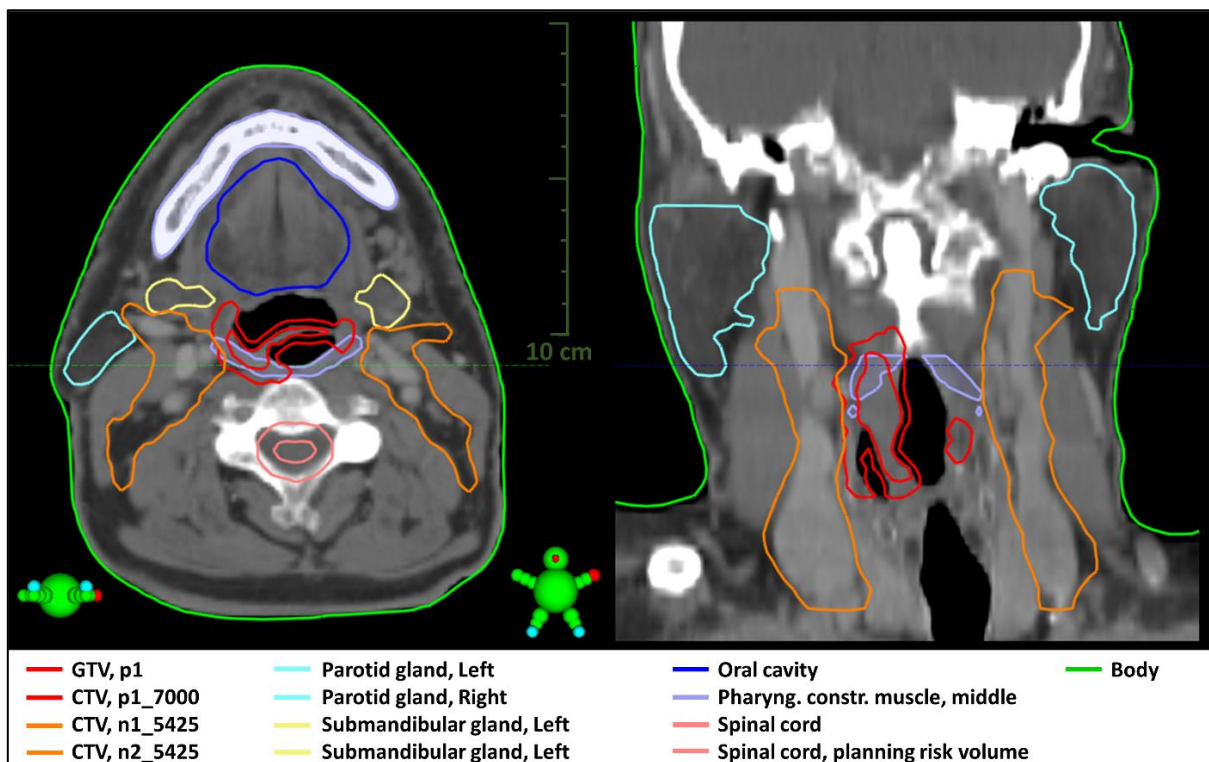

GTV, p1	Parotid gland, Left	Oral cavity	Body
CTV, p1_7000	Parotid gland, Right	Pharyng. constr. muscle, middle	
CTV, n1_5425	Submandibular gland, Left	Spinal cord	
CTV, n2_5425	Submandibular gland, Left	Spinal cord, planning risk volume	

Figure 3. Visualization of an axial (left) and a coronal (right) slice of the planning CT for a patient with a locally advanced tumor of the supraglottic larynx. The GTV and the associated high-risk CTV are delineated in red. The low-risk CTV, consisting of the elective lymph nodes, is delineated in orange. A number of important organs-at-risk are delineated as well: the parotid glands, submandibular glands, oral cavity, middle pharyngeal constrictor muscle and the spinal cord.

I.1.2.3 Treatment planning

The third step of the treatment preparation phase constitutes the creation of a patient-specific treatment plan, using the anatomic information acquired in the previous steps. The used software, the TPS, contains validated beam models and associated dose calculation engines for the external beam RT modalities available at the treating center, such as electron, photon and proton beams [45,46]. Treatment planning then consists of selecting an external beam RT modality that is suitable for the clinical case under consideration and subsequently optimizing the expected dose distribution, by directing the selected beam towards the target volume from one or more angles, shaping and/or modulating the beam. As such, the degrees of freedom for the different machine settings are optimized in order to meet the physician's target dose prescription while sparing the OARs as much as achievable.

Dealing with geometric uncertainties

The anatomic information used during treatment planning is known to be subject to geometric uncertainties. The definition of the CTV in the treatment preparation phase, for instance, contains geometric uncertainties due to variability in the delineation process [47,48]. In addition, the patient's anatomy during treatment delivery deviates from the anatomy used for treatment planning, for example as a result of daily setup variations during treatment [34,36]. To prevent these geometric uncertainties to result in geographic misses, i.e. part of the CTV not receiving the prescribed dose due to these geometric uncertainties, treatment planning and evaluation is performed based on an auxiliary planning target volume (PTV), consisting of the CTV isotropically expanded with a margin [49]. Alternatively, different error scenarios may be directly included in the treatment plan optimization process, to minimize for instance the deviation of the worst case with so-called minimax robust optimization [50–52].

Beam modalities and treatment techniques

Figure 4 shows characteristic depth-dose curves for typically used modalities for RT of HNC, such as electron beams and photon beams, produced with a linear accelerator (linac), and proton beams, for instance produced with a cyclotron. Photons, being uncharged, exhibit an increasing dose deposition in a build-up region, after which the dose deposition exponentially decays with depth. Electrons and protons, being

charged, exhibit an exit dose that is largely reduced or even absent, respectively. The distal fall-off for protons is much sharper than for electrons. In addition, protons of clinically used energies are able to penetrate much deeper into tissue than electrons [53].
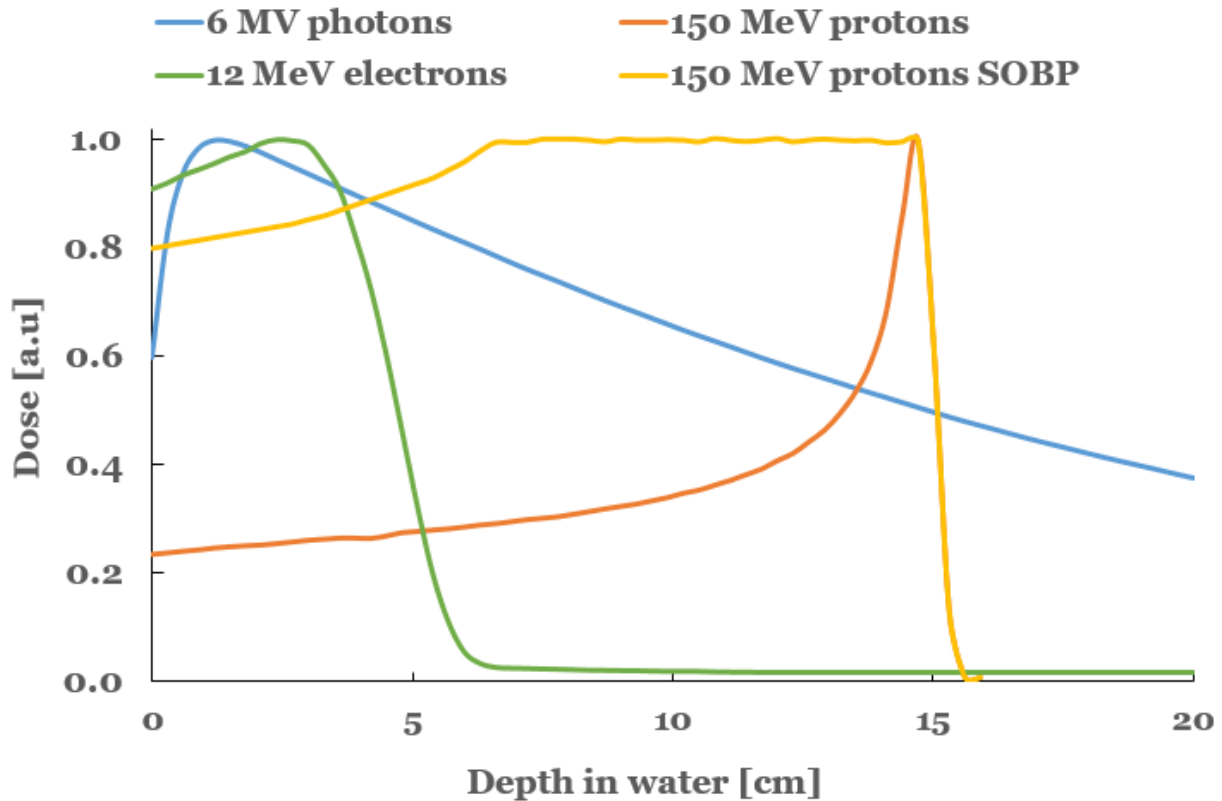

Figure 4. The shape of the depth-dose curves considerably differs between a 6 MV flattened photon beam (blue), a 12 MeV electron beam (green), a pristine Bragg peak of quasi-mono-energetic 150 MeV protons (red) and a proton spread-out Bragg peak (yellow), composed of multiple pristine Bragg peaks (yellow). *Abbreviation:* SOBP = spread-out Bragg peak.

Electron beam RT is a relatively simple technique that allows to treat superficial tumors with minimal dose to the underlying normal tissue, due to the high dose at the body entrance and the relatively steep dose fall-off beyond. The penetration depth achieved with common beam energies (up to 20 MeV), however, is only a few centimeters. In addition, routine field shaping to conform to the target is restricted to the use of patient-specific aperture blocks. Therefore, the use of electron beams in RT of HNC is limited to the treatment of target volumes at shallow depth and of simple geometry, that do not require any beam modulation to spare OARs in the vicinity [54,55].

RT of more complex-shaped, extended target volumes in close proximity to a large number of OARs, as often encountered in HNC, requires the use of more deeply penetrating beams such as photon beams, directed to the target from multiple angles. In three-dimensional conformal radiotherapy (3D-CRT) with photons, each field is conformed to the beam's eye view with a multi-leaf collimator (MLC), consisting of a large number of leaf pairs for which the positon can be independently controlled. Improved OAR sparing in RT of HNC can be achieved, however, by using the MLC to vary the photon intensity – or fluence – within each incident field in function of the position in the field aperture [56,57]. The basic idea of such intensity-modulated radiotherapy (IMRT) is to subdivide each field into smaller segments and to reduce the intensity of rays going through particular OARs while increasing the intensity of rays that primarily 'see' the target volume [49,58]. Although each beam intentionally delivers a non-uniform intensity to the target, the desired dose distribution in the target is achieved after superimposing all fields from the different directions [58]. Faster delivery of highly-conformal, intensity modulated photon beam RT of HNC can be achieved with volumetric modulated arc therapy [59]. In this technique, the photon fluence is dynamically shaped while rotating the gantry of a C-arm linac around the patient, by continuously adjusting the gantry speed, MLC leaf positions and the dose rate [60]. Figure 5 shows the dose distribution for a VMAT plan clinically delivered to treat a patient with LAHNC.
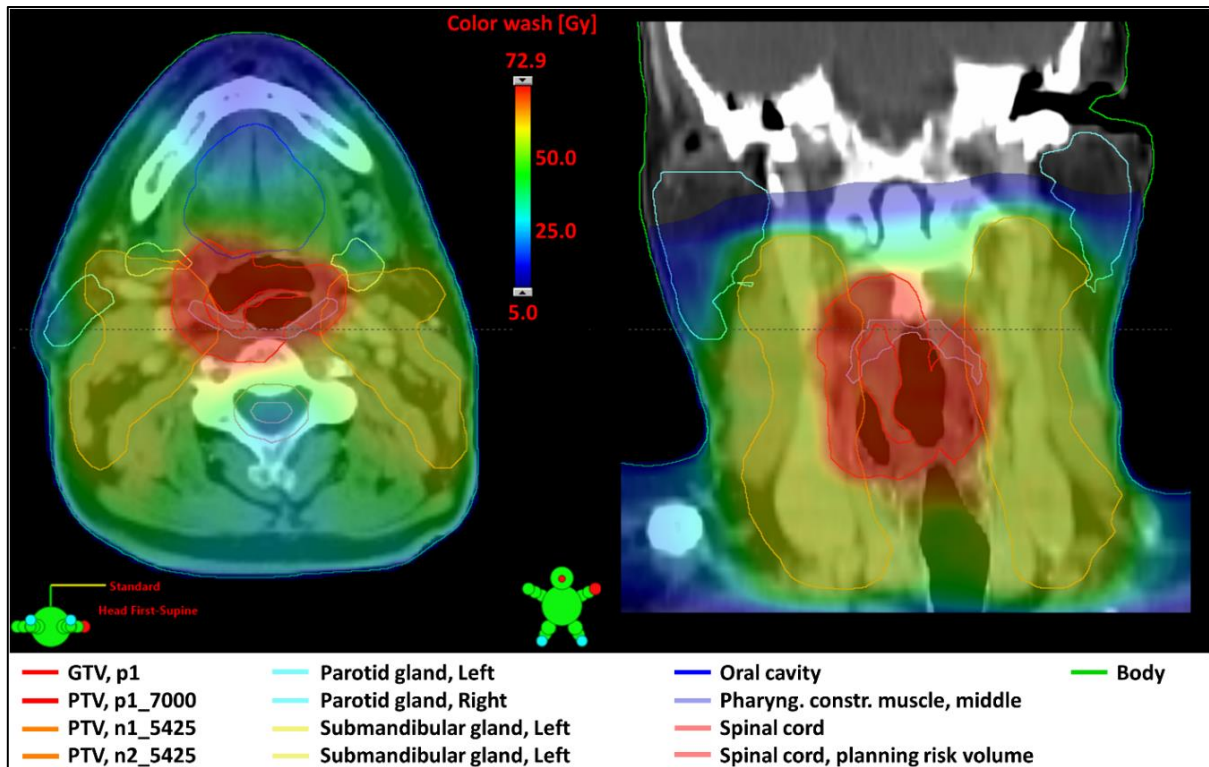
Figure 5. Visualization of the dose distribution for the clinical volumetric modulated arc therapy (VMAT) plan created for the case shown in Figure 3. The dose prescription was 70 Gy in fractions of 2 Gy to the primary CTV and 54.25 Gy in fractions of 1.55 Gy to the elective CTV. A CTV-to-PTV margin of 5 mm was used.

Further reduction of the volume of irradiated normal tissue in RT of HNC can be expected using proton therapy (PT), due to the favorable depth dose characteristics of proton beams compared to photon beams [61,62]. In intensity-modulated proton therapy (IMPT) with pencil beam scanning (PBS), thousands of small proton pencil beams – or spots – are delivered to the tumor one by one. The depth at which these spots are deposited, is selected layer-by-layer by varying the energy of the proton beam. The lateral position of the spots within a layer is adjusted by magnetically deflecting the proton beam with scanning magnets. The local intensity of each of these spots is controlled by the time during which the pencil beam resides at each target position [63]. As such, by varying the position and the intensity of all the spots, the dose can be conformed tightly to the tumor shape without any exit dose for each field. The actual range of the protons within the patient, however, is highly sensitive to the thickness and the physical properties (specifically the stopping power [64]) of the traversed tissues. The particular dose deposition profile of protons, therefore, is subject to both setup and range uncertainties, which requires thorough mitigation [65–68]. Added to that, the potential improvement in OAR sparing of IMPT is partly limited by the pencil

beam spot size achieved by current PT technology [68–72]. Also, current PT systems are substantially more expensive than photon beam systems, such that cost-effectiveness has yet to be realized [73]. Moreover, the dosimetric advantage of IMPT has yet to be shown to translate into an effective reduction of side-effects [74–77].

Given that broader adoption of PT thus may require further maturation and optimization of the technology [68–72] and increased clinical evidence [74–77], photon beam VMAT may still be considered the current standard for RT of HNC [78–80]. Nevertheless, PT can be the selected treatment modality in the setting of a randomized clinical trial [74,75], based on a plan-comparison suggesting clinically relevant NTCP reductions [76,77,81] or based on insurance coverage policy [82].

Treatment plan optimization

Treatment planning for relatively simple treatment techniques can be performed with basic forward planning. In 3D-CRT with photons, for instance, the relative contribution of each field is manually adjusted after each evaluation of the dose distribution in an iterative process. The greatly increased number of degrees of freedom for advanced intensity-modulated treatment techniques such as IMRT/VMAT and IMPT, however, can only be managed by computerized inverse planning. Such inverse planning is driven by optimization objectives, which are representative of the clinical goals and are introduced by the user for each target and for each considered OAR. The computerized algorithm then iteratively adjusts the different parameters specific to the treatment technique until an optimal dose distribution is found [49,58]. For VMAT of HNC, for instance, these parameters are the gantry speed, MLC leaf speed and dose rate in function of the time. For IMPT of HNC, these parameters are the intensities, energies and lateral positions of the different spots to be delivered. Robust optimization of HNC IMPT involves optimization of the spot intensities and positions while taking into account predefined setup and range errors, in such a way that the optimization objectives are still met for these errors scenarios [50,52].

Treatment plan quality assurance

The result of the optimization process is a physician-approved treatment plan, containing the treatment machine settings capable of delivering the intended dose

distribution to the patient. Before treatment of a patient with an approved treatment plan, however, it is recommended to verify that the planned dose distribution can be actually delivered with sufficient accuracy by the treatment machine [49]. To this end, the clinical plan is recalculated and delivered to a phantom containing one or more radiation detectors. The degree of agreement between measurement and calculation is then evaluated and compared with the clinically accepted tolerance [83].

I.1.3   Treatment delivery

Image-guided radiotherapy

For the actual treatment delivery, the patient is positioned on a daily basis on the treatment couch using the immobilization devices created prior to the acquisition of the planning CT. Initial setup is performed by aligning the localization points on the immobilization mask with the lasers mounted in the treatment room. The localization points on the immobilization mask mark the isocenter as defined during treatment planning, whereas the lasers project onto the treatment machine isocenter. Hence, the initial setup procedure intends to reproduce the patient's position at the time of the planning CT acquisition and to align the target with the planned treatment beam.

Despite the use of immobilization devices in combination with a standard patient setup protocol, variations between the patient's position during daily treatment delivery and during planning CT acquisition do occur [34,36]. Image-guidance prior to delivery is an effective method to reduce the magnitude of these setup errors and thus to reduce the associated margins that prevent geographic misses [84,85]. In image-guided radiotherapy (IGRT), the initial setup is followed by X-ray imaging of the patient. The acquired images are rigidly registered with the planning CT or planning CT-derived images using a global region-of-interest (ROI) that contains the relevant anatomy [34,86]. Based on the performed image registration, a correction vector is calculated to further align the patient's treatment position with respect to the position on the planning CT. One possible image-guidance modality is the megavoltage (MV) treatment beam itself of a linac, in combination with a detector mounted opposite to the linac head by means of an insertable and retractable support arm. Improved contrast can be obtained with a kilovoltage (kV) X-ray tube-detector pair, mounted stationary in the treatment room or attached to the treatment machine. The use of combined planar imaging allows for corrections mostly based on the visualization of

bony anatomy. An on-board source-detector pair, however, can be used to obtain volumetric imaging as well, using cone-beam CT (CBCT) or fan-beam CT , which allows for corrections obtained from soft-tissue information [84]. The obtained correction vector is then applied by means of translation and possibly also rotation of the treatment couch.

Reproducible positioning of a large, flexible anatomic region such as in locally advanced HNC can be considered challenging, but has been facilitated by the use of immobilization in combination with daily volumetric image-guidance. Nevertheless, residual setup errors remain present [34,86,87], the magnitude of which directly impacts the required CTV-to-PTV margins. For the image-guided delivery of current highly conformal treatment techniques such as VMAT, a PTV margin of 3 to 5 mm is commonly used [51,88–90]. For IMPT of heterogeneous sites such as HNC, however, the use of a PTV margin is considered sub-optimal, as the underlying assumption of a rigid shift of the dose distribution in case of setup errors is not valid [50,52]. In appropriate robust optimization for IMPT of HNC, a setup error robustness setting of 3 to 5 mm likewise is commonly used [52,65,91,92]. In any case, either approach to ensure robustness of the target coverage against geometric uncertainties such as setup errors results in an increase of the normal tissue volume irradiated. Any effort to improve the patient setup accuracy, for instance by improving the quality of the immobilization, may therefore positively affect patient's outcome [52,89,90,93].

Anatomic deformations and adaptive radiotherapy

Couch movements for patient alignment in IGRT of HNC are typically based on a rigid registration that makes use of a large, global ROI. Within the considered anatomy, however, different smaller sub-ROIs can be identified, such as the occiput bone, mandible and cervical vertebrae, each of which can translate and rotate with respect to each other. The associated daily variations in posture may result in varying distances and orientations between the different sub-ROIs [34,86,87,94]. Such type of geometric variations is referred to as anatomic deformations. Besides changes in posture, other important sources of anatomic deformation have been identified during the RT treatment course of HNC, such as weight loss and tumor regression but also shrinkage of the lymph nodes and parotid glands [95–98].

The initial treatment plan is based on a single planning CT, which merely represents a snapshot of the anatomy, i.e. only one posture and only the anatomy prior to the treatment. Use of the initial treatment plan in the presence of the described anatomic deformations likewise deforms the actually delivered dose distribution, which may result in overdosage of OARs such as the parotid glands or underdosage of the target volumes [98–101]. Such dosimetric effects due to anatomic deformations may be even more pronounced in IMPT due to its increased sensitivity to uncertainties [102].

Adaptive radiotherapy (ART) is a widely proposed approach to mitigate the described dosimetric effects, by means of treatment plan adaptation using imaging that captures the patient-specific anatomic deformations throughout the treatment course [65,91,97,103–109]. Treatment plan adaptation may be based on repeated CT-imaging throughout the treatment course or may use the anatomical information captured during daily volumetric image-guidance. Clinically relevant benefits, however, may only be achieved for a selection of the considered patients. In addition, ART is still considered a labor- and equipment-intensive approach. General consensus is that broad clinical application of ART requires further optimization of adaptation frequency and timing, patient selection and workflow efficiency [97,100,110,111].

I.2 Emerging technologies to improve head-and-neck cancer radiotherapy

In the past few decades, substantial improvements in the efficacy of RT for HNC have been realized. Loco-regional control and survival rates have been increased through treatment intensification strategies, such as altered fractionation schedules and/or concomitant chemotherapy [15,18,19]. Treatment-related side-effects have been decreased by reducing the dose to healthy OARs. This has been achieved by the steeper dose gradients and the reduced safety margins allowed by technological advances such as intensity modulation [56,57] and volumetric image-guidance [89,90], respectively. Nevertheless, the outcome of patients with LAHNC remains relatively poor, with 5-year overall survival rates not exceeding 50% [15,17]. In addition, acute and late toxicities such as xerostomia and dysphagia remain frequent, with significant impact on patients' quality of life [112,113]. Further advances in both radiation biology and radiation oncology technology, therefore, are considered crucial to improve outcomes [25,114,115]. This thesis focusses on advances in radiation oncology technology,

specifically the optimization and implementation of emerging technologies to improve photon and proton beam RT of HNC.

I.2.1 Implementation of a fast-rotating O-ring linac for VMAT of HNC

Conventional C-arm linear accelerators (linac), with gantry-mounted, extendable devices for image-guidance, have been making up the bulk of radiotherapy treatment machines since long [116]. In recent years, these C-arm linacs have been gradually supplemented by O-ring systems, the geometry of which allows for designs with distinct technological features [117,118]. O-ring gantry designs for instance are allowed to rotate at higher speeds than the one rotation per minute of conventional C-arm linacs, due to the encapsulation of the moving parts. Such encapsulation also could achieve continuous readiness of image-guidance devices, without the need to insert and retract associated support arms. O-ring linac systems thus may be optimized for increased time-efficiency of IGRT.

Increased time-efficiency may increase the adoption rate of highly conformal IGRT. Indeed, while the use of image-guided, highly conformal RT has been shown crucial to reduce treatment-related toxicities [56,89], IGRT in an hyper-fractionated setting may be considered time-consuming, which limits the number of patients treated per machine. At the same time, the actual utilization of RT already is significantly lower than the optimal use, for instance due to shortage of resources. As the need for RT will continue increasing, this field of tension between quality and time-efficiency can be expected to become even more pronounced [119–121]. The clinical implementation of a fast-rotating O-ring linac, optimized for fast image-guidance and treatment delivery, is discussed in chapter 2 of the thesis.

I.2.2 Optimization of IMPT for HNC

Despite the advances in outcome achieved so far with photon beam VMAT of HNC, acute and late toxicities remain extensive, with significant impact on the patients' quality of life [112,113]. In this regard, the use of charged particles such as protons is highly promising, as their finite range and the sharp dose fall-off may offer improved OAR sparing compared to state-of-the-art photon beam VMAT [72]. For the often complex geometries of HNC, with close proximity of various OARs to the target

volume, this improved conformity of IMPT may reduce treatment-related side-effects for a subpopulation of the patients [76,77,81].

The potential advantage of PT has been recognized already since 1946 [122]. A few decades later, the use of PBS to deliver IMPT was clinically introduced in dedicated facilities [123]. Nevertheless, only since the past few years more broad clinical adoption of IMPT has been emerging [124,125]. Indeed, the increased costs associated with IMPT highlights the need for rationalized use for non-standard indications such as LAHNC [76,77,81]. In addition, full realization of the potential of IMPT is generally acknowledged to still require optimization of many technologic and physical aspects [68,70,72]. Predominant issues such as spot size minimization [69,71], treatment delivery workflow efficiency [68,70,72] and treatment delivery uncertainties [65], for instance, may be effectively dealt with through increased treatment individualization using patient-specifically manufactured devices, which is discussed in the following chapters.

I.2.2.1   Patient-specific bolus range shifter for spot size reduction in IMPT of HNC

Modern PBS systems are limited in the minimal energy hence depth at which they can deliver spots, typically around 4.1-7.7 cm depth in water. IMPT of more superficial target volumes, such as in LAHNC, requires a pre-absorbing range shifter (RS), which is typically attached to the nozzle. The air gap between the nozzle-mounted RS and the patient however is known to compromise the spot size [126–129] and therefore the dose conformity of IMPT [68–72]. To minimize these air gap effects, the RS is often positioned as close as possible to the patient using a movable snout extension. Air gap minimization in IMPT of LAHNC, however, requires careful attention to avoid any collision and moreover is often prevented due to the presence of curved geometries combined with large target volumes. Novel solutions for individualized, on-skin 'bolus' RS would avoid the detrimental effect of air gaps, hereby optimizing the potential OAR sparing in IMPT for LAHNC. The clinical benefit of such approach is shown in chapter 3 of the thesis.

I.2.2.2 Implementation of 3D printing to create patient-specific devices in IMPT of HNC

Patient-specific bolus RS could be realized using 3D printing, an emerging manufacturing technology with a high degree of flexibility in object creation through a layer-by-layer shaping process. 3D printing is already in clinical use for the creation of bolus in electron beam RT [130]. When considering clinical implementation of bolus RS for IMPT, the sensitivity of the proton range to the thickness and the stopping power of the traversed materials requires detailed consideration. Part of chapter 4 of the thesis therefore describes an in-depth characterization of the geometrical and proton beam modifying properties of possible 3D printed materials and techniques for bolus RS. Moreover, the clinical use of 3D printed materials for bolus RS requires reliable quality assurance that fits within the clinical workflow. To this end, a potential work-up for the clinical use of 3D printed RS is investigated as well in chapter 4: from the material printing to in-house prediction of the beam modification properties, with a verification through proton beam measurements. Lastly, bolus RS may be 3D printed as an individual add-on or may be 3D printed together with the patient immobilization. The latter, integrated approach would ensure presence and correct placement of the RS for each treatment field and may simplify the overall IMPT delivery workflow by reducing the number of hardware manipulations. Such integrated device, however, would have a mechanical functionality as well, besides proton beam modifying functionality. The remaining part of chapter 4, therefore, elaborates on mechanical characterization of 3D printed materials and techniques.

Along with realization of bolus RS integration, 3D printed immobilization may offer enhancements with respect to the currently used thermoplastic masks. Certain types of these masks, namely, are known to shrink after the initial application, which can cause patient discomfort and reduce patient-specificity [131]. Also, substantial residual inter-fractional variations in patient positioning have been reported [36]. While the impact of these setup variations on the target coverage is typically minimized using robust treatment planning, plan robustness does have a significant cost in terms of OARs dose [52]. The potentially increased patient-specificity of 3D printed immobilization may reduce inter-fractional setup variations and hence could optimize the OAR sparing in IMPT of LAHNC.

Combined with the integration of RS bolus, 3D printed immobilization may reduce the spot size, the number of hardware manipulations – with collision risk – and the treatment delivery uncertainties in IMPT of HNC using a single, patient-specific device. The proposed method of immobilization, however, differs greatly from the widely adopted method using thermoplastic masks. Indeed, immobilization masks are molded in the physical presence of the patient, whereas 3D printed immobilization is to be created offline based on any captured information on the patient's anatomy. In addition, tolerability and comfort cannot be assumed given the novelty of the proposed immobilization technique. In chapter 5 of the thesis, a pilot study of 3D printed immobilization on patients with HNC is performed, in order to prove feasibility of the proposed immobilization approach.

I.3 Summary of general aim and specific objectives

The general aim of this thesis is to improve RT of LAHNC by the optimization and the implementation of emerging technologies. To this end, the clinical implementation of a system optimized for fast image-guidance and treatment delivery of highly conformal photon beam VMAT is discussed. In addition, optimization of the promising proton beam IMPT is investigated. To this end, the implementation of 3D printing technology to effectively deal with a number of predominant issues is examined.

The specific objectives of the thesis are:
- O-ring linac systems may allow for increased time-efficiency of image-guided VMAT. The first objective is to compare an early-adopted, fast-rotating O-ring linac with a conventional C-arm linac in terms of plan quality and treatment delivery time for VMAT of LAHNC (chapter II).
- Spot size preservation using patient-specific bolus RS may substantially improve the dose conformity for IMPT of LAHNC and may reduce the number of hardware manipulations with collision risk compared with conventional RS solutions. The second objective is to quantify the potential benefit of individualized bolus RS in terms of OAR sparing and normal tissue complication probability (NTCP) reduction (chapter III).
- 3D printing technology may provide the flexible object shaping needed for individualized bolus RS and for other functionalities such as patient immobilization. The third objective is twofold: to characterize the mechanical,

geometrical and radiological properties of different 3D printing materials and technologies in detail for the aforementioned purposes and to perform a potential work-up for the clinical use of 3D printed RS (chapter IV).

- 3D printing technology may allow for immobilization with integrated bolus RS and may improve patient immobilization. The <u>fourth objective</u> is to prove the feasibility of the proposed approach in terms of patient comfort and in terms of workflow (chapter V).

References

[1]   Hanahan D, Weinberg RA. Hallmarks of cancer: the next generation. Cell 2011;144:646–74.

[2]   Bray F, Ferlay J, Soerjomataram I, Siegel RL, Torre LA, Jemal A. Global cancer statistics 2018: GLOBOCAN estimates of incidence and mortality worldwide for 36 cancers in 185 countries. CA Cancer J Clin 2018;68:394–424.

[3]   World health statistics 2018: monitoring health for the SDGs, sustainable development goals. Geneva: World Health Organization: 2018.

[4]   Ferlay J, Colombet M, Soerjomataram I, Mathers C, Parkin DM, Piñeros M, et al. Estimating the global cancer incidence and mortality in 2018: GLOBOCAN sources and methods. Int J Cancer 2019;144:1941–53.

[5]   Chow LQM. Head and Neck Cancer. N Engl J Med 2020;382:60–72.

[6]   van der Veen J, Laenen A, Nuyts S. Modern radiotherapy techniques versus three-dimensional conformal radiotherapy for head and neck cancer. Cochrane Database Syst Rev 2017:CD012904.

[7]   Amin MB, Greene FL, Edge SB, Compton CC, Gershenwald JE, Brookland RK, et al. The Eighth Edition AJCC Cancer Staging Manual: Continuing to build a bridge from a population-based to a more "personalized" approach to cancer staging. CA Cancer J Clin 2017;67:93–9.

[8]   Grégoire V, Lefebvre JL, Licitra L, Felip E. Squamous cell carcinoma of the head and neck: EHNS-ESMO-ESTRO clinical practice guidelines for diagnosis, treatment and follow-up. Ann Oncol 2010;21:v184–6.

[9]   Caudell JJ, Torres-Roca JF, Gillies RJ, Enderling H, Kim S, Rishi A, et al. The future of personalised radiotherapy for head and neck cancer. Lancet Oncol 2017;18:e266–73.

[10]   Abdurehim Y, Hua Z, Yasin Y, Xukurhan A, Imam I, Yuqin F. Transoral laser surgery versus radiotherapy: Systematic review and meta-analysis for treatment options of T1a glottic cancer. Head Neck 2012;34:23–33.

[11]   Nutting C. Radiotherapy in head and neck cancer management: United Kingdom National Multidisciplinary Guidelines. J Laryngol Otol 2016;130:S66–7.

[12]   Berwouts D, Swimberghe M, Duprez F, Boterberg T, Bonte K, Deron P, et al. Intensity-modulated radiotherapy for early-stage glottic cancer. Head Neck 2016;38:E179–84.

[13]   Agrawal N, Ha PK. Management of Early-Stage Laryngeal Cancer. Otolaryngol Clin North Am 2008;41:757–69.

[14]   Dirix P, Nuyts S. Evidence-based organ-sparing radiotherapy in head and neck cancer. Lancet Oncol 2010;11:85–91.

[15]   Lacas B, Bourhis J, Overgaard J, Zhang Q, Grégoire V, Nankivell M, et al. Role of radiotherapy fractionation in head and neck cancers (MARCH): an updated meta-

analysis. Lancet Oncol 2017;18:1221–37.

[16]   Mehanna H, Robinson M, Hartley A, Kong A, Foran B, Fulton-Lieuw T, et al. Radiotherapy plus cisplatin or cetuximab in low-risk human papillomavirus-positive oropharyngeal cancer (De-ESCALaTE HPV): an open-label randomised controlled phase 3 trial. Lancet 2019;393:51–60.

[17]   Bonner JA, Harari PM, Giralt J, Cohen RB, Jones CU, Sur RK, et al. Radiotherapy plus cetuximab for locoregionally advanced head and neck cancer: 5-year survival data from a phase 3 randomised trial, and relation between cetuximab-induced rash and survival. Lancet Oncol 2010;11:21–8.

[18]   Nuyts S, Dirix P, Clement PMJ, Poorten V Vander, Delaere P, Schoenaers J, et al. Impact of Adding Concomitant Chemotherapy to Hyperfractionated Accelerated Radiotherapy for Advanced Head-and-Neck Squamous Cell Carcinoma. Int J Radiat Oncol Biol Phys 2009;73:1088–95.

[19]   Blanchard P, Baujat B, Holostenco V, Bourredjem A, Baey C, Bourhis J, et al. Meta-analysis of chemotherapy in head and neck cancer (MACH-NC): A comprehensive analysis by tumour site. Radiother Oncol 2011;100:33–40.

[20]   Grégoire V, Langendijk JA, Nuyts S. Advances in radiotherapy for head and neck cancer. J Clin Oncol 2015;33:3277–84.

[21]   Barton MB, Jacob S, Shafiq J, Wong K, Thompson SR, Hanna TP, et al. Estimating the demand for radiotherapy from the evidence: A review of changes from 2003 to 2012. Radiother Oncol 2014;112:140–4.

[22]   McMahon SJ. The linear quadratic model: Usage, interpretation and challenges. Phys Med Biol 2019;64:01TR01.

[23]   van Leeuwen CM, Oei AL, Crezee J, Bel A, Franken NAP, Stalpers LJA, et al. The alfa and beta of tumours: A review of parameters of the linear-quadratic model, derived from clinical radiotherapy studies. Radiat Oncol 2018;13:96.

[24]   Stuschke M, Thames HD. Fractionation sensitivities and dose-control relations of head and neck carcinomas: Analysis of the randomized hyperfractionation trials. Radiother Oncol 1999;51:113–21.

[25]   Joiner M, van der Kogel A. Basic Clinical Radiobiology. 4th ed. London, UK: Hodder Arnold; 2009.

[26]   Bentzen SM, Johansen L V., Overgaard J, Thames HD. Clinical radiobiology of squamous cell carcinoma of the oropharynx. Int J Radiat Oncol Biol Phys 1991;20:1197–206.

[27]   Okunieff P, Morgan D, Niemierko A, Suit HD. Radiation dose-response of human tumors. Int J Radiat Oncol Biol Phys 1995;32:1227–37.

[28]   Marks LB, Yorke ED, Jackson A, Ten Haken RK, Constine LS, Eisbruch A, et al. Use of

normal tissue complication probability models in the clinic. Int J Radiat Oncol Biol Phys 2010;76:S10-9.

[29] Brodin NP, Kabarriti R, Garg MK, Guha C, Tomé WA. Systematic Review of Normal Tissue Complication Models Relevant to Standard Fractionation Radiation Therapy of the Head and Neck Region Published After the QUANTEC Reports. Int J Radiat Oncol Biol Phys 2018;100:391–407.

[30] Mavroidis P, Price A, Fried D, Kostich M, Amdur R, Mendenhall W, et al. Dose-volume toxicity modeling for de-intensified chemo-radiation therapy for HPV-positive oropharynx cancer. Radiother Oncol 2017;124:240–7.

[31] Merlotti A, Alterio D, Vigna-Taglianti R, Muraglia A, Lastrucci L, Manzo R, et al. Technical guidelines for head and neck cancer IMRT on behalf of the Italian association of radiation oncology - head and neck working group. Radiat Oncol 2014;9:264.

[32] Tol JP, Dahele M, Gregoire V, Overgaard J, Slotman BJ, Verbakel WFAR. Analysis of EORTC-1219-DAHANCA-29 trial plans demonstrates the potential of knowledge-based planning to provide patient-specific treatment plan quality assurance. Radiother Oncol 2019;130:75–81.

[33] Gurney-Champion OJ, McQuaid D, Dunlop A, Wong KH, Welsh LC, Riddell AM, et al. MRI-based Assessment of 3D Intrafractional Motion of Head and Neck Cancer for Radiation Therapy. Int J Radiat Oncol Biol Phys 2018;100:306–16.

[34] van Kranen S, van Beek S, Rasch C, van Herk M, Sonke JJ. Setup Uncertainties of Anatomical Sub-Regions in Head-and-Neck Cancer Patients After Offline CBCT Guidance. Int J Radiat Oncol Biol Phys 2009;73:1566–73.

[35] Velec M, Waldron JN, O'Sullivan B, Bayley A, Cummings B, Kim JJ, et al. Cone-Beam CT Assessment of Interfraction and Intrafraction Setup Error of Two Head-and-Neck Cancer Thermoplastic Masks. Int J Radiat Oncol Biol Phys 2010;76:949–55.

[36] Ahn PH, Ahn AI, Lee CJ, Shen J, Miller E, Lukaj A, et al. Random Positional Variation Among the Skull, Mandible, and Cervical Spine With Treatment Progression During Head-and-Neck Radiotherapy. Int J Radiat Oncol Biol Phys 2009;73:626–33.

[37] Houweling AC, van der Meer S, van der Wal E, Terhaard CHJ, Raaijmakers CPJ. Improved immobilization using an individual head support in head and neck cancer patients. Radiother Oncol 2010;96:100–3.

[38] Lin H, Ding X, Kirk M, Liu H, Zhai H, Hill-Kayser CE, et al. Supine craniospinal irradiation using a proton pencil beam scanning technique without match line changes for field junctions. Int J Radiat Oncol Biol Phys 2014;90:71–8.

[39] Christiansen RL, Hansen CR, Nielsen TB, Johansen J, Brink C. Comparison of three immobilisation systems for radiation therapy in Head and Neck Cancer. Radiother Oncol 2014;103:S106.

[40] Grégoire V, Evans M, Le QT, Bourhis J, Budach V, Chen A, et al. Delineation of the primary tumour Clinical Target Volumes (CTV-P) in laryngeal, hypopharyngeal, oropharyngeal and oral cavity squamous cell carcinoma: AIRO, CACA, DAHANCA, EORTC, GEORCC, GORTEC, HKNPCSG, HNCIG, IAG-KHT, LPRHHT, NCIC CTG, NCRI, NRG Oncolog. Radiother Oncol 2018;126:3–24.

[41] Biau J, Lapeyre M, Troussier I, Budach W, Giralt J, Grau C, et al. Selection of lymph node target volumes for definitive head and neck radiation therapy: a 2019 Update. Radiother Oncol 2019;134:1–9.

[42] Evans M, Beasley M. Target delineation for postoperative treatment of head and neck cancer. Oral Oncol 2018;86:288–95.

[43] Grégoire V, Grau C, Lapeyre M, Maingon P. Target volume selection and delineation (T and N) for primary radiation treatment of oral cavity, oropharyngeal, hypopharyngeal and laryngeal squamous cell carcinoma. Oral Oncol 2018;87:131–7.

[44] Brouwer CL, Steenbakkers RJHM, Bourhis J, Budach W, Grau C, Grégoire V, et al. CT-based delineation of organs at risk in the head and neck region: DAHANCA, EORTC, GORTEC, HKNPCSG, NCIC CTG, NCRI, NRG Oncology and TROG consensus guidelines. Radiother Oncol 2015;117:83–90.

[45] Bedford JL, Thomas MDR, Smyth G. Beam modeling and VMAT performance with the Agility 160-leaf multileaf collimator. J Appl Clin Med Phys 2013;14:172–85.

[46] Saini J, Maes D, Egan A, Bowen SR, St James S, Janson M, et al. Dosimetric evaluation of a commercial proton spot scanning Monte-Carlo dose algorithm: Comparisons against measurements and simulations. Phys Med Biol 2017;62:7659–81.

[47] Thiagarajan A, Caria N, Schöder H, Iyer NG, Wolden S, Wong RJ, et al. Target volume delineation in oropharyngeal cancer: Impact of PET, MRI, and physical examination. Int J Radiat Oncol Biol Phys 2012;83:220–7.

[48] van der Veen J, Gulyban A, Nuyts S. Interobserver variability in delineation of target volumes in head and neck cancer. Radiother Oncol 2019;137:9–15.

[49] ICRU report 83. Prescribing, recording, and reporting photon-beam intensity-modulated radiation therapy (IMRT). vol. 10. Oxford, UK: Oxford University Press; 2010.

[50] Fredriksson A, Forsgren A, Hårdemark B. Minimax optimization for handling range and setup uncertainties in proton therapy. Med Phys 2011;38:1672–84.

[51] Wagenaar D, Kierkels RGJ, Free J, Langendijk JA, Both S, Korevaar EW. Composite minimax robust optimization of VMAT improves target coverage and reduces non-target dose in head and neck cancer patients. Radiother Oncol 2019;136:71–7.

[52] van de Water S, van Dam I, Schaart DR, Al-Mamgani A, Heijmen BJM, Hoogeman MS. The price of robustness; impact of worst-case optimization on organ-at-risk dose and

complication probability in intensity-modulated proton therapy for oropharyngeal cancer patients. Radiother Oncol 2016;120:56–62.

[53] Edward C. Halperin, David E. Wazer, Carlos A. Perez, Luther W. Brady, editors. Perez and Brady's principles and practice of radiation oncology. 6th ed. Philadelphia, PA, USA: Lippincott Williams & Wilkins - Wolters Kluwers; 2013.

[54] Hogstrom KR, Almond PR. Review of electron beam therapy physics. Phys Med Biol 2006;51:R455–89.

[55] Michiels S, Mangelschots B, De Roover R, Depuydt T. Production of patient-specific electron beam aperture cut-outs using a low-cost, multi-purpose 3D printer. J Appl Clin Med Phys 2018;19:756–60.

[56] Nutting CM, Morden JP, Harrington KJ, Urbano TG, Bhide SA, Clark C, et al. Parotid-sparing intensity modulated versus conventional radiotherapy in head and neck cancer (PARSPORT): A phase 3 multicentre randomised controlled trial. Lancet Oncol 2011;12:127–36.

[57] Van Der Laan HP, Christianen MEMC, Bijl HP, Schilstra C, Langendijk JA. The potential benefit of swallowing sparing intensity modulated radiotherapy to reduce swallowing dysfunction: An in silico planning comparative study. Radiother Oncol 2012;103:76–81.

[58] Bortfeld T. IMRT: a review and preview. Phys Med Biol 2006;51:R363–79.

[59] Verbakel WFAR, Cuijpers JP, Hoffmans D, Bieker M, Slotman BJ, Senan S. Volumetric Intensity-Modulated Arc Therapy Vs. Conventional IMRT in Head-and-Neck Cancer: A Comparative Planning and Dosimetric Study. Int J Radiat Oncol Biol Phys 2009;74:252–9.

[60] Otto K. Volumetric modulated arc therapy: IMRT in a single gantry arc. Med Phys 2008;35:310–7.

[61] Van De Water TA, Bijl HP, Schilstra C, Pijls-Johannesma M, Langendijk JA. The Potential Benefit of Radiotherapy with Protons in Head and Neck Cancer with Respect to Normal Tissue Sparing: A Systematic Review of Literature. Oncologist 2011;16:366–77.

[62] Van Der Laan HP, Paul Van Der Laan H, De Water TA Van, Van Herpt HE, Christianen MEMC, Bijl HP, et al. The potential of intensity-modulated proton radiotherapy to reduce swallowing dysfunction in the treatment of head and neck cancer: A planning comparative study. Acta Oncol 2013;52:561–9.

[63] Van De Water S. Optimizing Planning and Delivery of High-Precision Robotic Radiotherapy and Intensity- Modulated Proton Therapy. Erasmus University Rotterdam, 2015.

[64] Schneider U, Pedroni E, Lomax a. The calibration of CT Hounsfield units for radiotherapy treatment planning. Phys Med Biol 1996;41:111–24.

[65] Kraan AC, Van De Water S, Teguh DN, Al-Mamgani A, Madden T, Kooy HM, et al. Dose uncertainties in IMPT for oropharyngeal cancer in the presence of anatomical, range, and setup errors. Int J Radiat Oncol Biol Phys 2013;87:888–96.

[66] Lomax AJ. Intensity modulated proton therapy and its sensitivity to treatment uncertainties 1: the potential effects of calculational uncertainties. Phys Med Biol 2008;53:1027–42.

[67] Lomax AJ. Intensity modulated proton therapy and its sensitivity to treatment uncertainties 2: the potential effects of inter-fraction and inter-field motions. Phys Med Biol 2008;53:1043–56.

[68] Mohan R, Das IJ, Ling C. Empowering Intensity Modulated Proton Therapy Through Physics and Technology: An Overview. Int J Radiat Oncol Biol Phys 2017;99:304–16.

[69] Both S, Shen J, Kirk M, Lin L, Tang S, Alonso-Basanta M, et al. Development and clinical implementation of a universal bolus to maintain spot size during delivery of base of skull pencil beam scanning proton therapy. Int J Radiat Oncol Biol Phys 2014;90:79–84.

[70] Flanz J, Bortfeld T. Evolution of technology to optimize the delivery of proton therapy: The third generation. Semin Radiat Oncol 2013;23:142–8.

[71] Van De Water TA, Lomax AJ, Bijl HP, Schilstra C, Hug EB, Langendijk JA. Using a reduced spot size for intensity-modulated proton therapy potentially improves salivary gland-sparing in oropharyngeal cancer. Int J Radiat Oncol Biol Phys 2012;82:95–114.

[72] Engelsman M, Schwarz M, Dong L. Physics Controversies in Proton Therapy. Semin Radiat Oncol 2013;23:88–96.

[73] Sher DJ, Tishler RB, Pham NL, Punglia RS. Cost-Effectiveness Analysis of Intensity Modulated Radiation Therapy Versus Proton Therapy for Oropharyngeal Squamous Cell Carcinoma. Int J Radiat Oncol Biol Phys 2018;101:875–82.

[74] Frank SJ, Cox JD, Gillin M, Mohan R, Garden AS, Rosenthal DI, et al. Multifield optimization intensity modulated proton therapy for head and neck tumors: A translation to practice. Int J Radiat Oncol Biol Phys 2014;89:846–53.

[75] Frank SJ, Blanchard P, Lee JJ, Sturgis EM, Kies MS, Machtay M, et al. Comparing Intensity-Modulated Proton Therapy With Intensity-Modulated Photon Therapy for Oropharyngeal Cancer: The Journey From Clinical Trial Concept to Activation. Semin Radiat Oncol 2018;28:108–13.

[76] Langendijk JA, Boersma LJ, Rasch CRN, van Vulpen M, Reitsma JB, van der Schaaf A, et al. Clinical Trial Strategies to Compare Protons With Photons. Semin Radiat Oncol 2018;28:79–87.

[77] Widder J, van der Schaaf A, Lambin P, Marijnen CAM, Pignol JP, Rasch CR, et al. The Quest for Evidence for Proton Therapy: Model-Based Approach and Precision Medicine. Int J Radiat Oncol Biol Phys 2016;95:30–6.

[78]   Holt A, Van Gestel D, Arends MP, Korevaar EW, Schuring D, Kunze-Busch MC, et al. Multi-institutional comparison of volumetric modulated arc therapy vs. intensity-modulated radiation therapy for head-and-neck cancer: a planning study. Radiat Oncol 2013;8−26.

[79]   Lu S, Cheng JC, Kuo S, Lee JJ, Chen L, Wu J, et al. Volumetric modulated arc therapy for nasopharyngeal carcinoma : A dosimetric comparison with TomoTherapy and step-and-shoot IMRT. Radiother Oncol 2012;104:324−30.

[80]   Liu W, Patel SH, Harrington DP, Hu Y, Ding X, Shen J, et al. Exploratory study of the association of volumetric modulated arc therapy (VMAT) plan robustness with local failure in head and neck cancer. J Appl Clin Med Phys 2017:1−8.

[81]   Langendijk JA, Lambin P, De Ruysscher D, Widder J, Bos M, Verheij M. Selection of patients for radiotherapy with protons aiming at reduction of side effects: The model-based approach. Radiother Oncol 2013;107:267−73.

[82]   Ning MS, Gomez DR, Shah AK, Kim CR, Palmer MB, Thaker NG, et al. The Insurance Approval Process for Proton Radiation Therapy: A Significant Barrier to Patient Care. Int J Radiat Oncol Biol Phys 2019;104:714−23.

[83]   Miften M, Olch A, Mihailidis D, Moran J, Pawlicki T, Molineu A, et al. Tolerance limits and methodologies for IMRT measurement-based verification QA: Recommendations of AAPM Task Group No. 218. Med Phys 2018;45:e53−83.

[84]   Zou W, Dong L, Kevin Teo BK. Current State of Image Guidance in Radiation Oncology: Implications for PTV Margin Expansion and Adaptive Therapy. Semin Radiat Oncol 2018;28:238−47.

[85]   Van Herk M. Errors and Margins in Radiotherapy. Semin Radiat Oncol 2004;14:52−64.

[86]   Giske K, Stoiber EM, Schwarz M, Stoll A, Muenter MW, Timke C, et al. Local setup errors in image-guided radiotherapy for head and neck cancer patients immobilized with a custom-made device. Int J Radiat Oncol Biol Phys 2011;80:582−9.

[87]   van Beek S, van Kranen S, Mencarelli A, Remeijer P, Rasch C, van Herk M, et al. First clinical experience with a multiple region of interest registration and correction method in radiotherapy of head-and-neck cancer patients. Radiother Oncol 2010;94:213−7.

[88]   Hamming-Vrieze O, Depauw N, Craft DL, Chan AW, Rasch CRN, Verheij M, et al. Impact of setup and range uncertainties on TCP and NTCP following VMAT or IMPT of oropharyngeal cancer patients. Phys Med Biol 2019;64:095001.

[89]   Navran A, Heemsbergen W, Janssen T, Hamming-Vrieze O, Jonker M, Zuur C, et al. The impact of margin reduction on outcome and toxicity in head and neck cancer patients treated with image-guided volumetric modulated arc therapy (VMAT). Radiother Oncol 2019;130:25−31.

[90]   Chen AM, Farwell DG, Luu Q, Donald PJ, Perks J, Purdy JA. Evaluation of the planning

target volume in the treatment of head and neck cancer with intensity-modulated radiotherapy: What is the appropriate expansion margin in the setting of daily image guidance? Int J Radiat Oncol Biol Phys 2011;81:943–9.

[91] Cubillos-mesías M, Troost EGC, Lohaus F, Agolli L. Including anatomical variations in robust optimization for head and neck proton therapy can reduce the need of adaptation. Radiother Oncol 2019;131:127–34.

[92] Kierkels RGJ, Fredriksson A, Both S, Langendijk JA, Scandurra D, Korevaar EW. Automated Robust Proton Planning Using Dose-Volume Histogram-Based Mimicking of the Photon Reference Dose and Reducing Organ at Risk Dose Optimization. Int J Radiat Oncol Biol Phys 2019;103:251–8.

[93] Samuels SE, Eisbruch A, Vineberg K, Lee J, Lee C, Matuszak MM, et al. Methods for Reducing Normal Tissue Complication Probabilities in Oropharyngeal Cancer: Dose Reduction or Planning Target Volume Elimination. Int J Radiat Oncol Biol Phys 2016;96:645–52.

[94] van Kranen S, van Beek S, Mencarelli A, Rasch C, van Herk M, Sonke JJ. Correction strategies to manage deformations in head-and-neck radiotherapy. Radiother Oncol 2010;94:199–205.

[95] Barker JL, Garden AS, Ang KK, O'Daniel JC, Wang H, Court LE, et al. Quantification of volumetric and geometric changes occurring during fractionated radiotherapy for head-and-neck cancer using an integrated CT/linear accelerator system. Int J Radiat Oncol Biol Phys 2004;59:960–70.

[96] Gros SAA, Xu W, Roeske JC, Choi M, Emami B, Surucu M. A novel surrogate to identify anatomical changes during radiotherapy of head and neck cancer patients. Med Phys 2017;44:924–34.

[97] Sonke JJ, Aznar M, Rasch C. Adaptive Radiotherapy for Anatomical Changes. Semin Radiat Oncol 2019;29:245–57.

[98] Brouwer CL, Steenbakkers RJHM, Langendijk JA, Sijtsema NM. Identifying patients who may benefit from adaptive radiotherapy: Does the literature on anatomic and dosimetric changes in head and neck organs at risk during radiotherapy provide information to help? Radiother Oncol 2015;115:285–94.

[99] Hong TS, Tomé WA, Chappell RJ, Chinnaiyan P, Mehta MP, Harari PM. The impact of daily setup variations on head-and-neck intensity-modulated radiation therapy. Int J Radiat Oncol Biol Phys 2005;61:779–88.

[100] Brouwer CL, Steenbakkers RJHM, van der Schaaf A, Sopacua CTC, van Dijk L V., Kierkels RGJ, et al. Selection of head and neck cancer patients for adaptive radiotherapy to decrease xerostomia. Radiother Oncol 2016;120:36–40.

[101] van Kranen S, Hamming-Vrieze O, Wolf A, Damen E, van Herk M, Sonke JJ. Head and

Neck Margin Reduction With Adaptive Radiation Therapy: Robustness of Treatment Plans Against Anatomy Changes. Int J Radiat Oncol Biol Phys 2016;96:653–60.

[102] Góra J, Kuess P, Stock M, Andrzejewski P, Knäusl B, Paskeviciute B, et al. ART for head and neck patients: On the difference between VMAT and IMPT. Acta Oncol 2015:1–9.

[103] Schwartz DL, Garden AS, Thomas J, Chen Y, Zhang Y, Lewin J, et al. Adaptive Radiotherapy for Head-and-Neck Cancer: Initial Clinical Outcomes from a Prospective Trial. Int J Radiat Oncol Biol Phys 2012;83:986–93.

[104] Van Kranen S, Mencarelli A, Van Beek S, Rasch C, Van Herk M, Sonke JJ. Adaptive radiotherapy with an average anatomy model: Evaluation and quantification of residual deformations in head and neck cancer patients. Radiother Oncol 2013;109:463–8.

[105] Wu Q, Chi Y, Chen PY, Krauss DJ, Yan D, Martinez A. Adaptive Replanning Strategies Accounting for Shrinkage in Head and Neck IMRT. Int J Radiat Oncol Biol Phys 2009;75:924–32.

[106] Chen AM, Daly ME, Cui J, Mathai M, Benedict S, Purdy JA. Clinical outcomes among patients with head and neck cancer treated by intensity-modulated radiotherapy with and without adaptive replanning. Head Neck 2014;36:1541–6.

[107] Schwartz DL, Garden AS, Shah SJ, Chronowski G, Sejpal S, Rosenthal DI, et al. Adaptive radiotherapy for head and neck cancer—Dosimetric results from a prospective clinical trial. Radiother Oncol 2013;106:80–4.

[108] Zhao L, Wan Q, Zhou Y, Deng X, Xie C, Wu S. The role of replanning in fractionated intensity modulated radiotherapy for nasopharyngeal carcinoma. Radiother Oncol 2011;98:23–7.

[109] Olteanu LAM, Berwouts D, Madani I, De Gersem W, Vercauteren T, Duprez F, et al. Comparative dosimetry of three-phase adaptive and non-adaptive dose-painting IMRT for head-and-neck cancer. Radiother Oncol 2014;111:348–53.

[110] Brown E, Owen R, Harden F, Mengersen K, Oestreich K, Houghton W, et al. Predicting the need for adaptive radiotherapy in head and neck cancer. Radiother Oncol 2015;116:57–63.

[111] Castelli J, Simon A, Lafond C, Perichon N, Rigaud B, Chajon E, et al. Adaptive radiotherapy for head and neck cancer. Acta Oncol (Madr) 2018;57:1284–92.

[112] Langendijk JA, Doornaert P, Verdonck-de Leeuw IM, Leemans CR, Aaronson NK, Slotman BJ. Impact of late treatment-related toxicity on quality of life among patients with head and neck cancer treated with radiotherapy. J Clin Oncol 2008;26:3770–6.

[113] Leeman JE, Romesser PB, Zhou Y, McBride S, Riaz N, Sherman E, et al. Proton therapy for head and neck cancer: expanding the therapeutic window. Lancet Oncol 2017;18:e254–65.

[114] Hall E. Radiation Biology. Cancer 1985;55:201–57.

[115] Rosenblatt E, Zubizarreta E. Radiotherapy in cancer care: facing the global challenge. Vienna: International Atomic Energy Agency: 2017.

[116] Keall PJ, Nguyen DT, O'Brien R, Zhang P, Happersett L, Bertholet J, et al. Review of Real-Time 3-Dimensional Image Guided Radiation Therapy on Standard-Equipped Cancer Radiation Therapy Systems: Are We at the Tipping Point for the Era of Real-Time Radiation Therapy? Int J Radiat Oncol Biol Phys 2018;102:922–31.

[117] Kamino Y, Takayama K, Kokubo M, Narita Y, Hirai E, Kawawda N, et al. Development of a four-dimensional image-guided radiotherapy system with a gimbaled X-ray head. Int J Radiat Oncol Biol Phys 2006;66:271–8.

[118] Raaymakers BW, Lagendijk JJW, Overweg J, Kok JGM, Raaijmakers AJE, Kerkhof EM, et al. Integrating a 1.5 T MRI scanner with a 6 MV accelerator: Proof of concept. Phys Med Biol 2009;54:N229.

[119] Grau C, Defourny N, Malicki J, Dunscombe P, Borras JM, Coffey M, et al. Radiotherapy equipment and departments in the European countries : Final results from the ESTRO-HERO survey 2014;112:155–64.

[120] Borras JM, Lievens Y, Dunscombe P, Coffey M, Malicki J, Corral J, et al. The optimal utilization proportion of external beam radiotherapy in European countries : An ESTRO-HERO analysis. Radiother Oncol 2015;116:38–44.

[121] Borras JM, Grau C, Corral J, Wong K, Barton MB, Ferlay J, et al. Estimating the number of fractions by tumour site for European countries in 2012 and 2025: An ESTRO-HERO analysis. Radiother Oncol 2017;126:198–204.

[122] Wilson RR. Radiological Use of Fast Protons. Radiology 1946;47:487–91.

[123] Lomax AJ, Böhringer T, Bolsi A, Coray D, Emert F, Goitein G, et al. Treatment planning and verification of proton therapy using spot scanning: Initial experiences. Med Phys 2004;31:3150–7.

[124] Durante M, Paganetti H. Nuclear physics in particle therapy: a review. Rep Prog Phys 2016;79:096702.

[125] Newhauser WD, Zhang R. The physics of proton therapy. Phys Med Biol 2015;60:R155–209.

[126] Jelen U, Bubula ME, Ammazzalorso F, Engenhart-Cabillic R, Weber U, Wittig A. Dosimetric impact of reduced nozzle-to-isocenter distance in intensity-modulated proton therapy of intracranial tumors in combined proton-carbon fixed-nozzle treatment facilities. Radiat Oncol 2013;8:218.

[127] Farace P, Bizzocchi N, Righetto R, Fellin F, Fracchiolla F, Lorentini S, et al. Supine craniospinal irradiation in pediatric patients by proton pencil beam scanning. Radiother Oncol 2017;123:112–8.

[128] Titt U, Mirkovic D, Sawakuchi GO, Perles LA, Newhauser WD, Taddei PJ, et al.

Adjustment of the lateral and longitudinal size of scanned proton beam spots using a pre-absorber to optimize penumbrae and delivery efficiency. Phys Med Biol 2010;55:7097–106.

[129] Safai S, Bortfeld T, Engelsman M. Comparison between the lateral penumbra of a collimated double-scattered beam and uncollimated scanning beam in proton radiotherapy. Phys Med Biol 2008;53:1729–50.

[130] Łukowiak M, Jezierska K, Boehlke M, Wiecko M, Łukowiak A, Podraza W, et al. Utilization of a 3D printer to fabricate boluses used for electron therapy of skin lesions of the eye canthi. J Appl Clin Med Phys 2017;18:76–81.

[131] Tsai JS, Engler MJ, Ling MN, Wu JK, Kramer B, Dipetrillo T, et al. A non-invasive immobilization system and related quality assurance for dynamic intensity modulated radiation therapy of intracranial and head and neck disease. Int J Radiat Oncol Biol Phys 1999;43:455–67.

Volumetric modulated arc therapy of head-and-neck cancer on a fast-rotating O-ring linac: Plan quality and delivery time comparison with a C-arm linac

II

Michiels S, Poels K, Crijns W, Delombaerde L, De Roover R, Vanstraelen B, Haustermans K, Nuyts S, Depuydt T.

Abstract

Background & Purpose

Linac improvements in gantry speed, leaf speed and dose rate may increase the time-efficiency of volumetric modulated arc therapy (VMAT) delivery. The plan quality achievable with faster VMAT however remains to be investigated. In this study, a fast-rotating O-ring linac with fast-moving leaves is compared with a C-arm linac in terms of plan quality and delivery time for VMAT of head-and-neck cancer (HNC).

Material & Methods

For 30 patients with HNC, treatment planning was performed using dual-arc (HA2) and triple-arc (HA3) VMAT on a Halcyon fast-rotating O-ring linac and using dual-arc VMAT on a TrueBeam C-arm linac (TB2). Target coverage metrics and complication probabilities were compared. Plan delivery was verified using 3%/3mm gamma-index analysis of helical diode array measurements. Volumetric image acquisition and plan delivery times were compared.

Results

All studied VMAT-techniques fulfilled the target coverage objectives. D2% to the boost volume was higher for HA2 (median 103.7%, 1st-3rd quartile [103.5%; 104.0%]) and HA3 (103.2% [103.0%; 103.7%)]) than for TB2 (102.6% [102.3%; 103.0%)]), resulting in an increased boost target dose heterogeneity for HA2 and HA3. Complication probabilities were comparable between HA2 and TB2, while HA3 showed a xerostomia probability reduction (0.8% [0.2%; 1.8%]) and dysphagia probability reduction (1.0% [0.2%;1.8%]) compared with TB2. Gamma-index agreement scores were never below 93.0% for HA2, HA3 and TB2. Volumetric imaging and plan delivery time was shorter for HA2 (1m24s±1s) and HA3 (1m54s±1s) than for TB2 (2m47s±1s).

Conclusion

For VMAT of HNC, the fast-rotating O-ring linac at least maintains the plan quality of two arcs on a C-arm linac while reducing the image acquisition and plan delivery time.

RADIATION THERAPY OF HEAD-AND-NECK CANCER (HNC) IS OFTEN challenging due to the large, complex-shaped target volumes in close proximity to a large number of organs at risk (OAR). The introduction of intensity-modulated radiotherapy (IMRT) has led to reduced salivary dysfunction probability because of improved parotid gland sparing [1]. Moreover, IMRT has the potential to reduce swallowing dysfunction probability thanks to the improved sparing of swallowing structures [2]. The improved dose conformity of IMRT however generally comes at the expense of plan delivery time [3].

Increased time efficiency compared with 7-9 fields IMRT can be achieved with volumetric modulated arc therapy (VMAT) [4–8]. Single-arc plans have been shown to yield clinically acceptable plans for VMAT of HNC [8,9], while improvement in target coverage homogeneity and OAR sparing can be achieved by increasing the number of arcs [5,7,10,11]. This however requires additional beam-on time, indicating a trade-off between plan quality and delivery time [11].

A reduction in delivery time may positively impact clinical throughput and patient comfort. Such faster delivery could be achieved by utilizing increased dose rates, for instance using flattening filter free (FFF) beams [12]. The use of FFF for HNC VMAT, however, has not yet shown improvement in delivery efficiency, attributed to the current limitations in gantry and multi-leaf collimator (MLC) speed [12–14]. Improvements in speed of these linear accelerator (linac) components may therefore help in exploiting the potential advantage in delivery efficiency of FFF beams.

O-ring gantry designs are allowed to rotate at higher speeds than the one rotation per minute of current C-arm linacs, due to the encapsulation of the moving parts. The plan quality achieved with a faster VMAT delivery however remains to be quantified, since VMAT fluence distributions result from the interplay between gantry rotation, MLC leaf motion and dose rate [15]. Provided that a faster gantry rotation is supported by improved dose rate and leaf speed, the question remains open as well to which extent an effective improvement in delivery efficiency compared with a C-arm linac can be achieved.

A commercially available O-ring linac, Halcyon (Varian Medical Systems, Palo Alto, CA), combines a FFF beam with a higher gantry and MLC speed than current C-arm linacs, which may allow for improved time-efficiency of VMAT delivery. In the current study, this fast-rotating O-ring linac with fast-moving leaves is compared with a C-arm linac in terms of plan quality and delivery time for VMAT of HNC.

II.1 Materials & Methods

II.1.1 Linac systems

The Halcyon IMRT/VMAT delivery system consists of a 6 MV FFF straight-through linac mounted on an O-ring gantry, , which allows for a maximum rotation speed of 4 rpm. The jawless MLC is composed of two staggered layers of 28 leaf pairs, with a projected leaf width of 10 mm. The maximum leaf speed is 5 cm/s and the leaf span is 28 cm. For the delivery of VMAT for HNC, this fast-rotating O-ring linac was compared with a selected C-arm linac (TrueBeam, Varian Medical Systems), which has a maximum rotation speed of 1 rpm. On this C-arm linac, the used Millennium 120 MLC consists of 40 central leaf pairs of 5 mm width and 20 peripheral leaf pairs of 10 mm width, with a maximum leaf speed of 2.5 cm/s. The leaves are mounted on opposing, movable carriages and are subject to a maximum leaf span of 15 cm. On both systems the maximum dose rate was used, namely 6.0 Gy/min (at isocenter, for a 10x10 cm² field at 10 cm depth in water) on the fast-rotating O-ring linac and 4.8 Gy/min on the C-arm linac.

II.1.2 Patients and dose prescription

Computed tomography (CT) data of 30 patients with HNC, evenly distributed over three subsites (larynx, oropharynx and nasopharynx), were used (Table 1). The primary clinical target volume was delineated according to the clinical protocol in use. Neck lymph nodes and OAR were delineated according to published guidelines [16,17]. Planning target volumes (PTV) were created by isotropically expanding the clinical target volumes with 5 mm. For laryngeal and oropharyngeal cases, 70 Gy was prescribed to the high-risk PTV (PTV$_{Boost}$; primary tumor and positive neck) and 54.25 Gy to the low-risk PTV (PTV$_{Elective}$; elective neck), to be delivered in 35 fractions with a simultaneously integrated boost (SIB). For nasopharyngeal cases, prescription doses were 66.96 Gy and 59.4 Gy, to be delivered in 33 fractions with a SIB.

Table 1. Patient characteristics.

		Larynx	**Oropharynx**	**Nasopharynx**
Volume of target [cm³]	PTV_{Boost}	134 (110 − 192)	237 (181 − 427)	253 (172 − 310)
	PTV_{Total}	462 (406 − 477)	573 (505 − 772)	861 (681 − 933)
Number of patients per UICC-stage	**I**	0 (0)	0 (0)	1 (0)
	II	1 (0)	0 (0)	2 (2)
	III	5 (1)	3 (3)	5 (5)
	IVa	4 (4)	6 (5)	2 (2)
	IVb	0 (0)	1 (1)	0 (0)

Abbreviations: UICC = International Union Against Cancer; PTV = Planning Target Volume.
The median PTV-volumes per subsite are shown, together with the 1st and 3rd quartile (between brackets). The number of patients per stage was determined according to the 7th UICC staging-edition. The number of patients with positive lymph nodes is shown between brackets.

II.1.3 Planning objectives

PTV objectives were such that 98% of the PTV_{Boost} and $PTV_{Elective}$ volume received more than 95% of their respective dose prescription. Additional objectives were a near-maximum dose $D_{2\%}$ below 107% [18] of the high-dose prescription for PTV_{Boost} and PTV_{Total} (defined as the union of PTV_{Boost} and $PTV_{Elective}$). The objective for $PTV_{Elective\ only}$ (defined as $PTV_{Elective}$ minus PTV_{Boost} isotropically expanded with 5 mm) was a $D_{2\%}$ below 107% of the low-dose prescription. Planning risk volumes (PRV) were defined for the spinal cord (5 mm margin) and brainstem (3 mm margin). Hard constraints were used for their $D_{2\%}$ to remain strictly below 45 Gy and 50 Gy, respectively. For the OAR, priority was given to minimize the mean dose (D_{Mean}) to the contralateral (and if possible also to the ipsilateral) parotid gland to reduce risk of salivary dysfunction [19]. The next priority was to minimize D_{Mean} to the pharyngeal constrictor muscles (PCM) and supraglottic larynx, to reduce risk of swallowing dysfunction [20,21]. Finally, D_{Mean} to the oral cavity, glottic area and submandibular glands was minimized.

II.1.4 Planning techniques

Dual-arc VMAT on a C-arm linac (TB2)

A commonly used planning technique for VMAT of HNC on a C-arm linac [6,11,13,22,23], namely two arcs using a 6 MV flattened photon beam (TB2), was selected as a reference for comparison. For these TB2 plans on the C-arm linac, collimator angles were set at 10°/80°, with orthogonal leaf orientations for maximal OAR sparing but with a slight inclination with respect to the orientation plane and axis,

respectively, to avoid cumulative tongue and groove effects [24]. For the frequent cases in HNC where the craniocaudal dimension of PTV$_{Total}$ exceeded 15 cm, this setup would violate the 15 cm leaf span limitation for the second arc. Therefore the collimator angles were set at 10°/350° in those cases, using an 8 cm overlap symmetric around the isocenter.

Dual-arc (HA2) and triple-arc (HA3) VMAT on a fast-rotating O-ring linac

The VMAT planning technique studied on the fast-rotating O-ring linac consisted of two arcs (HA2), with collimators set at 10°/80° given the absence of any leaf span limitation. As the MLC system of the fast-rotating O-ring linac consists of broader leaves, an additional arc could be needed to achieve plan quality comparable to the TB2 reference on a C-arm linac. Therefore triple-arc VMAT (HA3) with collimators 10°/45°/80° was studied as well, where the 45° angle was added to give more degrees of freedom to the optimizer for potentially improved OAR sparing.

II.1.5   Plan optimization and dose calculation

Plan optimization was performed in the Eclipse (Varian Medical Systems) treatment planning system (TPS) using the photon optimizer version 15.1. Patient-specific sets of optimization weights for the different objectives were determined for HA2, with user-interaction exclusively in the first step of the first multi-resolution level. Optimization weights were determined such that the cost function was dominated by the PTV objectives, albeit in a balanced competition with the OAR objectives according to the described priorities. HA3- and TB2-plans were generated using the same patient-specific sets of optimization weights, to avoid a weight-difference bias in the optimization. Intermediate and final dose calculation was performed using the anisotropic analytical algorithm (AAA) version 15.1 with a voxel size of 2.5x2.5x2.5 mm³. The dose distributions were normalized to the prescribed D$_{Mean}$ to PTV$_{Boost}$ for all created plans.

Currently the fast-rotating O-ring linac is available with MV-imaging only. Daily imaging is imposed by the TPS and the imaging dose is automatically included in the plan optimization. For this study, a daily low-dose cone beam CT (CBCT) (16 cm craniocaudal field size, symmetric around the isocenter) was included in each plan. For TB2-plans the daily imaging dose from MV-CBCT was included as well by calculating

its dose over all the fractions and using it as a base plan for the optimization. This integral dose bath affects achievable OAR doses and dose gradients but was also taken into account during the plan optimization for TB2 to avoid bias in the plan quality comparison.

II.1.6   Plan quality evaluation

PTV and OAR dose metrics were evaluated for all plans. A homogeneity index (HI) was calculated for PTV$_{Boost}$ and PTV$_{Elective\ only}$ according to ICRU 83 [18]. A conformity index (CI) was calculated for PTV$_{Boost}$ and PTV$_{Total}$ as the ratio of the volume enclosed by the 95% isodose to the volume of the considered PTV [25]. Probability of grade 2-4 patient-rated xerostomia after 6 months [19] and grade 2-4 physician-rated dysphagia after 6 months [20] were calculated. For all metrics, two-sided Wilcoxon matched-pairs signed-rank tests (p<0.05) were performed between HA2 and TB2 and between HA3 and TB2.

II.1.7   Plan delivery verification

Patient-specific quality assurance (QA) was performed for a subset of 10 patients distributed over the different subsites. These patients were selected based on the largest differences in D$_{Mean}$ to the parotid glands and to the swallowing structures between HA3- and TB2-plans. For these patients, all the plans were delivered on an ArcCHECK helical diode array (Sun Nuclear Corporation, Melbourne, FL) [26,27]. The agreement between calculated and measured dose distributions was evaluated with gamma-index ($\Gamma_{3\%,\ 3mm}$) analysis, using 3% (local)/3mm dose difference and distance-to-agreement criteria and a 20% lower dose exclusion threshold [28].

II.1.8   Image acquisition, plan delivery and treatment time

For the subset of patients for which plan delivery was verified, the acquisition time for a full-fan CBCT on the respective machines (MV-CBCT on the fast-rotating O-ring linac, kV-CBCT on the C-arm linac) was recorded. For these patients, the time needed to deliver the HA2-, HA3- and TB2-plans in automation mode was recorded as well.

Clinical timings were recorded for a number of actual treatment fractions delivered on the fast-rotating O-ring linac using HA3. Recordings were acquired for 40 fractions in

total, distributed over seven patients with a diagnosis and dose description similar to the patient characteristics shown in Table 1, with a minimum of 5 recordings per patient. During each fraction, image-guidance was performed using MV-CBCT. The time was recorded from the moment the patient entered the vault to the moment the patient stepped off the treatment couch. On a day on which monthly QA was performed on the fast-rotating O-ring linac, five patients received a TB2 fraction on the C-arm linac using kV-CBCT image-guidance, for which the time was recorded as well. Given the small sample size of these TB2-recordings, these measurements were supported with average treatment slots reported in recent literature [29,30].

II.2 Results

II.2.1 Plan quality

Target coverage metrics, OAR doses and NTCP-values are shown in Table 2 for the whole studied population and in the supplementary table per individual subsite. When considering the former, $D_{2\%}$ to PTV_{Boost} was increased for HA2 (median 103.7%, 1st-3rd quartile [103.5%; 104.0%], p<0.001) and HA3 (103.2% [103.0%; 103.7%], p<0.001) compared with TB2 (102.6% [102.3%; 103.0%]). HI was increased as well for HA2 (8.6% [7.8%; 10.0%], p<0.001) and HA3 (7.6% [6.9%; 8.7%], p<0.03) compared with TB2 (7.3% [6.5%; 8.5%]).

D_{Mean} to the contralateral parotid gland showed no difference between HA2 and TB2 but was reduced for HA3 (23.2 Gy [17.7 Gy; 26.9 Gy], p<0.001) compared with TB2 (25.1 Gy [19.2 Gy; 27.5 Gy]). The associated xerostomia probability was reduced for HA3 (41.2% [35.2%; 45.5%], p<0.001) compared with TB2 (43.4% [36.8%; 46.2%]).

D_{Mean} to the superior PCM showed no difference between HA2 and TB2 but was reduced for HA3 (63.0 Gy [46.5 Gy; 67.9 Gy], p=0.03) compared with TB2 (63.4 Gy [47.3 Gy; 68.2 Gy]). D_{Mean} to the supraglottic larynx showed no difference between HA2 and TB2 but was reduced for HA3 (45.6 Gy [42.0 Gy; 68.3 Gy], p<0.001) compared with TB2 (46.9 Gy [43.3 Gy; 68.4 Gy]). The associated dysphagia probability was increased for HA2 (31.1% [21.9%; 38.6%]) compared with TB2 (30.9% [21.3%; 37.0%], p=0.049), but was reduced for HA3 (29.1% [20.1%; 36.6%], p<0.001) compared with TB2.

II.2.2 Plan delivery verification

The median $\Gamma_{3\%,3mm}$ agreement score was 97.5% (range [96.6%; 98.6%]) for HA2, 96.9% ([95.2%; 97.7%]) for HA3 and 93.5% ([93.0%; 95.2]) for TB2. The agreement scores for the delivered TB2-plans were lower than for the HA2-plans (p=0.02) and HA3-plans (p=0.02), but all agreement scores exceeded a clinical acceptance threshold of 90% as reported in literature [31] and as used at the authors' institute.

II.2.3 Image acquisition, plan delivery and treatment time

The group mean of the treatment time recordings for HA3 (n=40) was 8m50s ± 1m17s. The mean of the treatment time recordings for TB2 (n=5) was 11m12s ± 01m12s. The mean acquisition time for a full-fan CBCT was 14s ± 0s on the fast-rotating O-ring linac and 35s ± 0s on the C-arm linac. The mean plan delivery time was 1m10s ±1s for HA2, 1m40s ±1s for HA3 and 2m12s ± 1s for TB2.

Table 2. Target coverage metrics, OAR mean doses and NTCP-values for the whole studied patient population.

| | | All subsites | | |
		TB2	HA2	HA3
Target coverage metric	PTV$_{Boost}$ — D$_{98\%}$ [%]	95.7 (95.2-96.1)	**95.3** (95.0-95.8)	**95.9** (95.5-96.4)
	PTV$_{Boost}$ — D$_{2\%}$ [%]	102.6 (102.3-103.0)	**103.7** (103.5-104.0)	**103.2** (103.0-103.7)
	PTV$_{Boost}$ — HI [%]	7.3 (6.5-8.5)	**8.6** (7.8-10.0)	**7.6** (6.9-8.7)
	PTV$_{Boost}$ — CI [%]	114.5 (110.4-116.6)	114.8 (111.7-120.9)	114.4 (110.6-117.5)
	PTV$_{Elective\ only}$ — D$_{98\%}$ [%]	95.5 (95.0-96.1)	95.2 (94.8-95.5)	95.8 (95.4-96.2)
	PTV$_{Elective\ only}$ — D$_{2\%}$ [%]	105.6 (104.6-106.0)	**105.9** (105.3-106.5)	**105.0** (104.6-105.7)
	PTV$_{Elective\ only}$ — HI [%]	10.5 (9.7-11.8)	**11.3** (10.1-12.4)	**9.6** (8.6-10.9)
	PTV$_{Total}$ — CI [%]	145.7 (138.7-151.6)	146.5 (141.2-155.0)	144.4 (137.8-153.3)
OAR mean dose	Parotid gland, CL [Gy]	25.1 (19.2-27.5)	24.6 (18.9-27.2)	**23.2** (17.7-26.9)
	Parotid gland, IL [Gy]	36.8 (24.8-45.6)	37.0 (25.2-47.4)	**35.4** (24.8-44.8)
	PCM, Superior [Gy]	63.4 (47.3-68.2)	63.3 (49.2-68.0)	**63.0** (46.5-67.9)
	PCM, Middle [Gy]	53.1 (40.8-65.7)	53.1 (41.5-65.9)	**52.6** (40.1-64.3)
	PCM, Inferior [Gy]	41.6 (31.3-65.1)	42.2 (31.9-62.7)	**38.3** (29.0-63.6)
	Supraglottic larynx [Gy]	46.9 (43.3-68.4)	47.2 (44.5-68.6)	**45.6** (42.0-68.3)
	Glottic area [Gy]	36.5 (30.7-69.3)	37.4 (31.4-69.3)	**35.2** (28.6-69.3)
	Oral cavity [Gy]	43.7 (30.0-50.2)	44.6 (31.9-49.9)	**42.7** (29.0-50.1)
	Subm. gland, CL [Gy]	53.6 (47.6-60.0)	53.6 (46.1-60.2)	**52.4** (45.4-59.1)
	Subm. gland, IL [Gy]	64.6 (58.0-68.4)	63.7 (57.7-68.6)	**64.0** (57.6-68.3)
NTCP	Xerostomia* [%]	43.4 (36.8-46.2)	42.9 (36.5-45.9)	**41.2** (35.2-45.5)
	Dysphagia** [%]	30.9 (21.3-37.0)	**31.1** (21.9-38.6)	**29.1** (20.1-36.6)

Abbreviations: OAR = organ at risk; NTCP = normal tissue complication probability; TB2 = VMAT on a C-arm linac using 2 arcs; HA2 & HA3 = VMAT on a fast-rotating O-ring linac using 2 and 3 arcs, respectively; PTV = Planning Target Volume; D$_{xx\%}$ = dose covering xx% of the target volume; HI = homogeneity index according to ICRU 83 [18]; CI = conformity index calculated as the ratio of the volume enclosed by the 95% isodose to the volume of the considered PTV [25]; CL = contralateral; IL = ipsilateral; PCM = pharyngeal constrictor muscle; Subm. = submandibular.

The median values are shown, together with the 1st and 3rd quartile (between brackets). HA2- and HA3-metrics yielding $p < 0.05$ for a Wilcoxon matched-pairs signed-rank test compared to TB2 are shown in bold.
*   Grade 2-4 patient-rated xerostomia after 6 months [19].
** Grade 2-4 physician-rated dysphagia after 6 months [20]

II.3 Discussion

In this study, a Halcyon fast-rotating O-ring linac with fast-moving leaves was compared with a C-arm linac in terms of plan quality and delivery time for VMAT of HNC. Since the fast-rotating O-ring linac has been used clinically since only recently, this is one of the first quantifications of its performance. For VMAT of HNC, the fast-rotating O-ring linac at least maintains the plan quality of two arcs on the C-arm linac while reducing the image acquisition and plan delivery time. At the authors' institute, HA3 has been implemented as the preferred planning technique for VMAT of HNC on the fast-rotating O-ring linac, due to the minor improvements in target dose homogeneity and OAR sparing compared with HA2. Treatment time recordings using HA3 on the fast-rotating O-ring linac showed a mean of 8m50s ± 1m17s.

Differences in treatment planning processes were avoided as much as possible, to minimize bias in the plan quality comparison. Currently the fast-rotating O-ring linac is only available with MV-imaging. Daily imaging is imposed by the TPS for the fast-rotating O-ring linac and the imaging dose is automatically included in the plan optimization. In this study, a daily low-dose MV-CBCT was included in each plan, including the TB2-plans. This way, observed plan quality differences between the studied VMAT-techniques should not result from differences in image-guidance but from each machine's specific combination of MLC, beam and gantry characteristics. In addition, kV-CBCT will become available on the fast-rotating O-ring linac in the short term, so that simulating the same imaging modality could be considered reasonable for current comparisons.

HA2 and HA3 make use of the only beam available on the fast-rotating O-ring linac, namely 6MV FFF. One could argue that the TB2 reference on a C-arm linac should use the same beam profile and energy. Indeed, differences in these beam characteristics between HA2/HA3 and TB2 can result in differences in OAR sparing capability and target dose homogeneity [12]. In a comparison of 6MV FFF and 6MV flattened for VMAT of HNC on a C-arm linac, the flattened beam was reported to achieve similar OAR sparing but improved target dose homogeneity compared with the FFF beam, although it was not clarified whether this plan quality difference originated from differences in beam profile or in mean energy [13]. In addition, a 6 MV flattened beam has been shown to deliver VMAT for HNC with similar or increased time-efficiency

compared with a 6 MV FFF beam [13,14]. As the current study focussed on plan quality and time-efficiency of VMAT delivery, a 6 MV flattened beam was used for the TB2 reference on a C-arm linac.

The selected TB2 reference for VMAT of HNC on a C-arm linac consists of two arcs. A number of studies however indicated that a single arc already yields clinically acceptable plans with sufficient OAR sparing [8,9,14]. On the other hand, Guckenberger et al. [10] reported that at least two arcs are required for VMAT of HNC to achieve OAR sparing and boost target dose homogeneity comparable to fixed-field IMRT. Tol et al. considered four arcs as an optimal balance between plan quality and delivery efficiency [11]. Overall, the intermediate number of two arcs has been a widely described setup for VMAT of HNC on a C-arm linac [6,11,13,22,23]. The TB2 planning technique used in the current study can therefore be considered a relevant reference on a C-arm linac.

HA2 and HA3 on the fast-rotating O-ring linac showed a lower target dose homogeneity than TB2 on the C-arm linac, although the $D_{2\%}$ and $D_{98\%}$ target coverage objectives were fulfilled for nearly all cases. Complication probabilities were comparable between HA2 and TB2, while HA3 showed a xerostomia probability reduction (median 0.8%, 1st-3rd quartile [0.2%;1.8%]) and dysphagia probability reduction (1.0% [0.2%;1.8%]) compared with TB2. Though these reductions showed statistical significance, differences actually observed in clinical practice may be limited. When comparing HA3 with HA2, the additional arc for HA3 likewise improved the target dose homogeneity and OAR sparing slightly. Other studies reported comparable to larger differences for these plan qualities when increasing the number of arcs on a C-arm linac, namely from one arc to two arcs [5,7] and from two to four arcs [11]. Further increasing the number of arcs on the fast-rotating O-ring linac may further improve plan quality on the fast-rotating O-ring linac as well. Adding more arcs however would likely undo the gain in delivery efficiency observed for HA2 and HA3 compared with TB2 on the C-arm linac.

The maximum gantry rotation speed for the fast-rotating O-ring linac is 4 times as high as for the C-arm linac. Nevertheless, the rotation speed during VMAT plan delivery is only 2 times as high as for the C-arm linac, as the MLC leaf speed for the fast-rotating O-ring linac is only two times as high as for the C-arm linac. The resulting volumetric

image acquisition and plan delivery time was reduced for HA2 (1m24s ± 1s) and HA3 (1m54s ± 1s) on the fast-rotating O-ring linac compared with TB2 (2m47±1s) on the C-arm linac.

Besides volumetric imaging and plan delivery time, however, actual treatment times are influenced by other workflow steps as well. On one hand, matching times may currently be advantageous for the C-arm linac due to the superior soft tissue contrast of kV-CBCT [33]. On the other hand, overall workflow efficiency may be advantageous for the fast-rotating O-ring linac due to an increased number of automated steps. A recent study showed that workflow efficiency on C-arm linacs can be improved as well using a dedicated streamlining approach [30]. Differences due to C-arm linac characteristics however cannot be overcome, such as volumetric image acquisition time, plan delivery time and the need to insert and retract imaging device support arms. A reduction in treatment time on the fast-rotating O-ring linac can therefore be expected.

In the current study, treatment time recordings using HA3 on the fast-rotating O-ring linac showed a mean value of 8m50s ± 1m17s, while TB2-recordings on the C-arm linac showed a mean value of 11m12s ± 01m12s. A limitation of the TB2-recordings was the small sample size, although the mean value was in line with treatment slots of 12 minutes widely reported in literature for current C-arm linacs [9,29,30]. To quantify a potential benefit in clinical throughput on the fast-rotating O-ring linac, a comparison of streamlined treatment slots on both machine types, with a sufficient number of paired samples, would be needed.

In conclusion, a commercially available O-ring linac, which combines a FFF beam with a higher gantry and MLC speed than current C-arm linacs, was evaluated for the delivery of VMAT for HNC. The fast-rotating O-ring linac at least maintains the plan quality of two arcs on a C-arm linac while reducing the image acquisition and plan delivery time. A reduction in treatment time for VMAT of HNC on the fast-rotating linac can be expected owing to its inherent machine characteristics, however this needs to be quantified in further study.

References

[1]   Nutting CM, Morden JP, Harrington KJ, Urbano TG, Bhide SA, Clark C, et al. Parotid-sparing intensity modulated versus conventional radiotherapy in head and neck cancer (PARSPORT): A phase 3 multicentre randomised controlled trial. Lancet Oncol 2011;12:127–36.

[2]   Van Der Laan HP, Christianen MEMC, Bijl HP, Schilstra C, Langendijk JA. The potential benefit of swallowing sparing intensity modulated radiotherapy to reduce swallowing dysfunction: An in silico planning comparative study. Radiother Oncol 2012;103:76–81.

[3]   Palma DA, Verbakel WFAR, Otto K, Senan S. New developments in arc radiation therapy: A review. Cancer Treat Rev 2010;36:393–9.

[4]   Clemente S, Wu B, Sanguineti G, Fusco V, Ricchetti F, Wong J, et al. SmartArc-based volumetric modulated arc therapy for oropharyngeal cancer: A dosimetric comparison with both intensity-modulated radiation therapy and helical tomotherapy. Int J Radiat Oncol Biol Phys 2011;80:1248–55.

[5]   Vanetti E, Clivio A, Nicolini G, Fogliata A, Ghosh-Laskar S, Agarwal JP, et al. Volumetric modulated arc radiotherapy for carcinomas of the oro-pharynx, hypo-pharynx and larynx: A treatment planning comparison with fixed field IMRT. Radiother Oncol 2009;92:111–7.

[6]   Lu SH, Cheng JCH, Kuo SH, Lee JJS, Chen LH, Wu JK, et al. Volumetric modulated arc therapy for nasopharyngeal carcinoma: A dosimetric comparison with TomoTherapy and step-and-shoot IMRT. Radiother Oncol 2012;104:324–30.

[7]   Verbakel WFAR, Cuijpers JP, Hoffmans D, Bieker M, Slotman BJ, Senan S. Volumetric Intensity-Modulated Arc Therapy Vs. Conventional IMRT in Head-and-Neck Cancer: A Comparative Planning and Dosimetric Study. Int J Radiat Oncol Biol Phys 2009;74:252–9.

[8]   Stieler F, Wolff D, Schmid H, Welzel G, Wenz F, Lohr F. A comparison of several modulated radiotherapy techniques for head and neck cancer and dosimetric validation of VMAT. Radiother Oncol 2011;101:388–93.

[9]   Bertelsen A, Hansen CR, Johansen J, Brink C. Single Arc Volumetric Modulated Arc Therapy of head and neck cancer. Radiother Oncol 2010;95:142–8.

[10] Guckenberger M, Richter A, Krieger T, Wilbert J, Baier K, Flentje M. Is a single arc sufficient in volumetric-modulated arc therapy (VMAT) for complex-shaped target volumes? Radiother Oncol 2009;93:259–65.

[11] Tol JP, Dahele M, Slotman BJ, Verbakel WF a R. Increasing the number of arcs improves head and neck volumetric modulated arc therapy plans. Acta Oncol 2015;54:283–7.

[12] Budgell G, Brown K, Cashmore J, Duane S, Frame J, Hardy M, et al. IPEM topical report 1: Guidance on implementing flattening filter free (FFF) radiotherapy. Phys Med Biol 2016;61:8360–94.

[13] Gasic D, Ohlhues L, Brodin NP, Fog LS, Pommer T, Bangsgaard JP, et al. A treatment planning and delivery comparison of volumetric modulated arc therapy with or without flattening filter for gliomas, brain metastases, prostate, head/neck and early stage lung cancer. Acta Oncol 2014;53:1005–11.

[14] Lechner W, Kragl G, Georg D. Evaluation of treatment plan quality of IMRT and VMAT with and without flattening filter using Pareto optimal fronts. Radiother Oncol 2013;109:437–41.

[15] Otto K. Volumetric modulated arc therapy: IMRT in a single gantry arc. Med Phys 2008;35:310–7.

[16] Grégoire V, Ang K, Budach W, Grau C, Hamoir M, Langendijk JA, et al. Delineation of the neck node levels for head and neck tumors : A 2013 update . DAHANCA , EORTC , HKNPCSG , NCIC CTG , NCRI , RTOG , TROG consensus guidelines. Radiother Oncol 2013;110:172–81.

[17] Brouwer CL, Steenbakkers RJHM, Bourhis J, Budach W, Grau C, Grégoire V, et al. CT-based delineation of organs at risk in the head and neck region: DAHANCA, EORTC, GORTEC, HKNPCSG, NCIC CTG, NCRI, NRG Oncology and TROG consensus guidelines. Radiother Oncol 2015;117:83–90.

[18] ICRU report 83. Prescribing, recording, and reporting photon-beam intensity-modulated radiation therapy (IMRT). vol. 10. Oxford, UK: Oxford University Press; 2010.

[19] Beetz I, Schilstra C, Van Der Schaaf A, Van Den Heuvel ER, Doornaert P, Van Luijk P, et al. NTCP models for patient-rated xerostomia and sticky saliva after treatment with intensity modulated radiotherapy for head and neck cancer: The role of dosimetric and clinical factors. Radiother Oncol 2012;105:101–6.

[20] Christianen MEMC, Schilstra C, Beetz I, Muijs CT, Chouvalova O, Burlage FR, et al. Predictive modelling for swallowing dysfunction after primary (chemo)radiation : Results of a prospective observational study. Radiother Oncol 2012;105:107–14.

[21] Mavroidis P, Price A, Fried D, Kostich M, Amdur R, Mendenhall W, et al. Dose-volume toxicity modeling for de-intensified chemo-radiation therapy for HPV-positive

oropharynx cancer. Radiother Oncol 2017;124:240–7.

[22] Doornaert P, Verbakel WFAR, Bieker M, Slotman BJ, Senan S. RapidArc planning and delivery in patients with locally advanced head-and-neck cancer undergoing chemoradiotherapy. Int J Radiat Oncol Biol Phys 2011;79:429–35.

[23] Holt A, Van Gestel D, Arends MP, Korevaar EW, Schuring D, Kunze-Busch MC, et al. Multi-institutional comparison of volumetric modulated arc therapy vs. intensity-modulated radiation therapy for head-and-neck cancer: a planning study. Radiat Oncol 2013:8–26.

[24] Crijns W, Budiharto T, Defraene G, Verstraete J, Depuydt T, Haustermans K, et al. IMRT-based optimization approaches for volumetric modulated single arc radiotherapy planning. Radiother Oncol 2010;95:149–52.

[25] Feuvret L, Noël G, Mazeron JJ, Bey P. Conformity index: A review. Int J Radiat Oncol Biol Phys 2006;64:333–42.

[26] Létourneau D, Publicover J, Kozelka J, Moseley DJ, Jaffray DA. Novel dosimetric phantom for quality assurance of volumetric modulated arc therapy. Med Phys 2009;36:1813–21.

[27] Hussein M, Rowshanfarzad P, Ebert MA, Nisbet A, Clark CH. A comparison of the gamma index analysis in various commercial IMRT/VMAT QA systems. Radiother Oncol 2013;109:370–6.

[28] Depuydt T, Van Esch A, Huyskens DP. A quantitative evaluation of IMRT dose distributions: Refinement and clinical assessment of the gamma evaluation. Radiother Oncol 2002;62:309–19.

[29] Van Dyk J, Zubizarreta E, Lievens Y. Cost evaluation to optimise radiation therapy implementation in different income settings : A time-driven activity-based analysis. Radiother Oncol 2017;125:178–85.

[30] Kapur A, Adair N, O'Brien M, Naparstek N, Cangelosi T, Zuvic P, et al. Improving efficiency and safety in external beam radiation therapy treatment delivery using a Kaizen approach. Pract Radiat Oncol 2017;7:e499–506.

[31] Aristophanous M, Suh Y, Chi PC, Whittlesey LJ, LaNeave S, Martel MK. Initial clinical experience with ArcCHECK for IMRT / VMAT QA. J Appl Clin Med Phys 2016;17:20–33.

[32] Christianen MEMC, Schilstra C, Beetz I, Muijs CT, Chouvalova O, Burlage FR, et al. Predictive modelling for swallowing dysfunction after primary (chemo)radiation: Results of a prospective observational study. Radiother Oncol 2012;105:107–14.

[33] Bissonnette J-P, Balter PA, Dong L, Langen KM, Lovelock DM, Miften M, et al. Quality assurance for image-guided radiation therapy utilizing CT-based technologies: a report of the AAPM TG-179. Med Phys 2012;39:1946–63.

Supplementary table. Target coverage metrics, OAR mean doses and NTCP-values per individual subsite.

			Larynx			Oropharynx			Nasopharynx		
			TB2	HA2	HA3	TB2	HA2	HA3	TB2	HA2	HA3
Target coverage metric	PTV$_{Boost}$	D$_{98\%}$ [%]	95.5 (95.1-96.1)	95.6 (95.3-95.9)	**96.2** (95.9-96.6)	95.5 (94.6-95.8)	95.0 (94.6-95.5)	95.7 (95.3-96.0)	95.7 (95.3-95.8)	**95.1** (94.0-95.9)	95.6 (94.6-95.9)
		D$_{2\%}$ [%]	102.5 (102.3-102.6)	**103.6** (103.5-103.7)	**103.1** (103.0-103.3)	102.8 (102.1-103.2)	**103.6** (103.5-104.1)	**103.2** (103.0-103.6)	102.8 (102.6-103.3)	**104.0** (103.8-104.2)	103.5 (103.2-103.8)
		HI [%]	7.0 (6.5-7.5)	**8.2** (7.8-8.5)	7.0 (6.6-8.0)	7.7 (6.4-8.9)	**8.7** (8.1-9.9)	7.7 (7.1-8.5)	7.2 (6.7-8.0)	**8.9** (7.5-10.2)	**8.0** (7.1-9.0)
		CI [%]	113.8 (110.8-115.2)	114.5 (112.0-117.5)	112.0 (110.9-114.5)	111.7 (110.2-113.4)	112.1 (109.1-115.8)	110.5 (108.1-113.9)	119.2 (116.4-127.9)	**120.9** (118.7-128.0)	119.0 (116.3-126.6)
	PTV$_{Elective\ only}$	D$_{98\%}$ [%]	95.8 (95.6-96.1)	95.4 (95.3-96.0)	96.3 (96.1-96.5)	95.3 (94.9-96.1)	95.2 (95.0-95.4)	95.8 (95.6-96.1)	95.3 (95.0-95.7)	**94.4** (93.9-94.8)	95.1 (94.6-95.6)
		D$_{2\%}$ [%]	105.7 (105.1-106.0)	105.9 (105.5-106.3)	104.9 (104.6-105.1)	105.3 (104.6-106.0)	105.3 (104.9-106.6)	104.8 (104.1-105.9)	105.9 (105.5-106.0)	106.1 (105.7-106.9)	105.3 (105.1-105.9)
		HI [%]	9.6 (8.7-10.3)	**10.1** (9.6-10.6)	**8.4** (8.1-8.9)	11.8 (10.3-12.1)	11.6 (10.0-12.8)	10.1 (8.7-11.6)	10.6 (9.9-11.2)	**12.4** (12.0-13.1)	10.8 (10.7-11.3)
	PTV$_{Total}$	CI [%]	146.4 (143.3-147.5)	**149.8** (145.3-153.2)	148.0 (142.4-150.2)	151.0 (148.0-159.1)	154.5 (146.8-161.8)	152.4 (146.2-159.2)	131.2 (127.1-136.5)	**133.4** (128.6-139.8)	129.5 (125.5-136.7)
OAR mean dose	Parotid gland, CL [Gy]		20.8 (16.9-25.1)	20.6 (16.5-24.2)	20.4 (16.1-23.1)	21.1 (19.7-28.9)	21.1 (18.8-28.6)	**18.2** (18.2-27.3)	26.7 (25.4-28.3)	26.1 (24.4-28.6)	**25.4** (24.0-27.0)
	Parotid gland, IL [Gy]		24.6 (19.5-26.1)	24.8 (19.7-26.4)	**24.0** (18.7-25.1)	37.4 (33.9-38.8)	38.4 (34.3-38.2)	**35.6** (33.1-37.5)	48.0 (42.8-51.1)	48.6 (44.6-51.7)	47.8 (42.5-50.1)
	PCM, Superior [Gy]		40.0 (35.2-46.4)	**40.4** (36.2-47.8)	38.7 (34.5-46.5)	67.9 (65.8-68.5)	68.0 (66.0-68.8)	67.9 (66.1-68.6)	65.1 (63.4-68.8)	64.5 (63.2-68.5)	64.4 (62.8-68.6)
	PCM, Middle [Gy]		67.1 (58.3-70.2)	66.7 (58.7-69.9)	66.3 (58.3-70.2)	41.7 (39.6-53.9)	41.9 (39.9-53.1)	**41.1** (39.0-52.8)	47.5 (39.5-56.5)	48.0 (40.3-55.9)	**47.0** (38.5-55.7)
	PCM, Inferior [Gy]		69.0 (64.1-69.6)	68.9 (63.6-69.2)	68.8 (63.1-69.6)	31.0 (29.5-41.7)	31.9 (28.5-41.5)	**29.5** (26.8-38.4)	35.7 (31.4-39.3)	36.4 (30.6-41.3)	**34.5** (29.2-37.9)
	Supragl. larynx [Gy]		70.1 (70.0-70.2)	69.9 (69.9-69.9)	69.8 (69.8-70.0)	45.4 (38.6-47.3)	45.9 (38.6-47.6)	45.2 (36.8-45.6)	43.4 (41.5-45.6)	44.7 (40.9-46.0)	**42.3** (39.9-43.7)
	Glottic area [Gy]		69.9 (69.6-70.1)	70.0 (69.6-70.0)	69.7 (69.6-70.1)	32.5 (27.7-35.6)	31.8 (28.0-35.8)	**29.3** (26.7-33.4)	33.6 (30.0-37.0)	33.9 (30.7-37.6)	**31.8** (27.8-36.1)
	Oral cavity [Gy]		23.1 (18.1-27.9)	23.2 (17.2-29.8)	**22.4** (16.4-27.4)	50.0 (46.6-53.5)	49.8 (45.7-52.8)	**48.4** (44.7-51.3)	46.5 (42.9-51.4)	48.4 (43.7-51.1)	45.8 (42.7-50.8)
	Subm. gland, CL [Gy]		48.0 (45.4-52.0)	47.4 (45.0-52.7)	45.5 (43.6-51.1)	51.9 (49.7-58.1)	51.0 (49.3-59.4)	50.9 (47.9-58.3)	60.0 (58.9-60.9)	59.9 (58.3-60.4)	59.0 (57.8-60.0)
	Subm. gland, IL [Gy]		56.0 (51.0-58.5)	55.8 (51.7-58.2)	**54.8** (50.7-57.7)	69.0 (66.3-70.2)	69.4 (66.4-69.9)	69.1 (66.2-69.8)	64.6 (62.4-66.7)	64.0 (61.6-66.3)	**63.7** (61.1-65.4)
NTCP	Xerostomia* [%]		38.6 (34.3-43.4)	38.3 (33.9-42.4)	38.1 (33.5-41.2)	38.9 (37.3-47.9)	38.9 (36.4-47.5)	**37.0** (35.7-46.0)	45.3 (43.8-47.2)	44.6 (42.6-47.5)	**43.8** (42.2-45.7)
	Dysphagia** [%]		22.4 (18.4-30.5)	**22.4** (19.2-31.5)	**20.8** (17.7-30.0)	36.5 (31.7-39.2)	37.0 (31.4-41.4)	35.8 (29.9-38.8)	31.1 (27.4-38.0)	31.1 (27.1-38.1)	**29.0** (25.9-36.2)

Abbreviations: OAR = organ at risk; NTCP = normal tissue complication probability; TB2 = VMAT on a C-arm linac using 2 arcs; HA2 & HA3 = VMAT on a fast-rotating O-ring linac using 2 and 3 arcs, respectively; PTV = planning target volume; D$_{xx\%}$ = dose covering xx% of the target volume; HI = homogeneity index according to ICRU 83 [18]; CI = conformity index calculated as the ratio of the volume enclosed by the 95% isodose to the volume of the considered PTV [25]; CL = contralateral; IL = ipsilateral; PCM = pharyngeal constrictor muscle; Supragl. = supraglottic; Subm. = submandibular.

The median values are shown, together with the 1st and 3rd quartile (between brackets). HA2- and HA3-metrics yielding p < 0.05 for a Wilcoxon matched-pairs signed-rank test compared to TB2 are shown in **bold**.
* Grade 2-4 patient-rated xerostomia after 6 months [19].
** Grade 2-4 physician-rated dysphagia after 6 months [20].

Patient-specific bolus for range shifter air gap reduction in intensity-modulated proton therapy of head-and-neck cancer studied with Monte Carlo based plan optimization

III

Michiels S, Barragán A M, Souris K, Poels K, Crijns W, Lee J A, Sterpin E, Nuyts S, Haustermans K, Depuydt T.

Abstract

Background & purpose

Intensity-modulated proton therapy (IMPT) of superficial lesions requires pre-absorbing range shifter (RS) to deliver the more shallow spots. RS air gap minimization is important to avoid spot size degradation, but remains challenging in complex geometries such as in head-and-neck cancer (HNC). In this study, clinical endpoints were investigated for patient-specific bolus and for conventional RS solutions, making use of a Monte Carlo (MC) dose engine for IMPT optimization.

Methods and Materials

For 5 oropharyngeal cancer patients, IMPT spot maps were generated using beamlets calculated with MC. The plans were optimized for three different RS configurations: 3D printed on-skin bolus, snout- and nozzle-mounted RS. Organ-at-risk (OAR) doses and late toxicity probabilities were compared between all configuration-specific optimized plans.

Results

The use of bolus reduced the mean dose to all OARs compared to snout and nozzle-mounted RS. The contralateral parotid gland and supraglottic larynx received on average 2.9 Gy and 4.2 Gy less dose compared to the snout RS. Bolus reduced the average probability for xerostomia by 3.0%. For dysphagia, bolus reduced the probability by 2.7%.

Conclusions

Quantification of the dosimetric advantage of patient-specific bolus shows significant reductions compared to conventional RS solutions for xerostomia and dysphagia probability. These results motivate the development of a patient-specific bolus solution in IMPT for HNC.

Proton therapy (PT) can offer improved organ-at-risk (OAR) sparing compared to state-of-the-art photon radiotherapy. Combined with cost reduction of modern intensity-modulated proton therapy (IMPT) systems, this expected clinical advantage is currently driving a rapid increase in the number of proton therapy facilities [1]. Randomized clinical trials are being established for a wide range of indications [2]. For the often complex geometries of head-and-neck cancer (HNC) for instance, with close proximity of various OARs to the target volume, the improved conformity of IMPT is expected to result in reduced treatment-related side-effects [3,4].

In IMPT with pencil beam scanning (PBS), pencil beam spots are magnetically scanned across the target volume. The depths at which these spots are delivered, are selected layer-by-layer by varying the energy. Modern PT systems however are limited in the minimal energy they can deliver, ranging from 60 to 100 MeV which corresponds to a minimal range in water between 3.1 and 7.7 cm. For the treatment of more superficial lesions, such as in HNC, a pre-absorbing range shifter (RS) is typically attached to the nozzle. The air gap between the RS and the patient however is known to increase the PBS spot size, which can compromise the dose conformity of IMPT [5–7]. Also, various authors have reported on the sub-optimal modelling of RS air gaps by current treatment planning systems (TPS) [8,9].

To minimize these air gap effects, the RS is often positioned as close as possible to the patient using a movable snout extension. Careful attention however is needed to avoid any collision, especially when applying couch adjustments based on image guidance during patient positioning. Both et al. [10] implemented a universal bolus RS, a U-shape with a constant thickness positioned around the patient's head. Universal bolus' application mainly lies in cranial applications and is not always suited for HNC, since often the elective nodes extend beyond the lung apices. Also, such universal bolus has been reported to limit the close positioning of a prompt gamma camera, reducing the obtained useful signal for in-vivo range verification in clinical conditions [11].

Novel solutions for on-skin range shifting tailored to the patient treatment would avoid air gaps altogether and could simplify the workflow for IMPT in HNC. The emerging

3D printing technology is already in clinical use for the creation of individualized devices such as bolus for electron radiotherapy [12]. This technology could also be used to create patient-specific range shifting bolus for IMPT, applicable to the complex curved geometries encountered in HNC while still allowing full flexibility in the selection of treatment beam angles. The use of 3D printing may also enable integration of bolus RS within the patient immobilization. Such integrated approach would ensure presence and correct placement of the RS for each IMPT treatment field. Issues related to the design and construction of such devices are subject of dedicated, ongoing studies and are not within the scope of this work.

In order to justify further investigation of 3D printed on-skin RS, the current study focused on the quantification of the dosimetric benefit compared to conventional RS solutions with air gaps. Although the influence of an air gap on the spot size has been subject of previous publications [13,14], the actual deteriorating effects on dose distributions and treatment plan quality were yet to be quantified. IMPT plan optimization in this study was fully based on Monte Carlo (MC) calculated beamlets to accurately account for RS air gap effects. The aim of this study was to quantify the potential gain of individualized bolus in terms of OAR sparing and normal tissue complication probability (NTCP) reduction in IMPT of HNC.

III.1 Materials and methods

III.1.1 Patient data and planning objectives

Computed tomography (CT) data of 5 patients with oropharyngeal cancer were used for the treatment planning study. A dose of 66 Gy_{RBE} (assuming a constant radiobiologic effectiveness RBE of 1.1) was prescribed to the high-risk clinical target volume (CTVHigh; primary tumour and positive neck levels) and 54 Gy_{RBE} to the low-risk CTV (CTV$_{Low}$; elective neck levels), to be delivered in a simultaneously integrated boost scheme of 30 fractions [15,16]. Planning target volumes (PTV) were defined as the CTVs with a 5 mm margin [16,17].

The PTV constraints were such that 98% of the volume received more than 95% of the prescribed dose D_{Prescr} ($D_{98\%} \geq 95\%$) and that no more than 2% of the volume received more than 107% ($D_{2\%} \leq 107\%$) [15,18,19]. The constraint on the spinal cord was a maximum dose of 40 Gy. A minimum mean dose D^{Mean} was used as objective for the

parotid glands, submandibular glands, oral cavity, larynx, supraglottic larynx and superior pharyngeal constrictor muscle (PCM$_{Sup}$).

III.1.2 Range shifter configurations and plan optimization

A 3-beam arrangement with gantry angles 50, 180 and 310 degrees was used [16], with RS of 4 cm PMMA. For each patient, 3 different RS configurations were compared: applied as bolus or mounted either on a snout or on the nozzle. The bolus was created by expanding the body contour 4 cm parallel to the beam axis for each field. A 3 mm air gap was maintained between the body contour and the bolus to include the potential effect of non-ideal bolus set-up on the spot size in the modelling. For the snout RS, an extendable device attached to the nozzle that can hold accessories such as a RS or an aperture, a 25 cm diameter was chosen. This was the minimum size required to cover the total PTV for every gantry angle. For the nozzle RS, dimensions of 40x30 cm² were adopted from an IBA (Ion Beam Applications, Louvain-la-Neuve, Belgium) dedicated nozzle. For both the snout and nozzle RS, a safety distance, equal to the shortest distance between the RS and the patient, was maintained at 3 cm, to avoid collision with the patient (see Figure 1). This translated into a maximum air gap of 10 cm and 12 cm for the snout and nozzle, respectively, on the more cranially located slices.
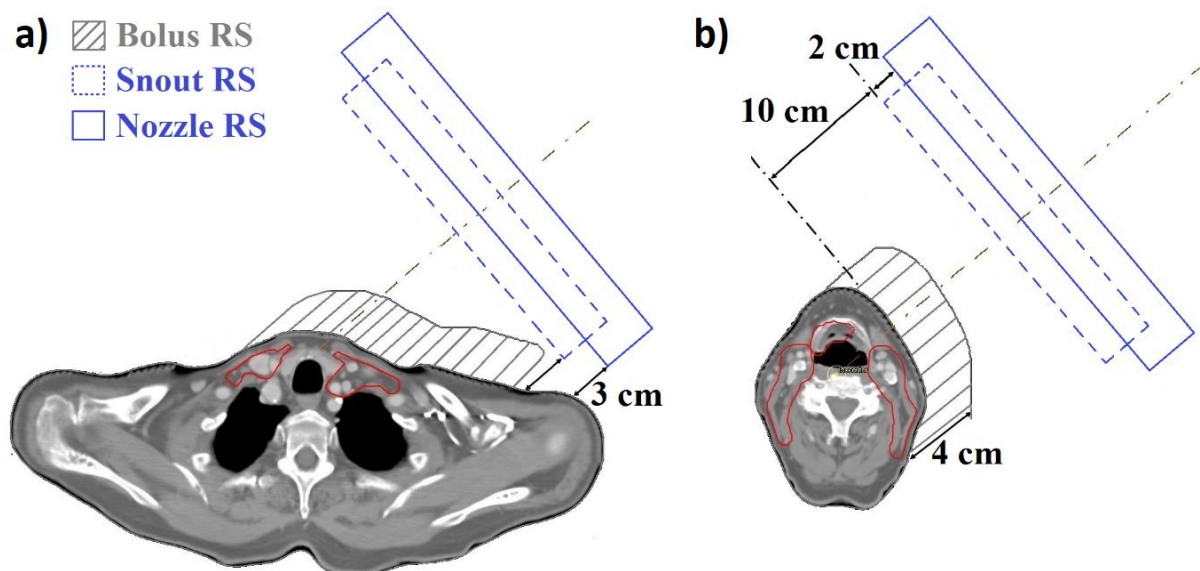
Figure 1. Range shifter (RS) applied as bolus, mounted on a snout or on the nozzle. **a)** A 3 mm air gap was maintained between the body contour and the bolus RS to include non-ideal set-up in the modelling. A 3 cm safety gap was maintained for the snout and nozzle RS to avoid collision with the patient. **b)** This translated into a maximum air gap of 10 cm and 12 cm, respectively, on the more cranially located slices.

III.1.3 Treatment planning system and MC dose engine

To achieve the desired plan constraints ($D_{98\%} \geq 95\%$ of D_{prescr}) for the IMPT plans, an in-house TPS, MIROpt, was used for all RS configurations. MIROpt is fully coupled with the MC dose engine MCsquare, which has been validated in heterogeneous geometries [20] against GATE/GEANT4 [21], allowing to accurately model the effect of RS multiple Coulomb scattering (MCS) and density heterogeneities within the patient. A clinical PBS system was modelled in MCsquare to reproduce commissioning data [21]. Initial spot sizes in air at isocenter were $\sigma = 7$ mm at 70 MeV and $\sigma = 2.5$ mm at 230 MeV.

In MIROpt, spots were placed on a hexagonal grid with 5 mm lateral spot spacing and 5 mm layer spacing. A CT number to tissue parameter conversion was applied to each voxel [22]. The dose deposition matrix was computed with MCsquare using 5×10^4 protons per spot. Simultaneous optimization of all spot weights was done using the large-scale non-linear solver IPOPT [23]. A final MCsquare forward dose calculation was performed with 5×10^8 protons on a $2 \times 2 \times 2$ mm³ dose grid. A median statistical uncertainty of 0.19 Gy was found for the PTV voxels using a batch method [24].

III.1.4 Evaluation of different RS configurations

Target doses and OAR doses were compared between the patient-specific bolus, nozzle-mounted and snout-mounted RS configurations. In addition, expected endpoints for late toxicity in head-and-neck cancer patients receiving radiotherapy were evaluated in terms of their normal issue complication probability (NTCP). The probability of salivary flow <25% of pre-treatment after 1 year for the individual parotid glands was quantified based on Dijkema et al. [25]. Grade 2-4 patient-rated xerostomia probability after 6 months was calculated based on Beetz et al. [26]. Grade 2-4 physician-rated dysphagia probability after 6 months was calculated based on Christianen et al. [27].

III.2 Results

For the bolus plans, the average number of spots per field was 8596. The delivered energies ranged from 75 MeV to 207 MeV. Table 1 shows the target coverage metrics when the spot maps are optimized for each RS configuration individually, hence taking

into account the air gap during optimization. The planning objectives for the PTVs were achieved for all RS configurations. The PTV homogeneity index however, calculated according to ICRU report 83 [19], was slightly higher for the snout and nozzle RS. More distinctively, achieving target coverage for the RS configurations with air gap (snout and nozzle RS) came at the expense of a decreased radiation conformity index as calculated according to Knöös et al [28]. This resulted in an increased mean dose to all parallel OARs, as shown in Table 2. The mean dose to the contralateral parotid gland, for instance, increased on average by 2.9 Gy (snout RS) and 3.4 Gy (nozzle RS). The Dmean to the supraglottic larynx increased by 4.2 Gy (snout RS) and 5.5 Gy (nozzle RS). The dose distributions and dose-volume histograms for one representative patient are shown in Figure 2.

Table 3 shows the NTCP predictions for the different RS configurations. Averaged over the patients, the use of patient-specific on-skin bolus reduced the probability of individual parotid gland dysfunction [25] by 3.5% (ipsilateral) and 3.0% (contralateral) compared to the snout RS and by 5.0% (ipsilateral) and 3.8% (contralateral) compared to the nozzle RS. The probability of xerostomia [26] with a bolus was 3.1% and 3.6% lower compared to a snout and nozzle RS, respectively. A similar trend was seen for the probability of dysphagia with on-skin bolus RS (respectively -2.7% and -3.6% compared to snout RS and nozzle RS).

Table 1. Target coverage metrics for the RS configuration-specific optimized plans.

	CTV$_{Low}$		PTV$_{Low}$			CTV$_{High}$		PTV$_{High}$		
	HI [-] *	D$_{50}$ [Gy]	RCI [-] **	HI [-]	D$_{50}$ [Gy]	HI [-]	D$_{50}$ [Gy]	RCI [-]	HI [-]	D$_{50}$ [Gy]
Bolus RS	0.28	55.9	0.58	0.24	55.3	0.11	67.1	0.86	0.12	67.0
	(0.18, 0.32)	(54.9, 57.3)	(0.43, 0.79)	(0.11, 0.33)	(54.5, 57.2)	(0.10, 0.12)	(66.8, 67.2)	(0.81, 0.91)	(0.12, 0.13)	(66.7, 67.3)
Snout RS	0.28 (p=0.31)	55.8 (p=0.39)	**0.55 (p=0.02)**	**0.25 (p=0.02)**	**55.5 (p=0.004)**	0.11 (p=0.15)	**67.3 (p=0.03)**	**0.84 (p=0.007)**	**0.12 (p=0.02)**	**67.2 (p=0.01)**
	(0.19, 0.32)	(55.0, 57.1)	(0.42, 0.73)	(0.11, 0.33)	(54.8, 57.3)	(0.10, 0.12)	(67.0, 67.6)	(0.79, 0.88)	(0.12, 0.13)	(66.9, 67.5)
Nozzle RS	0.27 (p=0.90)	55.9 (p=0.46)	**0.55 (p=0.01)**	**0.25 (p=0.02)**	**55.6 (p=0.001)**	0.11 (p=0.15)	67.7 (p=0.1)	**0.82 (p=0.003)**	**0.12 (p=0.01)**	**67.2 (p=0.01)**
	(0.19, 0.31)	(55.1, 57.3)	(0.42, 0.73)	(0.11, 0.33)	(54.9, 57.4)	(0.10, 0.12)	(66.9, 69.2)	(0.77, 0.88)	(0.12, 0.13)	(66.9, 67.5)

All plans were optimized for a PTV coverage $D_{98\%} \geq 95\%$ D_{Prescr}, corresponding to 51.3 Gy for PTV$_{Low}$ and 62.7 Gy for PTV$_{High}$. Metrics are shown averaged over all the patients, together with the range values (between brackets). p-Values are for a single-sided paired t-test and are shown in **bold** when below 0.05.

Two patients had positive neck disease. The median volume of PTV$_{High}$ and PTV$_{Low}$ was 148 cm³ and 393 cm³, respectively.

Abbreviations: RS = range shifter; PTV = planning target volume; $D_{xx\%}$ = dose covering xx% of the target volume; D_{Prescr} = prescribed dose; CTV = clinical target volume; PTV = planning target volume.

(*) The homogeneity index (HI) was determined according to ICRU report 83 [19]. The closer to zero, the better the homogeneity
(**) The radiation conformity index (RCI) was determined according to Knöös et al. [28] based on 50% (for PTV$_{Low}$) and 95% (for PTV$_{High}$) isodoses. The closer to one, the better the conformity.

Table 2. Organ-at-risk doses for the RS configuration-specific optimized plans.

	Parotid gland, Ipsi	Parotid gland, Contra	Subm. gland, Ipsi	Subm. gland, Contra	PCM, Superior	Supraglottic larynx	Larynx	Oral cavity	Spinal cord
	D_{mean} [Gy]	D_{mean} [Gy]	D_{mean} [Gy]	D_{mean} [Gy]	D_{mean} [Gy]	D_{mean} [Gy]	D_{mean} [Gy]	D_{mean} [Gy]	D_{max} [Gy]
Bolus RS	20.6	14.8	65.2	34.3	56.8	18.8	25.5	35.7	30.4
	(9.0, 32.8)	(3.7, 25.0)	(62.7, 66.6)	(22.3, 50.2)	(47.4, 64.8)	(8.6, 36.0)	(15.9, 38.2)	(28.6, 41.2)	(20.6, 40.2)
Snout RS	**23.4** (p=0.001)	**17.7** (p=0.001)	66.2 (p=0.12)	**37.3** (p=0.007)	**58.7** (p=0.01)	**23.0** (p=0.001)	**30.3** (p=0.004)	**38.3** (p=0.001)	32.11 (p=0.11)
	(11.0, 36.5)	(5.1, 28.7)	(62.8, 70.3)	(23.5, 55.4)	(47.9, 68.2)	(10.9, 41.5)	(19.4, 44.2)	(30.4, 44.7)	(23.3, 40.5)
Nozzle RS	**24.3** (p=0.001)	**18.2** (p=0.001)	66.5 (p=0.11)	**38.7** (p=0.002)	**59.2** (p=0.01)	**24.3** (p=0.001)	**31.5** (p=0.001)	**39.0** (p=0.001)	32.9 (p=0.09)
	(11.9, 37.9)	(5.6, 29.6)	(62.8, 71.0)	(24.1, 56.3)	(47.9, 69.1)	(12.6, 42)	(20.4, 44.7)	(31.2, 45.5)	(25.5, 40.7)

Metrics are shown averaged over all the patients, together with the range values (between brackets). p-Values are for a single-sided paired t-test and are shown in **bold** when below 0.05.

Abbreviations: RS = range shifter; Ipsi/Contra = ipsi-/contralateral; Subm. = submandibular; PCM = pharyngeal constrictor muscle.

Table 3. Normal tissue complication probability-values for the RS configuration-specific optimized plans.

	Ipsilateral PG dysfunction* [%]	Contralateral PG dysfunction* [%]	Xerostomia ** [%]	Dysphagia*** [%]
Bolus RS	15.0 (2.4, 32.8)	7.2 (2.4, 32.8)	32.6 (22.0, 43.3)	11.8 (5.9, 25.1)
Snout RS	**18.5** (p=0.014) (3.5, 39.5)	**10.2** (p=0.021) (2.7, 38.7)	**35.7** (p=0.003) (23.1, 47.4)	**14.5** (p=0.002) (7.5, 29.0)
Nozzle RS	**20.0** (p=0.015) (3.7, 41.9)	**11.0** (p=0.022) (2.9, 40.7)	**36.2** (p=0.002) (23.6, 48.4)	**15.4** (p=0.001) (8.4, 29.6)

Metrics are shown averaged over all the patients, together with the range values (between brackets). p-Values are for a single-sided paired t-test and are shown in **bold** when below 0.5.

(*) Individual parotid gland (PG) salivary flow < 25% of pre-treatment [25].
(**) Grade 2-4 patient-rated xerostomia after 6 months [26].
(***) Grade 2-4 physician-rated dysphagia after 6 months [27].
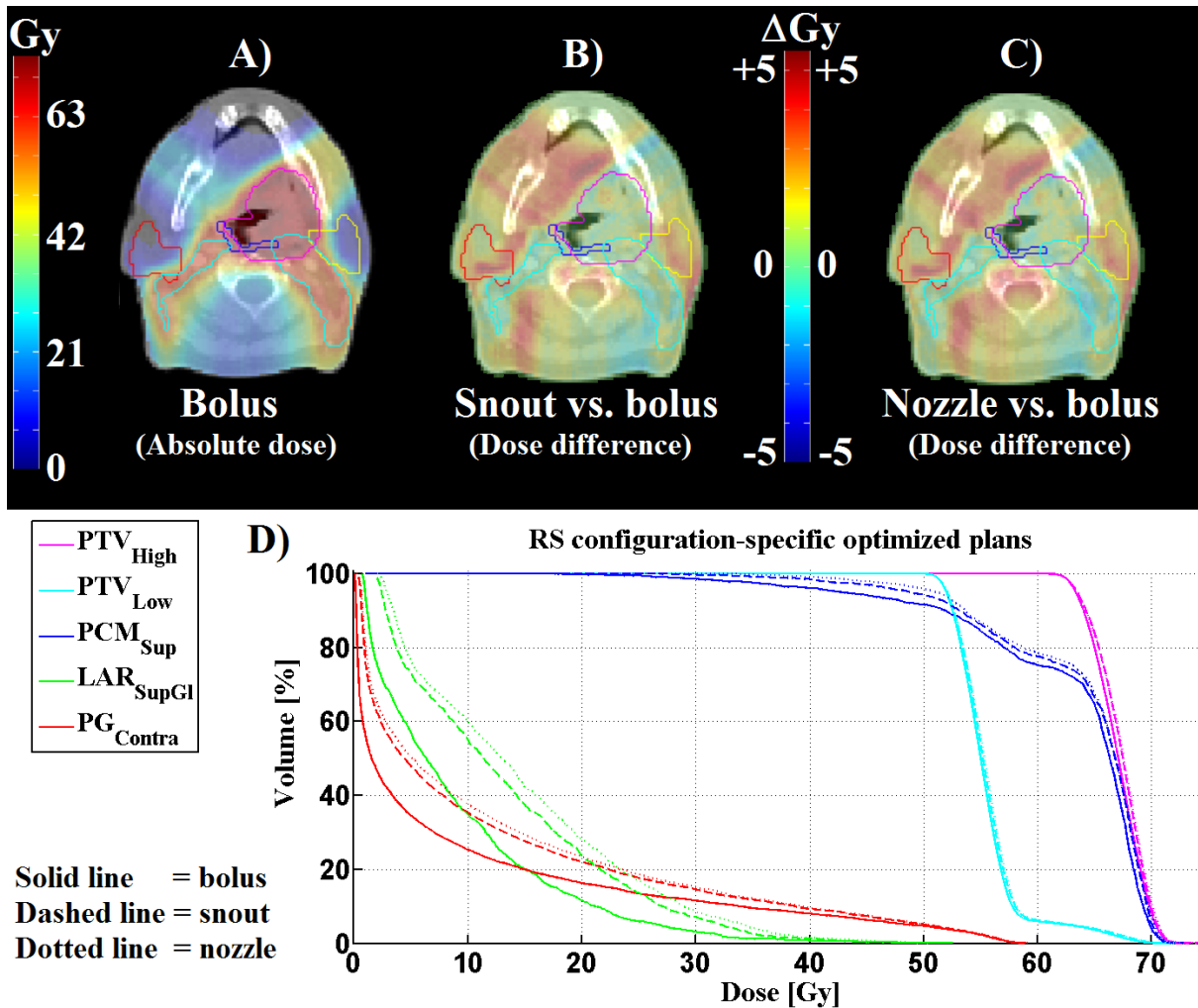
Figure 2. Dose distributions and dose-volume histograms for the RS configuration-specific optimized plans for one patient.

All plans were optimized for a PTV coverage $D_{98\%} \geq 95\%$ D_{Prescr}, corresponding to 51.3 Gy for PTV_{Low} and 62.7 Gy for PTV_{High}. For the snout and nozzle RS configuration, dose difference distributions relative to the bolus configuration are given.

Abbreviations: RS = range shifter; PTV = planning target volume; $D_{xx\%}$ = dose covering xx% of the target volume; D_{Prescr} = prescribed dose; PCM_{Sup} = superior pharyngeal constrictor muscle; LAR_{SupGl} = supraglottic larynx; PG = parotid gland; Contra = contralateral.

III.3 Discussion

In this study, the impact of RS air gaps on plan quality was investigated for IMPT of HNC. Although the influence of air gap on the spot size has been subject of previous publications [13,14], to our knowledge this is the first quantification of the dosimetric effects at actual patient level for HNC. Conventional snout-/nozzle-mounted RS were compared to a no-air-gap configuration by applying RS as patient-specific on-skin bolus. In this regard, it was shown that individualized bolus can considerably improve plan quality, with significant reductions in NTCP. The used safety gap of 3 cm for the conventional RS configurations can be considered at the limit of what is acceptable in terms of safety. A more conservative safety gap would result in larger air gaps for the conventional RS configurations, with an even more pronounced dosimetric advantage for the bolus configuration.

Although the planning parameters used in this study were based on literature [15–19], one could argue that for heterogeneous sites such as HNC robust planning methods [29,30] would be more suitable than a PTV approach. A margin expansion indeed increases the dose to the OARs, potentially shifting the generated plans upwards on the considered NTCP curves. On the other hand, robust optimization might increase the weight of spots at superficial depths, where the lateral penumbra is dominated by the initial spot size rather than by MCS in the patient [13], which in turn might enhance the advantage of bolus over nozzle-/snout-mounted RS. In any case, as the air gap effects do not change with the way treatment uncertainties are dealt with, the adopted approach should provide a fair basis to compare the simulated RS configurations.

Given that various authors have reported on the sub-optimal modelling of RS by clinical TPS [7,8,31], IMPT plan optimization in this study is fully based on MC calculated beamlets to accurately account for RS air gap effects. The current study is therefore representative for dose calculation with the newest generation of TPS which includes MC. It was shown that plan optimization using MC-calculated beamlets cannot fully compensate for OAR dose increase due to spot degradation. This indicates the clinical relevance of air gap reduction, which is currently pursued in clinical practice but can complicate the clinical workflow. Air gap reduction by positioning the RS as close as possible to the patient using a snout requires additional hardware manipulation for each individual field resulting in additional set-up time. In addition,

careful attention is needed to avoid any collision of the snout RS with the patient, especially when applying couch adjustments based on image guidance during patient positioning. Irradiating smaller areas at a time by splitting the fields in the craniocaudal direction can enhance gap reduction options, but requires robust field matching and results in higher treatment times due to the couch position adjustments needed between different fields.

A recent alternative approach for the reduction of air gap effects is the in-axis 'beam splitting' technique [7], in which a field is split along the beam axis into two sub-beams: one with RS for the proximal layers and one without RS for the remaining layers. Since this allows to only use the RS when actually needed, better spot penumbra than conventional RS solutions can be achieved resulting in increased kidney sparing in craniospinal irradiation with PT [7]. On the other hand, the spot degradation however is still present for the spots with lower energies, where spot sizes typically are already largest. Nevertheless, such technique can be a beneficial approach, for which the feasibility will depend on a number of factors, such as the physician's policy with respect to creating in-field junctions in a target volume, the presence of OARs in the shallow layers and the weight of the spots with lower energies. On a whole, the selection of a beam splitting approach or an individualized bolus approach ideally would be made indication- or even patient-specific.

Complete elimination of the air gap could be achieved by bolus RS, for which the improvement in plan quality was shown in this study. Other potential advantages compared to snout-/nozzle-mounted RS can be identified, such as improved safety and more efficient treatment workflow due to reduced hardware movements. The flexibility needed to create patient-specific bolus for challenging geometries such as in HNC could be provided by 3D printing technology. Michiels et al. [32] provided a proof of concept for PT range shifting using 3D printed materials. Investigation on the development of patient-specific RS is currently ongoing and the results found in this paper support these efforts.

Clinical implementation of patient-specific 3D printed bolus for IMPT would require to attend to a number of practical challenges. Expectations about the matching of 3D-printed bolus to the body contour, for instance, should be realistic. To include the effect

of non-ideal bolus set-up on the spot size in the modelling, a 3 mm air gap was maintained between the body contour and the bolus in current study. To assess the dosimetric impact of uncertainty in the bolus positioning relative to the patient, the bolus plan was recalculated on a number of perturbed geometries for one patient. For a systematic shift of the bolus with 2 mm in each direction individually, the impact on the target coverage and on the OAR dose was found comparable with the statistical uncertainty on the dose calculation (data not shown). Moreover, the increasing utilization of surface monitoring techniques should allow to keep the bolus positioning error well below the simulated perturbation [33,34]. An integrated approach, where the RS and the immobilization functionality are combined within one structure, could also aid in reducing the uncertainty in the bolus positioning.

All things considered, RS bolus implementation hindrances and costs should be weighed against the achievable workflow efficiency improvements and NTCP reductions. Although the current NTCP-models have been established using only photon radiotherapy treatment data, the used dysphagia and xerostomia models performed reasonably well (area under the curve ≥ 0.7) in an external validation with PT [35]. Using these models, the improved plan quality achieved with bolus RS yielded significant NTCP reductions compared to snout- and nozzle-mounted RS for individual parotid gland dysfunction, xerostomia and dysphagia. Though patient selection thresholds for the model-based comparison of IMPT with photon techniques are yet to be defined [36,37], these improved NTCP reductions with bolus could increase the overall number of HNC patients eligible for IMPT.

In conclusion, accounting for the air gap in IMPT plan optimization using MC dose calculation cannot fully cancel out the impact of spot degradation on OAR dose. Quantification of the dosimetric advantage of patient-specific bolus compared to conventional snout-/nozzle-mounted RS solutions yields significant reductions for parotid gland dysfunction, xerostomia and dysphagia probability. These results motivate the development of a patient-specific bolus solution in IMPT for oropharyngeal cancer.

Acknowledgments

References

[1]   Durante M, Paganetti H. Nuclear physics in particle therapy: a review. Rep Prog Phys 2016;79:096702.

[2]   Mishra M V., Aggarwal S, Bentzen SM, Knight N, Mehta MP, Regine WF. Establishing evidence-based indications for proton therapy: An overview of current clinical trials. Int J Radiat Oncol Biol Phys 2017;97:228–35.

[3]   Van De Water TA, Lomax AJ, Bijl HP, De Jong ME, Schilstra C, Hug EB, et al. Potential benefits of scanned intensity-modulated proton therapy versus advanced photon therapy with regard to sparing of the salivary glands in oropharyngeal cancer. Int J Radiat Oncol Biol Phys 2011;79:1216–24.

[4]   Eekers DBP, Roelofs E, Jelen U, Kirk M, Granzier M, Ammazzalorso F, et al. Benefit of particle therapy in re-irradiation of head and neck patients. Results of a multicentric in silico ROCOCO trial. Radiother Oncol 2015;121:387–94.

[5]   Safai S, Bortfeld T, Engelsman M. Comparison between the lateral penumbra of a collimated double-scattered beam and uncollimated scanning beam in proton radiotherapy. Phys Med Biol 2008;53:1729–50.

[6]   Titt U, Mirkovic D, Sawakuchi GO, Perles LA, Newhauser WD, Taddei PJ, et al. Adjustment of the lateral and longitudinal size of scanned proton beam spots using a pre-absorber to optimize penumbrae and delivery efficiency. Phys Med Biol 2010;55:7097–106.

[7]   Farace P, Bizzocchi N, Righetto R, Fellin F, Fracchiolla F, Lorentini S, et al. Supine craniospinal irradiation in pediatric patients by proton pencil beam scanning. Radiother Oncol 2017;123:112–8.

[8]   Fracchiolla F, Lorentini S, Widesott L, Schwarz M. Characterization and validation of a Monte Carlo code for independent dose calculation in proton therapy treatments with pencil beam scanning. Phys Med Biol 2015;60:8601–19.

[9]   Barten DLJ, Tol JP, Dahele M, Slotman BJ, Verbakel WFAR. Comparison of organ-at-risk sparing and plan robustness for spot-scanning proton therapy and volumetric modulated arc photon therapy in head-and-neck cancer. Med Phys 2015;42:6589–98.

[10]   Both S, Shen J, Kirk M, Lin L, Tang S, Alonso-Basanta M, et al. Development and clinical implementation of a universal bolus to maintain spot size during delivery of base of skull

pencil beam scanning proton therapy. Int J Radiat Oncol Biol Phys 2014;90:79–84.

[11] Xie Y, Bentefour H, Janssens G, Smeets J, Stappen F Vander, Hotoiu L, et al. Prompt gamma imaging for in vivo range verification of pencil beam scanning proton therapy. Int J Radiat Oncol 2017;99:210–8.

[12] Canters RA, Lips IM, Wendling M, Kusters M, Van Zeeland M, Gerritsen RM, et al. Clinical implementation of 3D printing in the construction of patient specific bolus for electron beam radiotherapy for non-melanoma skin cancer. Radiother Oncol 2016;121:148–53.

[13] Titt U, Mirkovic D, Sawakuchi GO, Perles LA, Newhauser WD, Taddei PJ, et al. Adjustment of the lateral and longitudinal size of scanned proton beam spots using a pre-absorber to optimize penumbrae and delivery efficiency. Phys Med Biol 2010;55:7097–106.

[14] Safai S, Bortfeld T, Engelsman M. Comparison between the lateral penumbra of a collimated double-scattered beam and uncollimated scanning beam in proton radiotherapy. Phys Med Biol 2008;53:1729–50.

[15] van de Water S, van Dam I, Schaart DR, Al-Mamgani A, Heijmen BJM, Hoogeman MS. The price of robustness; impact of worst-case optimization on organ-at-risk dose and complication probability in intensity-modulated proton therapy for oropharyngeal cancer patients. Radiother Oncol 2016;120:56–62.

[16] Kraan AC, Van De Water S, Teguh DN, Al-Mamgani A, Madden T, Kooy HM, et al. Dose uncertainties in IMPT for oropharyngeal cancer in the presence of anatomical, range, and setup errors. Int J Radiat Oncol Biol Phys 2013;87:888–96.

[17] Malyapa R, Lowe M, Bolsi A, Lomax AJ, Weber DC, Albertini F. Evaluation of Robustness to Setup and Range Uncertainties for Head and Neck Patients Treated with Pencil Beam Scanning Proton Therapy. Int J Radiat Oncol Biol Phys 2016;95:154–62.

[18] Van Der Voort S, Van De Water S, Perkó Z, Heijmen B, Lathouwers D, Hoogeman M. Robustness Recipes for Minimax Robust Optimization in Intensity Modulated Proton Therapy for Oropharyngeal Cancer Patients. Int J Radiat Oncol Biol Phys 2016;95:163–70.

[19] ICRU report 83. Prescribing, recording, and reporting photon-beam intensity-modulated radiation therapy (IMRT). vol. 10. Oxford, UK: Oxford University Press; 2010.

[20] Souris K, Lee JA, Sterpin E. Fast multi-purpose Monte Carlo simulation for proton therapy using multi- and many-core CPU architectures. Med Phys 2016;43:1700–12.

[21] Grevillot L, Bertrand D, Dessy F, Freud N, Sarrut D. A Monte Carlo pencil beam scanning model for proton treatment plan simulation using GATE/GEANT4. Phys Med Biol 2011;56:5203–19.

[22] Schneider W, Bortfeld T, Schlegel W. Correlation between CT numbers and tissue parameters needed for Monte Carlo simulations of clinical dose distributions. Phys Med Biol Phys Med Biol 2000;45:459−78.

[23] Wächter A, Biegler LT. On the Implementation of a Primal-Dual Interior Point Filter Line Search Algorithm for Large-Scale Nonlinear Programming. Math Program 2006;106:25−57.

[24] Jia X, Gu X, Graves YJ, Folkerts M, Jiang SB. GPU-based fast Monte Carlo simulation for radiotherapy dose calculation. Phys Med Biol 2011;56:7017−31.

[25] Dijkema T, Raaijmakers CPJ, Ten Haken RK, Roesink JM, Braam PM, Houweling AC, et al. Parotid gland function after radiotherapy: The combined Michigan and Utrecht experience. Int J Radiat Oncol Biol Phys 2010;78:449−53.

[26] Beetz I, Schilstra C, Van Der Schaaf A, Van Den Heuvel ER, Doornaert P, Van Luijk P, et al. NTCP models for patient-rated xerostomia and sticky saliva after treatment with intensity modulated radiotherapy for head and neck cancer: The role of dosimetric and clinical factors. Radiother Oncol 2012;105:101−6.

[27] Christianen MEMC, Schilstra C, Beetz I, Muijs CT, Chouvalova O, Burlage FR, et al. Predictive modelling for swallowing dysfunction after primary (chemo)radiation : Results of a prospective observational study. Radiother Oncol 2012;105:107−14.

[28] Knöös T, Kristensen I, Nilsson P. Volumetric and dosimetric evaluation of radiation treatment plans: Radiation conformity index. Int J Radiat Oncol Biol Phys 1998;42:1169−76.

[29] Fredriksson A, Forsgren A, Hårdemark B. Minimax optimization for handling range and setup uncertainties in proton therapy. Med Phys 2011;38:1672−84.

[30] Unkelbach J, Bortfeld T, Martin BC, Soukup M. Reducing the sensitivity of IMPT treatment plans to setup errors and range uncertainties via probabilistic treatment planning. Med Phys 2009;36:149−63.

[31] Barten DLJ, Tol JP, Dahele M, Slotman BJ, Verbakel WFAR. Comparison of organ-at-risk sparing and plan robustness for spot-scanning proton therapy and volumetric modulated arc photon therapy in head-and-neck cancer. Med Phys 2015;42:6589−98.

[32] Michiels S, D'Hollander A, Lammens N, Kersemans M, Zhang G, Denis J, et al. Towards 3D printed multifunctional immobilization for proton therapy: Initial materials characterization. Med Phys 2016;10:5392−402.

[33] Bert C, Metheany KG, Doppke K, Chen GTY. A phantom evaluation of a stereo-vision surface imaging system for radiotherapy patient setup. Med Phys 2005;32:2753−62.

[34] Bert C, Metheany KG, Doppke KP, Taghian AG, Powell SN, Chen GTY. Clinical experience with a 3D surface patient setup system for alignment of partial-breast irradiation patients. Int J Radiat Oncol Biol Phys 2006;64:1265−74.

[35]   Blanchard P, Wong AJ, Gunn GB, Garden AS, Mohamed ASR, Rosenthal DI, et al. Toward a model-based patient selection strategy for proton therapy: External validation of photon-derived normal tissue complication probability models in a head and neck proton therapy cohort. Radiother Oncol 2016;121:381–6.

[36]   Langendijk JA, Lambin P, De Ruysscher D, Widder J, Bos M, Verheij M. Selection of patients for radiotherapy with protons aiming at reduction of side effects: The model-based approach. Radiother Oncol 2013;107:267–73.

[37]   Widder J, van der Schaaf A, Lambin P, Marijnen CAM, Pignol JP, Rasch CR, et al. The Quest for Evidence for Proton Therapy: Model-Based Approach and Precision Medicine. Int J Radiat Oncol Biol Phys 2016;95:30–6.

Towards range shifter integrated immobilization for proton therapy: Characterization of 3D printed materials

IV

Abstract

Purpose

3D printing technology is investigated for the purpose of patient immobilization during proton therapy. It potentially enables a merge of patient immobilization, bolus range shifting and other functions into one single patient-specific structure. In this first step, a set of 3D printed materials is characterized in detail, in terms of structural and radiological properties, elemental composition, directional dependence and structural changes induced by radiation damage. These data will serve as input for the design of 3D printed immobilization structure prototypes.

Methods & Materials

Using four different 3D printing techniques, in total eight materials were subjected to testing. Samples with a nominal dimension of 20x20x80 mm³ were 3D printed. The geometrical printing accuracy of each test sample was measured with a dial gage. To assess the mechanical response of the samples, standardized compression tests were performed to determine the Young's modulus. To investigate the effect of radiation on the mechanical response, the mechanical tests were performed both prior and after the administration of clinically relevant dose levels (70 Gy), multiplied with a safety factor of 1.4. Dual Energy Computed Tomography (DECT) methods were used to calculate the relative electron density to water ρ_e, the effective atomic number Z_{eff} and the proton stopping power ratio to water SPR. In order to validate the DECT based calculation of radiological properties, beam measurements were performed on the 3D printed samples as well. Photon irradiations were performed to measure the photon linear attenuation coefficients, while proton irradiations were performed to measure the proton range shift of the samples. The directional dependence of these properties was investigated by performing the irradiations for different orientations of the samples.

Results

The printed test objects showed reduced geometric printing accuracy for 2 materials (deviation > 0.25 mm). Compression tests yielded Young's moduli ranging from 0.6 MPa to 2940 MPa. No deterioration in the mechanical response was observed after exposure of the samples to 100 Gy in a therapeutic MV photon beam. The DECT-based characterization yielded Z_{eff} ranging from 5.91 to 10.43. The SPR and ρ_e both ranged

from 0.6 to 1.22. The measured photon attenuation coefficients at clinical energies scaled linearly with ρ_e. Good agreement was seen between the DECT estimated SPR and the measured range shift, except

for the higher Z_{eff}. As opposed to the photon attenuation, the proton range shifting appeared to be printing orientation dependent for certain materials.

Conclusions

In this study, the first step towards 3D printed, multifunctional immobilization was performed, by going through a candidate clinical workflow for the first time: from the material printing to DECT characterization with a verification through beam measurements. Besides a proof of concept for beam modification, the mechanical response of printed materials was also investigated to assess their capabilities for positioning functionality. For the studied set of printing techniques and materials, a wide variety of mechanical and radiological properties can be selected from for the intended purpose. Moreover the elaborated hybrid DECT methods aid in performing in-house Quality Assurance (QA) of 3D printed components, as these methods enable the estimation of the radiological properties relevant for use in radiation therapy.

THE CONTINUOUS IMPROVEMENT OF RADIATION THERAPY TECHNIQUES mainly aims at improved local tumour control with reduced side effects of the treatment. In this pursuit, the use of protons is highly promising due to their advantageous depth dose profile. The finite range and the sharp fall-off of the dose deposition in the Bragg peak enable a potentially better target dose conformity and normal tissue sparing compared to photons. The accurate dose deposition control of proton pencil beam scanning however comes with an increased sensitivity to various range and setup uncertainties [1–3]. As these uncertainties may cause the delivered dose to considerably deviate from the planned dose, effectively dealing with them is the biggest challenge in realising the full potential of proton therapy (PT) [4]. In an effort to increase the PT treatment effectiveness for head-and-neck cancer (HNC), for which intensity-modulated proton therapy (IMPT) is an attractive modality [5,6], novel solutions using 3D printing technology are proposed.

3D printing or additive manufacturing is an appealing technique as it offers a high degree of flexibility in object shaping from a wide range of materials. Large-scaled printers with print bed side lengths of a few meters require a considerable capital investment, but desktop sized printers at entry-level prices have become readily available on the market. A variety of printing techniques exists, which allows to exploit each technique's relative strengths in function of the envisioned application. Fused deposition modeling (FDM) for example can be used to reduce costs in the industrial manufacturing of components, such as lightweight airplane parts. Polyjet™ (PJ) or Stereolithography (SLA) can be selected for applications where the highest achievable printing accuracy is required, such as in the fabrication of patient-specific implants [7] or in the 3D model creation for complex surgery planning [8]. Selective laser sintering (SLS) allows to produce heat-resistant metallic components in complex shapes for example for automotive engine parts. 3D printing in general is increasingly investigated for use in radiotherapy, for the manufacturing of amongst others electron bolus, proton range compensators and range modulator wheels [9–11]. The technology has been considered as well for the construction of anthropomorphic phantoms for dosimetry purposes [12]. We aim to use 3D printing to manufacture a customized immobilization device fitted to the patient's body outlines.

Such a 3D printed device could yield improvements in the accuracy and reproducibility of patient positioning and immobilization during treatment. The current practice of thermoplastic masks can encompass significant inter-fractional variation in the positioning of structures [13,14]. Also, substantial changes occur in the head-and-neck anatomy during the treatment course, with potentially a detrimental influence on the quality of the immobilization hence on the delivered dose distribution [15]. Lastly, certain types of thermoplastic masks are known to shrink after the initial application which can reduce the patient-specificity and can cause patient discomfort. In this regard, the ability to use different 3D printed materials with different degrees of elasticity in patient-specific shapes would enable to pursue a balance between accurate, reproducible immobilization and patient comfort. Moreover a modular approach of the design would allow to reprint substructures in function of the anatomical changes, aiding in implementing an adaptive immobilization.

3D printing could also yield a number of additional treatment enhancements, such as the integration of range shifter (RS) in the immobilization device for the treatment of superficial lesions, i.e. as bolus. The attachment of RS to the nozzle namely causes the presence of an air gap between the nozzle and the patient skin, which is not properly modelled by the current generation of pencil beam dose calculation algorithms [16]. Moreover the air gap length is known to have a strong impact on the lateral dose fall-off of proton beams due to the angular spread created in the RS [17–19] with negative dosimetric consequences. Integrating RS as bolus in the 3D printed device itself would solve this issue, as the air gap would be completely eliminated. Moreover, such an integrated solution would allow a safer clearance between moving gantry parts and patient, eliminating collision risk and allowing for a more time-efficient treatment delivery due to the omission of hardware movements. Lastly, the degrees of freedom in the generated shapes offered by 3D printing could allow to integrate other functionalities besides bolus. In-vivo dosimetry with a high positional accuracy of detectors relative to the patient anatomy for instance comes into reach, which could live up to the strong demand for patient specific dosimetry and QA techniques in IMPT.

Given that the intended device has both a mechanical and radiological functionality, in a first step a broad characterization of possible 3D printed materials and techniques is to be carried out, which is the scope of this paper. Due to the discrete nature of the

printing process, a different overall behaviour of 3D printed materials could be expected compared to the same materials produced in their more established manner. Topics such as dimensional accuracy, mechanical elasticity including its potential change induced by radiation and interaction with protons and photons are covered. Moreover, successful clinical implementation of a device consisting of 3D printed supporting and beam modifying structures requires reliable material assessment methods that fit within the clinical workflow. Therefore Dual-Energy Computed Tomography (DECT) methods for the determination of radiological properties are elaborated and applied to 3D printed materials for the first time. These methods are verified as well by photon attenuation and proton range shift measurements.

IV.1 Materials & Methods

IV.1.1 3D printing technologies and materials

In total eight materials were subjected to testing in this work, using four different printing techniques. An overview of the considered printing techniques and materials is given in Table 1. The FDM process is based on the heating and layering of thermoplastics. A temperature-controlled extrusion head is fed with thermoplastic material, which is heated to a semi-liquid state. The head extrudes and directs the material layer by layer onto a fixtureless base. After being deposited, the material cools down and hardens. The result of the solidified material laminating to the preceding layer is a plastic 3D model built up one layer at a time. The filling degree of the printed object can be varied freely in this technique. As it takes time for the thermoplastic to harden and for the layers to bond together, the use of support structures is required when generating objects with overhanging geometries. An advantage of FDM is that dual-nozzle configurations exist, which allow to create these support structures in water-soluble material. In general this printing technique is the cheapest and most accessible one, but is also the least capable in terms of printing speed, accuracy and surface finish.

The other techniques use a slice by slice technique similar to FDM, but require exposure to laser light for the material to harden or 'cure'. The SLA process uses a tank of liquid polymer resin in which the layers are cured and solidified by an UV laser. In general SLA provides the best accuracy and surface finish. Support structures however are to be removed by hand, which tends to be time-consuming. This printing technique

is mostly used for building large parts or parts where different finishing degrees are required. The PJ technique simultaneously jets multiple photopolymer materials onto a layer on a build tray, after which the layer is immediately cured by an ultraviolet (UV) laser. At the expense of the highest cost, this technique offers multi-material capabilities with fine detail. A trade-off however is that exposure of the materials to ambient heat or humidity can cause dimensional changes. Also these materials in general have limited mechanical properties. Lastly, in the SLS technique powder-based materials are used with particle size in the order of magnitude of 50 μm. Successive powder layers are spread on top of each other on the build platform. After deposition, the particles are selectively bound together by the elevation of the powder temperature due to the exposure to a CO_2 laser beam. This technique offers the possibility to print metallic materials as well. In addition, no support structures are needed as support is provided by the print bed itself, which allows to print complex shapes. On the downside, because of the elevated temperatures required for SLS, cooling times can be considerable. Also the use of particles result in rather rough surfaces.

Table 1. Overview of the considered printing techniques and materials. The manufacturer-quoted maximum part dimensions [20], standard accuracy, printing process layer thickness and used materials are displayed.

Property	Production technique			
	FDM	SLA	PJ	SLS
Max. dimensions [mm³]	914x610x914	2100x700x800	500x400x200	650x330x560
Standard accuracy [μm]	±200	±150	±100-200	±300
Layer thickness [μm]	100-300	50-200	16-32	60-180
Materials	ABS	TuskXC2700T	TangoPlus VeroWhite	PolyAmide (PA)-12 PA-Alumide PA-GlassFibre TPU

IV.1.2 Printing of test object samples

In order to perform the different characterization methods, two identical test objects were printed for each of the eight materials. A specified dimension of 20x20x80 mm³ was used. The actual dimensions of each sample were measured with a dial gauge (model: 2046S – Mitutoyo, Kawasaki) with a spatial resolution of 10 μm, and

compared with the specified nominal values. The distance between the 20x20 mm² faces was measured at one central point. The distance between the 20x80mm² faces was measured at 6 points distributed equally over the surface.

IV.1.3 Mechanical response measurements

In order to assess the mechanical response of the 3D printed samples, compression tests were performed to determine the Young's modulus. To investigate the effect of radiation on the mechanical response, the compression tests were performed both prior and after the administration of clinically relevant dose levels, multiplied with a safety factor.

<u>Compression tests - Young's modulus</u>

The samples were compression tested according to the ASTM D695 standard [21] in a tensile testing machine (model: 5800R – Instron, Norwood, MA). Three linear variable differential transformers were used to measure the displacement between top and bottom face of the compression plates. To avoid plastic deformation of the samples, the applied strain levels were kept as low as possible. For the stiff materials (> 100 MPa), the compressive strain level was limited to 0.5% and the loads were recorded with a 100 kN load cell. For the flexible materials (< 100 MPa), a compressive strain of 5% was applied and a 1 kN load cell was used in order to obtain a more accurate measurement.

<u>Photon irradiation – radiation impact</u>

Irradiation of the samples was done in a clinical photon beam of 6MV, which was calibrated to deliver 0.8 Gy per 100 Monitor Units (MU) at a depth in water of 10cm (Source-to-Surface Distance SSD = 90cm). To each sample positioned at a depth in solid water of 1cm using the same SSD, 10000 MU were delivered, yielding a delivered dose of roughly 100 Gy. This corresponds to a typical target dose of 70 Gy to a HNC boost volume, elevated with a safety factor of around 1.4.

IV.1.4 Radiological properties calculations based on DECT data

DECT-methodologies were used to calculate various radiological properties of the samples. In order to verify the deployed DECT characterization methods, tissue surrogate reference rods (RMI 467 Electron Density Phantom, Gammex, Middleton)

and a Plastic Water (PW – CIRS Inc., Norfolk) rod with a known elemental composition were included in the set of scanned samples. The relative electron density to water $\rho_e \equiv \rho_{e,medium}/\rho_{e,water}$, the effective atomic number Z_{eff} and the proton stopping power ratio to water SPR were calculated from the acquired images.

Reference samples and basic formulae

The composition and the properties of the reference materials are provided in the supplementary material 1 [22]. The relative electron density to water ρ_e of each reference material was determined from its electron density per volume $\rho_{e,medium} = N_A \rho \sum_i w_i Z_i/A_i$, with w_i the mass fraction weight of element i. The effective atomic number was calculated [23,24] as $Z_{eff} = (\sum_i \alpha_i Z_i^m)^{1/m}$, where a value of *3.1* for the exponent m was adopted from Hünemohr et al.[25] as the same scanner spectra were used in this work. The proton Stopping Power Ratio to water SPR was calculated using the simplified [26] Bethe-Bloch formula $SPR = \rho_e \cdot f(\beta c, I_{m,medium}, I_{m,water})$ (equation 1), where βc is the velocity of the proton and I_m is the mean ionization energy [22] of the considered medium. To put the calculations in line with the experiments (see section 2.5.2), a value of 0.347 was taken for β, which corresponds to protons with a kinetic energy of 62MeV.

DECT image acquisition

The reference samples as well as the 3D printed test samples under characterization were scanned with a dual source CT scanner (model Somatom Definition FLASH - Siemens Medical, Forchheim). One sample at a time was inserted in a cavity on the inner circle of a RMI 467 phantom. The dual energy mode applied 80kV$_p$ and 140kV$_p$, the latter with additional Sn filtration to improve spectrum separation. A tube current ratio of 360mAs/148mAs was used. The image reconstruction was done with a clinically used abdomen protocol with a D30f convolution kernel and using a 2mm slice thickness. Scans of the reference samples were taken in single energy mode as well, with a tube voltage of 120kV$_p$. For each volume-of-interest (VOI), the inner 90% of the voxels was used to extract the average number of Hounsfield Units (HU). For the single energy scan, the standard deviation, skewness and kurtosis of the CT-numbers distribution were extracted as well.

Calculation of ρ_e

The extraction of ρ_e from the DECT scans was done using the ΔHU-ρ_e conversion method from Saito [27]. In this procedure, the weighted subtraction of the CT numbers measured at two different energies was introduced, $\Delta HU \equiv (1 + \alpha)\, HU_H - \alpha\, HU_L$, where HU_H and HU_L are, respectively, the CT numbers in HU at the high and low kVp, and α is a scanner-specific weighting factor for the subtraction. A linear function for the calibrated ρ_e^{cal} was then fitted to the dataset of ρ_e and $\Delta HU(\alpha)$ for the reference materials:

$$\rho_e^{cal} = a_1 \frac{\Delta HU(\alpha)}{1000} + a_0 \tag{2}$$

where the final value for the parameter α was optimized to yield the largest coefficient of determination R^2. The found correlation was finally used to calculate the ρ_e for the 3D printed materials with unknown elemental composition from the DECT data.

Calculation of Z_{eff}

Effective atomic numbers were extracted from DECT images using the Tissue Substitute Method (TSM) from Landry *et al* [28]. This method employs the Rutherford parameterization [29] of the linear attenuation coefficients to derive a correlation (3) between Z_{eff} and the ratio of the linear attenuation coefficients measured at the low and high kV_p of the CT scanner, where the fit parameters m, C_{80kVp}, A_{140kVp} and C_{140kVp} are constrained to positive values and where the inversed function can be expressed analytically (4). The theoretical Z_{eff} was calculated as previously described. The TSM then consisted in fitting (3)

to the calculated Z_{eff} and $\mu^{80kVp/140kVp}$ for the reference materials. Equation (4) then enabled to estimate Z_{eff} for the 3D printed materials as well.

$$\frac{\mu_{80kVp}/\mu_{80kVp,water}}{\mu_{140kVp}/\mu_{140kVp,water}} \equiv \mu\Big|_{140kVp}^{80kVp} \approx \frac{1 + C_{80kVp}\, Z_{eff}^{m-1}}{A_{140kVp} + C_{140kVp}\, Z_{eff}^{m-1}}\ , \tag{3}$$

$$Z_{eff} = \left(\frac{1 - \mu\big|_{140kVp}^{80kVp}\, A_{140kVp}}{\mu\big|_{140kVp}^{80kVp}\, C_{140kVp} - C_{80kVp}} \right)^{\frac{1}{m-1}} \tag{4}$$

Calculation of SPR

Equations (2-4) allow to determine the proton SPR of the known reference materials using their elemental composition. For the 3D printed materials however, the

elemental composition is not always known or available. Therefore the formalism presented in the previous sections to calculate ρ_e and Z_{eff} using DECT data was used to estimate their SPR as well. For the missing information, namely I_m, a parameterization[25] through Z_{eff} from 71 tissue surrogate compositions was used as follows: $\ln I_m = a\, Z_{eff} + b$ (equation 5), where the parameter couple (a,b) has a value of (0.125; 3.378) for $Z_{eff} < 8$ and (0.098; 3.376) for $Z_{eff} > 9$. Through the combination of (1) and (5), the SPR can then be approximated by a function of the estimated ρ_e and Z_{eff}:

$$SPR \approx \rho_e \frac{11.73 - (a\, Z_{\text{eff}} + b)}{7.41} \tag{6}$$

IV.1.5 Beam measurements

In order to validate the DECT based calculation of radiological properties, beam measurements were performed on the 3D printed samples. Photon irradiations were performed in order to measure the photon linear attenuation coefficients of the samples. Proton irradiations were performed in order to measure their proton range shift. As a means to estimate the accuracy of the performed measurements, one sample with a known photon attenuation coefficient and proton range shift, namely a block of PW with the same nominal dimensions, was included in the set of irradiated samples.

Photon attenuation measurements

Photon irradiations were performed in clinical photon beams of 6MV and 10MV to measure the photon linear attenuation coefficients of the samples. A narrow beam geometry with a PW mini-phantom as proposed by Georg and Dutreix [30] was used to ensure that the primary beam alone is considered and that the influence of scattered rays from the head and from the attenuating material is excluded as much as possible. The dose rate was measured while inserting samples with different thicknesses in the beam. Fitting the measured data to an exponential curve allowed to determine the spectrum averaged attenuation coefficients μ_{tr}.

Proton range shift measurements

Range shift measurements of the samples were performed at the Cyclotron Resources Center of the Université catholique de Louvain (Louvain-la-Neuve, Belgium), in a 62 MeV non-modulated broad proton beam. A 20mm diameter brass aperture was used

as a final collimator. Radiochromic film (type Gafchromic EBT-XD – Ashland Inc., Covington) was sandwiched between two CIRS PW plates, with the film edge matched to the proximal surface of the plastic plates. The stack was positioned in-line with the beam axis, but with a tilt angle θ of 3° (verified with a digital level) in order to minimize the impact of the difference in proton stopping power between the interfacing media [31]. The distance between the collimator and the PW edge was 15 cm. Bragg peaks were acquired as such (see Figure 1).

To determine the realized range shifts, Bragg peaks were acquired as well with the 3D printed samples inserted between the collimator and the stack. The samples were positioned with the 2cm nominal length sides parallel to the beam axis. The samples were pressed against the stack edge in order to avoid any air gap. To measure the orientation dependency of the range shift due to the discrete 3D printing manufacturing process, irradiations were performed for two orthogonal orientations of the samples.
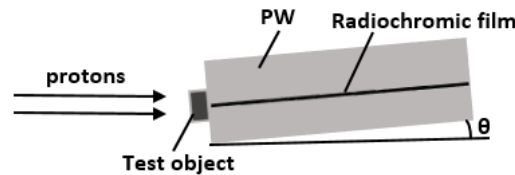
Figure 1. Tilted set up of the radiochromic film sandwiched between PW plates.

RGB 48-bit scans of the irradiated films were acquired using a flatbed scanner (model 10000XL – Epson, Suwa). Pre-calibration of the films using the method developed by Crijns *et al* [32] prior to the proton beam measurements allowed to convert the films scans to dose maps. Three depth dose profiles were extracted from the central region of each broad Bragg peak and averaged out. The true depth dose curve was finally obtained by a $1/\cos\theta$ scaling of the averaged depth dose curve to correct for the 3° tilt of the setup.

The range of each Bragg peak was determined by normalizing the profiles to the maximum dose and by taking the distal 80% position (d_{80}) of the peak [33] relative to the surface/edge of the film. The range shift realized by any of the materials inserted was determined by subtracting the d_{80} with the material inserted from the d_{80} without any material inserted. This measured range shift was compared with the expected range shift as calculated by the DECT estimated SPR:

$$\Delta R_{80,\exp ected} = t_{sample} \frac{SPR_{medium\ to\ water}}{SPR_{PW\ to\ water}}, \tag{7}$$

where t_{sample} represents the measured sample thickness traversed by the protons, $SPR_{medium\ to\ water}$ represents the stopping power ratio to water as estimated before and where $SPR_{PW\ to\ water}$ equals a value of 0.9984 and represents the SPR of PW to water, which compensates for the measurements being performed in PW instead of in real water. In order to quantify the uncertainty on the range shift determination, the aforementioned procedure was performed 6 times for a sample of PW with the same nominal dimensions.

IV.2 Results

IV.2.1 Geometrical printing accuracy

Table 2 provides a summary of the results from the dial gauge measurements performed on the 3D printed samples. TangoPlus, which was the most flexible materials from the set, was the only material with an average thickness value below the lower limit. It exhibited a significant variation of the thickness over the surface as well, which resulted in a visible curvature of the surfaces. VeroWhite, which was made using the same printing technique (PJ) but had a significantly higher stiffness, did not show any out of tolerance dimensions. All measured dimensions, both thickness and length, of the TPU samples were above their upper limit. This resulted in an average deviation in thickness and in length of more than 0.5mm. The other laser sintered materials did not show out of tolerance behaviour, except for one measured length for the PA-12 samples. Tusk, the only material printed by stereolithography, had all length measurements out of tolerance.

IV.2.2 Mechanical response

Table 3 shows the Young's modulus prior and after irradiation as measured in the compression test. Initial Young's moduli as low as 0.6MPa were seen for TangoPlus. VeroWhite, which was also printed with the PJ technique, exhibited a significantly higher stiffness, indicating that significantly different degrees of stiffness could be obtained using the same printing technique . In the group of laser sintered materials the influence of additives such as alumide grains or glass fibres to PolyAmide was

clearly seen, with Young's moduli observed up to 2940MPa. The results suggest that most materials experienced a stiffening effect due to exposure to radiation.

Table 2. Average and standard deviation of the centrally measured thickness, together with the range over which the thickness and length span over the complete surfaces of the different 3D printed samples. The shown tolerances represent the worse of the manufacturer-quoted tolerances. The nominal dimensions are 20x20x80mm³.

Material (Printing technique)	Tolerance [mm]	Thickness				Length	
		Central		Overall		Central	
		Average [mm]	Standard deviation [mm]	Min [mm]	Max [mm]	Min [mm]	Max [mm]
ABS (FDM)	0.2	20.18	0.19	19.99	20.42	79.95	80.00
Tusk (SLA)	0.15	19.88	0.10	19.77	19.98	80.58	80.85
TangoPlus (PJ)	0.2	19.39	0.25	18.8	19.7	78.55	79.85
VeroWhite (PJ)	0.2	20.05	0.08	19.98	20.15	80.02	80.2
PA-12 (SLS)	0.3	20.03	0.06	19.84	20.1	79.95	80.85
PA-Alu (SLS)	0.3	20.12	0.06	20	20.25	80.11	80.35
PA-GF (SLS)	0.3	20.09	0.14	19.94	20.22	80.1	80.28
TPU (SLS)	0.3	20.63	0.16	20.4	20.79	80.58	80.65

Table 3. Young's modulus measured according to ASTM D695 compression test of the 3D printed samples before and after irradiation with 100 Gy. The shown measurement uncertainties depend on the load cell capacity, the Young's modulus and the applied strain.

Material (Printing technique)	Young's modulus				
	Prior to irradiation [MPa]	After irradiation [MPa]	Relative difference [%]	Uncertainty	
				Relative [%]	Absolute [MPa]
ABS (FDM)	629	655	4.1	4	31
Tusk (SLA)	1874	2200	17.4	1.3	25
TangoPlus (PJ)	0.6	0.6	0	3.1	0.03
VeroWhite (PJ)	1981	2450	23.7	1	21
PA-12 (SLS)	1633	1800	10.2	1.5	25
PA-Alu (SLS)	2940	3445	17.2	0.7	21
PA-GF (SLS)	2705	3017	11.5	0.9	25
TPU (SLS)	33	34	3.0	0.9	0.3

Relative electron density ρ_e

For the reference materials, a value of 0.0041 for the standard error of the estimate (S_{est}) was obtained for ρ_e. The maximum relative error was found to be 1% for the lung insert LN-300, while for 8 out of the 12 reference materials, the relative error of the DECT method was below 0.43%. All the relative errors can be found in the supplementary material 2. As the application of the Saito method provided satisfactory results for the prediction of ρ_e, the method was applied as such on the 3D printed samples, for which Figure 2 visualizes the predicted values. Inspection of the Bethe-Bloch equation (1) indicates that the SPR is primarily influenced by ρ_e and only in secondary order by Z_{eff} due to the logarithmic operation on the latter. Therefore the ρ_e estimations already suggest that different materials can be distinguished in terms of proton range shifting, namely the significantly less than water-equivalent ABS, the approximately water-equivalent PA-12 and the at least 9% more than water-equivalent remaining materials. Moreover the impact of the use of additives within the same production technique (e.g. SLS) is clearly visible, as both PA-Alu and PA-GF have an increased ρ_e compared to PA-12. Caution should be exercised when interpreting the found value for ABS, as these samples were produced using a sparse filling pattern. Different values can be obtained when using a filling percentage of 100%.

Effective atomic number Z_{eff}

For the reference materials, a standard error of the estimate S_{est} of 0.1268 was found for Z_{eff}. The largest absolute error for the reference materials was 0.32 for LN-450, while the largest relative error was 4.67% for AP-6. For 9 out of the 12 materials[35] the absolute error was below 0.13 and the relative error below 2.16%.

The calculations for Z_{eff} of the 3D printed samples are shown in Figure 3. Two groups can be distinguished: the majority of the samples with a Z_{eff} equal to or lower than 6.52 and Tusk, PA-Alu and PA-GF with a Z_{eff} between 9.56 and 10.43. The Z_{eff} estimations can be linked to the observed CT numbers: while the one group of materials yields a lower HU_L (80kVp) than the HU_H (Sn, 140kVp), the other group shows the opposite trend. The significantly higher values for HU_L than for HU_H suggest the increased occurrence of the photo-electric effect at diagnostic energies for Tusk, PA-Alu and PA-GF due to the presence of elements with higher Z.

Stopping power ratio to water SPR

For the reference materials, a standard error of the estimate S_{est} of 0.0112 was found for the SPR. The largest relative error of 1.6% occurred for LN-300. For 10 out of the 12 reference materials, the error was smaller than or equal to 1.04%. For the 3D printed samples (see Figure 2), the different behaviours relative to water as already observed in the calculation of ρ_e are confirmed.
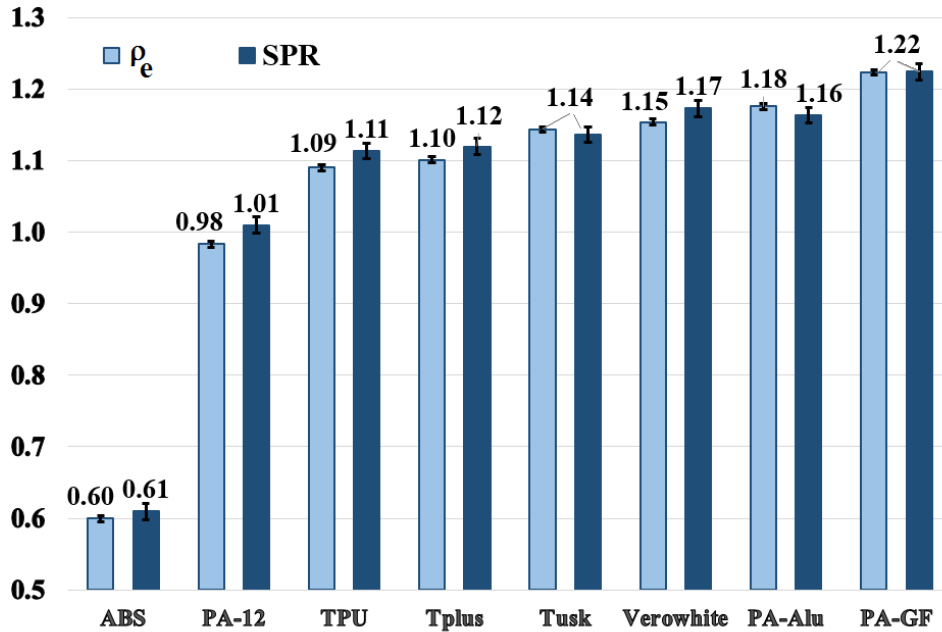
Figure 2. Calculated ρ_e and SPR ($\pm$ 1 S_{est}) for the 3D printed materials using the Saito method.
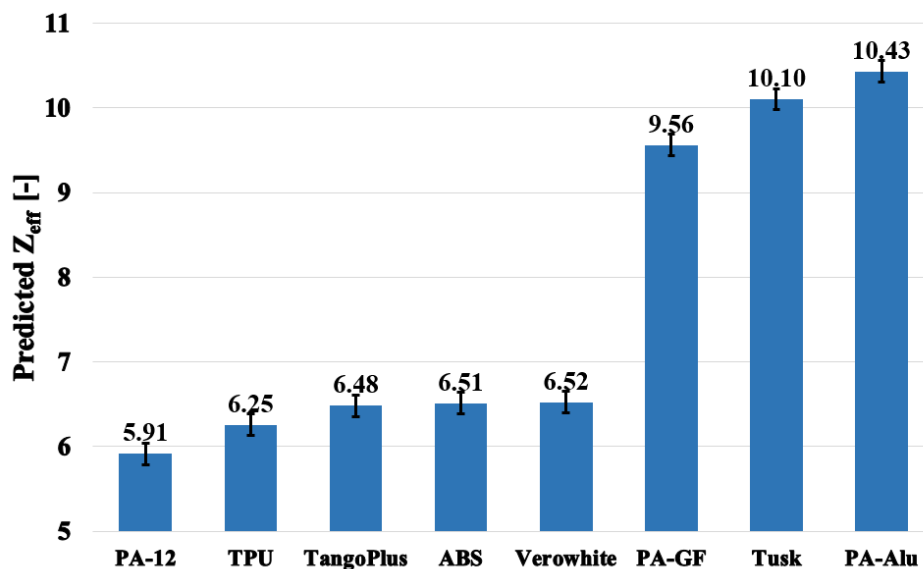
Figure 3. Calculated Z_{eff} ($\pm$ 1 S_{est}) for the 3D printed samples using the Landry method.

IV.2.3 Beam measurements

Photon linear attenuation coefficient μ_{tr}

The attenuation coefficients μ_{tr} measured at the two energies are displayed in table 4. No directional dependency was observed. For the measured μ_{tr} versus the predicted ρ_e a linear relationship (R²>0.95) was found, as documented in the supplementary material 3.

Table 4. Measured linear attenuation coefficients at two photon energies for the 3D printed samples and for PW.

	μ_{tr} [cm⁻¹]		μ_{tr} [% of PW]	
Material	6MV	10MV	6MV	10MV
ABS	0.0297	0.0227	62.2	62.5
Tusk	0.0538	0.0409	112.6	112.7
TangoPlus	0.0517	0.0396	108.1	109.0
VeroWhite	0.0546	0.0416	114.2	114.5
PA-12	0.0472	0.0351	98.8	96.7
PA-Alu	0.0598	0.0463	125.1	127.6
PA-GF	0.0572	0.0446	119.7	122.9
TPU	0.0521	0.0397	109.1	109.4
PW	0.0478	0.0363	100.0	100.0

Proton range shift

Figure 4 displays a selection of the acquired Bragg peaks, with and without 3D printed material inserted. Repeated application of the measurement method on the PW insert with known composition yielded deviations from the theoretical range shift of +/- 0.25 mm. Figure 5(a) shows the error on the DECT calculated range shift for the 3D printed samples. For one sample material, Tusk, the range shift calculation differs more than 1mm from the measured range shift. For 7 out of 8 materials, the deviation is no more than 0.66 mm. In Figure 5(b) the difference in measured range shift for the two measured orientations of the samples is shown. For 3 of the sample materials (ABS, VeroWhite and PA-12) the range shift difference between two orientations was observed to be above 0.5 mm, which was the maximum difference between the repeated measurements on the PW sample. This suggests the existence of an orientation dependency for range shifting for these materials.
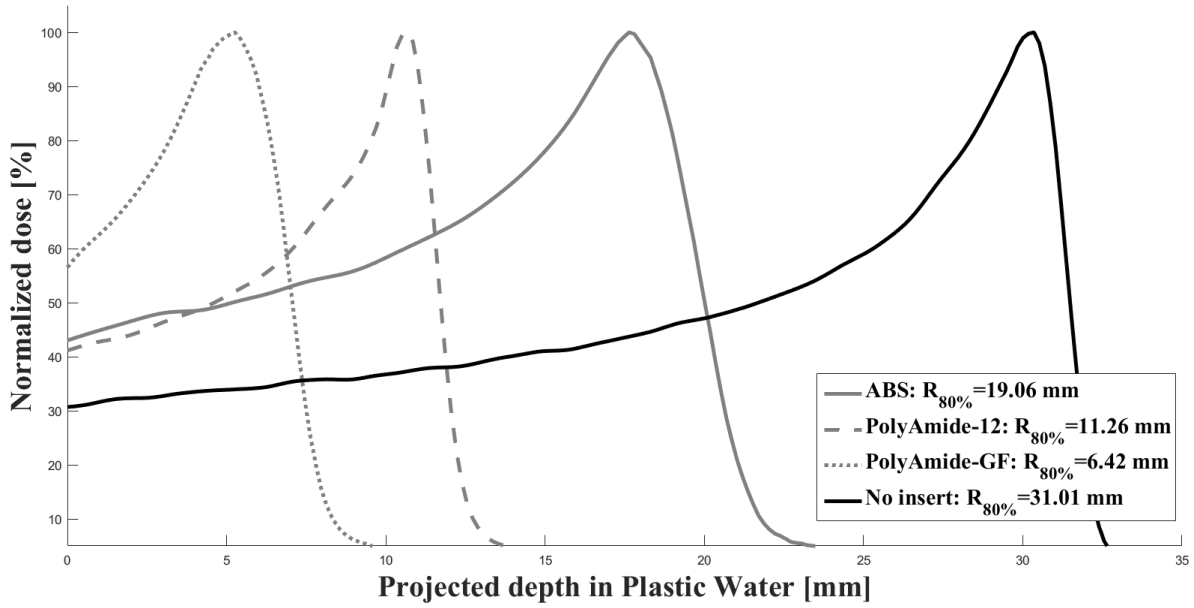
Figure 4. Selection of acquired Bragg peaks with and without 3D printed material inserted.
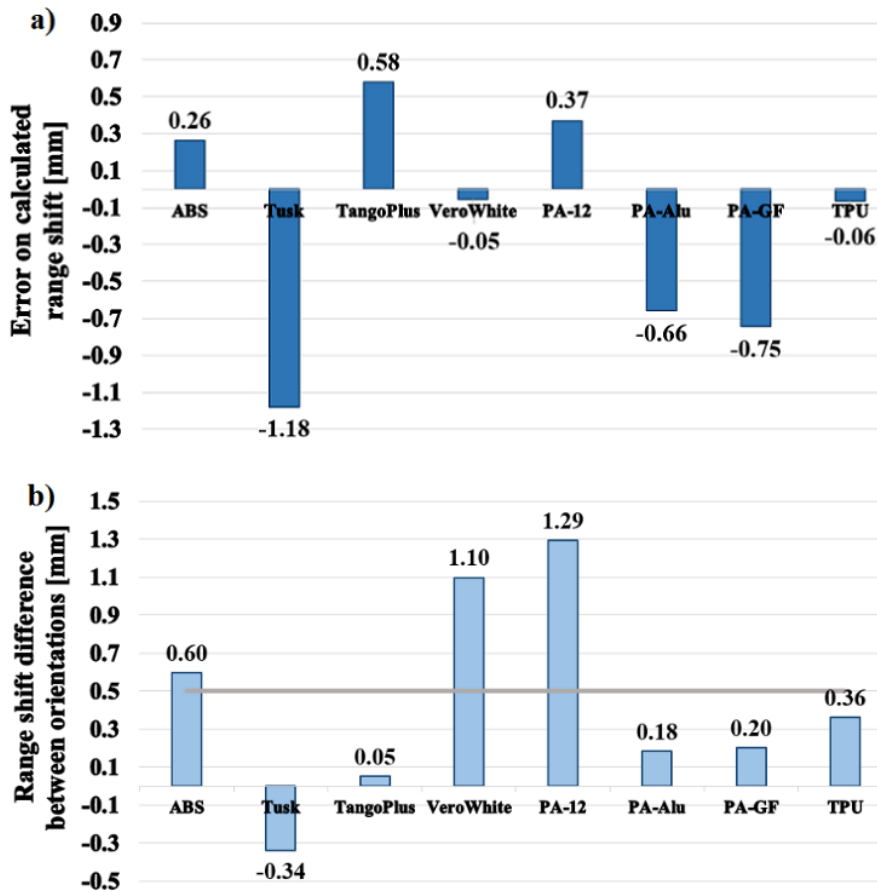
Figure 5. a) Error on the calculated range shift for one orientation and **b)** measured range shift difference between two orientations.

IV.3 Discussion

The first goal of this study was to perform a broad characterization of 3D printed materials for the future construction of a novel, multifunctional immobilization structure. The resulting data can be used for an optimal design of such a device in terms of structural strength, elasticity and geometrical and radiological properties. The wide range of Young's moduli encountered in the compression tests, from the rubber-like flexibility of TangoPlus to the polystyrene-like rigidity of Tusk and PA, makes a set of materials available to fulfil specific mechanical functionalities. The feature of high elasticity of these former materials for instance could be used advantageously to increase comfort in regions of elevated contact pressure. Such flexibility might also be an advantage to maintain a close fit for some parts of the immobilization in a situation with small anatomical changes. On the other hand, for regions requiring a tight tolerance on the positioning accuracy, a more rigid material should be used rather than a flexible material. For the case of a uniform load q on a beam supported at both ends, with a Young's modulus E, a length L and a square section with side a, the maximum deformation can be calculated as $\delta = \frac{5q}{32E} \left(\frac{L}{a}\right)^4$. This simplified calculation can be applied to the structural support of a head by a beam in for example 3D printed ABS with the same dimensions as the test samples. As such, a realistic but overestimated load of 10 kg of a patient head would result in an deformation below 0.1 mm, which is clearly acceptable. Obviously, such simplified calculations can be only indicative for the conception of a design. Also, the stiffness measurements were performed on standardized, simple shapes. As the design of the printed immobilization device proceeds, a necessary next step would be to assess the mechanical integrity and the deformations of more complex structures by means of experiments and/or in-silico finite element method (FEM) analysis.

Besides the mentioned mechanical stiffness and deformation itself, the change in mechanical response due to the administration of clinically relevant dose levels of 70 Gy (multiplied with a safety factor of around 1.4) is a point of consideration as well. In this regard, the performed compression tests prior and after irradiation provide valuable information. In general, the results suggest that most of the tested materials experience a stiffening effect due to the exposure to radiation. This may be explained by a facilitation of the chain forming due to the irradiation, which could result in an increased polymerization hence stiffening of the materials. Depending on the type of

polymer and the printing process used, the susceptibility to this effect indeed may differ from one material to another. A side effect of this stiffening could be that the material becomes more brittle, meaning less deformation can be sustained before breaking and material rupture occurs more abruptly. These results however may be less pronounced when using clinical dose levels without the multiplication factor. Also, as only the influence of photon irradiation on the mechanical stiffness was assessed, it might be valuable to repeat this exercise for proton irradiation, since the interaction of protons with matter yields additional processes such as nuclear interactions which might cause additional effects to occur.

The measured interaction of both photons and protons with the 3D printed materials allows to assess their beam modifying properties when used in an immobilization structure. The three observed degrees of water-equivalence for both types of interaction can namely be deliberately exploited in the design. For instance, ABS may be used for parts where minimal beam interaction is desired, such as support structures, whereas the near water-equivalent PA-12 may be used for parts where the radiological behaviour of soft tissue is to be mimicked. The elevated beam interaction of the remaining materials, in various degrees compared to water, may be selected for regions where a maximum proximal dose shift for the same thickness of material is aimed for, for example bolus. Given the extensiveness of this latter group of materials, additional material properties may be included in the selection process for bolus material, depending on the design requirements to be met such as the mechanical stiffness, the cost per unit of volume or the DECT estimated Z_{eff} to minimize the amount of scattering. However the use of the most flexible materials in zones where a beam portal is assigned should be done with caution, given the poor agreement of the sample dimensions with the nominal dimensions and given the high degrees of curvature observed. The uncertainty on the thickness hence on the water-equivalent path length may result in dose delivery deviations from the planned dose. The reported printing inaccuracy however might be overcome by optimizing the used print direction. Moreover the testing of a larger amount of samples might reveal better dimensional compliance for these materials.

The DECT based calculations of the radiological properties offer a first step towards the clinical implementation of in-house assessment of 3D printed materials for the

proposed use in immobilization, which was the second goal of this study. Such an approach could offer possibilities to reduce the number of device-specific quality assurance (QA) tests needed before clinical use. The calculated ρ_e was (albeit indirectly) experimentally verified and appears to serve as an excellent predictor for the photon attenuation. Indeed, the governing relationships for the atomic mass cross section σ_{at} respectively electronic cross section σ_{el} for the Compton effect can be written [34] as:

$$\begin{cases} \dfrac{\sigma_{at}}{\rho} = \dfrac{N_A\, Z}{A}\, \sigma_{el} \rightarrow \sigma_{at} = \rho_e\, \sigma_{el} \\ \sigma_{el} \propto Z^0 \end{cases} \Rightarrow \sigma_{at} \propto \rho_e \qquad (8)$$

Since at clinical MV photon energies the Compton effect dominates and σ_{at} scales linearly with ρ_e, the observed linear variation of μ_{tr} with ρ_e is as expected.

The found uncertainty of ±0.25mm on the used range shift measurement method is in line with the findings of Zhao and Das [31]. Given this uncertainty, in general the DECT derived SPR provides a good estimation for the range shifting of 3D printed materials. The systematically larger deviations for the higher Z_{eff} materials however might indicate that the used parameterization $I=f(Z_{eff})$ which is used in the SPR estimation can be improved for this group of materials. This explanation seems viable since the used parameterization was derived from a large set of tissue-equivalent materials, whereas the 3D printed materials that yield the larger deviations do not belong to this group since they contain elements such as Si and Al.

Additionally, the SPR estimation method does not allow to take into account the sample orientation dependency of the achieved range shift as observed for certain printed materials. The CT-numbers distribution however might hint at the presence of this effect, as some correlation was observed between the orientation dependency and the CT-numbers distribution of the ABS and VeroWhite samples, as these exhibited a relatively high skewness and kurtosis (see supplementary material 2). Since the necessarily used tilt in the measurement setup might already have dampened or even concealed this orientation dependency, this effect might even be more pronounced when proton beam incidences perfectly parallel or orthogonal to the printed layers are used. An altered measurement set up using a Bragg peak ionization chamber to

longitudinally scan the range shifted beam incidence in a water tank could provide more information on this effect, as this set up enables to measure the residual range under perfectly aligned beam incidence and with a better accuracy. In any case, the orientation dependency should be carefully considered when selecting and validating 3D printed materials for the intended multifunctional immobilization device.

In conclusion, 3D printing technology opens new possibilities to design immobilization devices, which could include multiple functionalities beyond fixation only. Today, however, little is known about the relevant properties for this application. Due to the additive manufacturing process, 3D printed materials cannot be considered to exhibit the same behaviour as their traditionally manufactured counterparts, which is for instance illustrated by the observed orientation dependency of the range shift for certain printed materials. In this study, the first step towards 3D printed, multifunctional immobilization was performed, by going through a candidate clinical workflow for the first time: from the material printing to DECT characterization with a verification through beam measurements. Besides a proof of concept for beam modification, the mechanical response of printed materials was also investigated to assess their capabilities for positioning functionality. For the studied set of printed materials and techniques, a wide variety of mechanical and radiological properties can be selected from for the intended purpose. Moreover the elaborated hybrid DECT methods aid in performing in-house QA of 3D printed components, as these methods enable the estimation of the radiological properties relevant for use in radiation therapy.

Acknowledgments

References

[1]   Lomax AJ. Intensity modulated proton therapy and its sensitivity to treatment uncertainties 1: the potential effects of calculational uncertainties. Phys Med Biol 2008;53:1027–42.

[2]   Lomax AJ. Intensity modulated proton therapy and its sensitivity to treatment uncertainties 2: the potential effects of inter-fraction and inter-field motions. Phys Med Biol 2008;53:1043–56.

[3]   Palta JR, Yeung DK. Proton Therapy Physics. In: Paganetti H, editor., CRC, Boca Raton; 2011, p. 413–34.

[4]   Engelsman M, Schwarz M, Dong L. Physics Controversies in Proton Therapy. Semin Radiat Oncol 2013;23:88–96.

[5]   Langendijk JA, Lambin P, De Ruysscher D, Widder J, Bos M, Verheij M. Selection of patients for radiotherapy with protons aiming at reduction of side effects: The model-based approach. Radiother Oncol 2013;107:267–73.

[6]   Ramaekers BLT, Grutters JPC, Pijls-Johannesma M, Lambin P, Joore MA, Langendijk JA. Protons in head-and-neck cancer: Bridging the gap of evidence. Int J Radiat Oncol Biol Phys 2013;85:1282–8.

[7]   Melchels FPW, Feijen J, Grijpma DW. A review on stereolithography and its applications in biomedical engineering. Biomaterials 2010;31:6121–30.

[8]   Matsumoto JS, Morris JM, Foley TA, Williamson EE, Leng S, McGee KP, et al. Three-dimensional Physical Modeling: Applications and Experience at Mayo Clinic. Radiographics 2015;35:1989–2006.

[9]   Ju SG, Kim MK, Hong CS, Kim JS, Han Y, Choi DH, et al. New technique for developing a proton range compensator with use of a 3-dimensional printer. Int J Radiat Oncol Biol

Phys 2014;88:453−8.

[10]   Lindsay C, Kumlin J, Jirasek A, Lee R, Martinez DM, Schaffer P, et al. 3D printed plastics for beam modulation in proton therapy. Phys Med Biol 2015;60:N231−40.

[11]   Zou W, Fisher T, Zhang M, Kim L, Chen T, Narra V, et al. Potential of 3D printing technologies for fabrication of electron bolus and proton compensators. J Appl Clin Med Phys 2015;16:90−8.

[12]   Mayer R, Liacouras P, Thomas A, Kang M, Lin L, Simone CB. 3D printer generated thorax phantom with mobile tumor for radiation dosimetry. Rev Sci Instrum 2015;86:074301.

[13]   Ahn PH, Ahn AI, Lee CJ, Shen J, Miller E, Lukaj A, et al. Random Positional Variation Among the Skull, Mandible, and Cervical Spine With Treatment Progression During Head-and-Neck Radiotherapy. Int J Radiat Oncol Biol Phys 2009;73:626−33.

[14]   Zhang L, Garden AS, Lo J, Ang KK, Ahamad A, Morrison WH, et al. Multiple regions-of-interest analysis of setup uncertainties for head-and-neck cancer radiotherapy. Int J Radiat Oncol Biol Phys 2006;64:1559−69.

[15]   Barker JL, Garden AS, Ang KK, O'Daniel JC, Wang H, Court LE, et al. Quantification of volumetric and geometric changes occurring during fractionated radiotherapy for head-and-neck cancer using an integrated CT/linear accelerator system. Int J Radiat Oncol Biol Phys 2004;59:960−70.

[16]   Barten DLJ, Tol JP, Dahele M, Slotman BJ, Verbakel WFAR. Comparison of organ-at-risk sparing and plan robustness for spot-scanning proton therapy and volumetric modulated arc photon therapy in head-and-neck cancer. Med Phys 2015;42:6589−98.

[17]   Safai S, Bortfeld T, Engelsman M. Comparison between the lateral penumbra of a collimated double-scattered beam and uncollimated scanning beam in proton radiotherapy. Phys Med Biol 2008;53:1729−50.

[18]   Sisterson JM, Urie MM, Koehler a M, Goitein M. Distal penetration of proton beams: the effects of air gaps between compensating bolus and patient. Phys Med Biol 1989;34:1309−15.

[19]   Titt U, Mirkovic D, Sawakuchi GO, Perles LA, Newhauser WD, Taddei PJ, et al. Adjustment of the lateral and longitudinal size of scanned proton beam spots using a pre-absorber to optimize penumbrae and delivery efficiency. Phys Med Biol 2010;55:7097−106.

[20]   Materialise NV, 3D printed material properties, 2015, http://manufacturing.materialise.com/sites/default/files/public/AMS/Datasheets/ams_datasheets_a gust2015.pdf. 2015.

[21]   American Society for Testing and Materials. Standard test method for compressive properties of rigid plastics. Rep. D695-15, ASTM, West Conshohocken; 2015.

[22] Johns HE, Cunningham JR. The Physics of Radiology. Charles C. Thomas, Springfield, IL; 1983.

[23] ICRU Report 49. ICRU report. Oxford University Press; 2007.

[24] Seltzer SM, Berger MJ. Evaluation of the collision stopping power of elements and compounds for electrons and positrons. Int J Appl Radiat Isot 1982;33:1189–218.

[25] Hünemohr N, Krauss B, Tremmel C, Ackermann B, Jäkel O, Greilich S. Experimental verification of ion stopping power prediction from dual energy CT data in tissue surrogates. Phys Med Biol 2014;59:83–96.

[26] Schneider U, Pedroni E, Lomax a. The calibration of CT Hounsfield units for radiotherapy treatment planning. Phys Med Biol 1996;41:111–24.

[27] Saito M. Potential of dual-energy subtraction for converting CT numbers to electron density based on a single linear relationship. Med Phys 2012;39:2021.

[28] Landry G, Seco J, Gaudreault M, Verhaegen F. Deriving effective atomic numbers from DECT based on a parameterization of the ratio of high and low linear attenuation coefficients. Phys Med Biol 2013;58:6851–66.

[29] Rutherford RA, Pullan BR, Isherwood I. Measurement of effective atomic number and electron density using an EMI scanner. Neuroradiology 1976;11:15–21.

[30] Georg D, Dutreix A. Methods for beam data acquisition offered by a mini-phantom. Phys Med Biol Phys Med Biol 1999;44:817–817.

[31] Zhao L, Das IJ. Gafchromic EBT film dosimetry in proton beams. Phys Med Biol 2010;55:N291–301.

[32] Crijns W, Maes F, Heide UA Van Der, Heuvel F Van Den. Calibrating page sized Gafchromic EBT3 films. Med Phys 2013;40:012102.

[33] Gottschalk B. Proton Therapy Physics. In: Paganetti H, editor., CRC, Boca; 2011, p. 32.

[34] Attix FH. Introduction to radiological physics and radiation dosimetry. Wiley-VCH, Weinheim; 1986.

Supplementary material 1. Elemental weight fractions w_i (%) of the Gammex RMI 467 inserts and of CIRS Plastic Water Original as provided by the manufacturers. The mass density r of the Gammex inserts was provided batch-specific. The mean ionization energy I_m of each composition was calculated using Bragg's additivity rule [23], where the ionization energy I_i of the elements was taken from Seltzer and Berger [24]. For water an I_m value of 75 eV was adopted [23]. The remaining properties were calculated using the equations described in section 2.4.1.

Element	H	C	N	O	Mg	Si	P	Cl	Ca	ρ (g cm^{-3})	ρ_e (-)	Z_{eff} (-)	I (eV)	SPR (-)
Z	1	6	7	8	12	14	15	17	20					
A	1.008	12.011	14.01	15.99	24.31	28.085	31	35.45	40.08					
Lung (LN-300)	8.46	59.38	1.96	18.14	11.19	0.78	0	0.1	0	0.28	0.27	7.49	73.91	0.27
Lung (LN-450)	8.47	59.57	1.97	18.11	11.21	0.58	0	0.1	0	0.4	0.39	7.46	73.78	0.39
Adipose (AP6)	9.06	72.3	2.25	16.27	0	0	0	0.13	0	0.94	0.92	6.17	66.56	0.94
Breast	8.59	70.11	2.33	17.9	0	0	0	0.13	0.95	0.98	0.95	6.81	68.19	0.97
Solid Water	8.02	67.23	2.41	19.91	0	0	0	0.14	2.31	1.02	0.99	7.54	70.41	1.00
Brain	10.83	72.54	1.69	14.86	0	0	0	0.08	0	1.05	1.05	6.05	63.54	1.07
Liver (LV1)	8.06	67.01	2.47	20.01	0	0	0	0.14	2.31	1.10	1.07	7.55	70.33	1.07
Inner bone	6.67	55.64	1.96	23.52	0	0	3.23	0.11	8.86	1.14	1.09	10.14	80.10	1.09
Bone (B200)	6.65	55.52	1.98	23.64	0	0	3.24	0.11	8.87	1.15	1.11	10.15	80.18	1.10
Bone (CB2-30)	6.68	53.48	2.12	25.61	0	0	0	0.11	12.01	1.34	1.28	10.61	80.75	1.27
Bone (CB2-50)	4.77	41.63	1.52	32	0	0	0	0.08	20.02	1.6	1.47	12.26	93.17	1.43
Cortical Bone (SB-3)	3.41	31.41	1.84	36.5	0	0	0	0.04	26.81	1.83	1.70	13.38	104.55	1.62
Plastic Water Original	7.79	59.82	1.78	23.57	0	0	0	0.23	6.76	1.03	1.00	9.22	74.43	1.00

Supplementary material 2. Hounsfield Units (HU) and standardized moments of the CT acquisitions for both the reference materials and the 3D printed materials. An overview of the DE-CT based estimated radiological properties is given as well.

Reference material	CT acquisition					ρ_e		Z_{eff}		SPR_w	
	HU_{mean} (80 kVp)	HU_{mean} (140 kVp, Sn)	σ (120 kVp)	Skewness (120 kVp)	Kurtosis (120 kVp)	Predicted value [-]	Relative error [%]	Predicted value [-]	Relative error [%]	Predicted value [-]	Relative error [%]
LN-300	-720	-723	31	-	-	0.27	-1.00	7.77	3.78	0.27	-1.60
LN-450	-595	-600	30	-	-	0.39	0.79	7.77	4.22	0.39	0.15
Adipose AP6	-116	-82	4	-	-	0.93	0.36	5.90	-4.67	0.94	1.45
Breast	-62	-44	4	-	-	0.96	0.43	6.79	-0.21	0.97	0.36
Solid Water	5	-1	4	-	-	0.99	0.16	7.63	1.07	1.00	-0.86
Brain	0	33	4	-	-	1.04	-0.67	6.18	2.16	1.07	-0.66
Liver	80	74	5	-	-	1.07	0.08	7.59	0.58	1.07	-0.89
Inner Bone	299	161	5	-	-	1.09	-0.03	10.06	-0.82	1.09	0.26
Bone B200	314	175	5	-	-	1.11	0.19	10.06	-0.84	1.10	0.48
CB2-30	592	374	6	-	-	1.27	-0.57	10.72	1.07	1.27	-1.04
CB2-50	1094	664	11	-	-	1.47	-0.06	12.27	0.12	1.43	-0.68
SB3 Cortical	1653	996	18	-	-	1.70	0.21	13.37	-0.10	1.62	-0.30
PW	128	42	5	-0.17	0.21	1.00	0.13	9.4	1.98	1.00	0.28
ABS	-416	-401	16	0.83	-0.92	0.60	-	6.51	-	0.61	-
Tusk	361	214	8	0.16	0.15	1.14	-	10.10	-	1.14	-
TangoPlus	67	94	5	0.03	0.27	1.10	-	6.48	-	1.12	-
Verowhite	119	147	5	1.40	0.94	1.15	-	6.52	-	1.17	-
PA-12	-62	-26	4	0.01	-0.19	0.98	-	5.91	-	1.01	-
PA-Alu	437	260	23	-0.15	-0.37	1.18	-	10.43	-	1.16	-
PA-GF	396	280	12	-0.08	-0.29	1.22	-	9.56	-	1.22	-
TPU	49	82	5	0.10	0.01	1.09	-	6.25	-	1.11	-

Supplementary material 3. Measured μ_{tr} versus calculated ρ_e for the 3D printed samples and for PW.
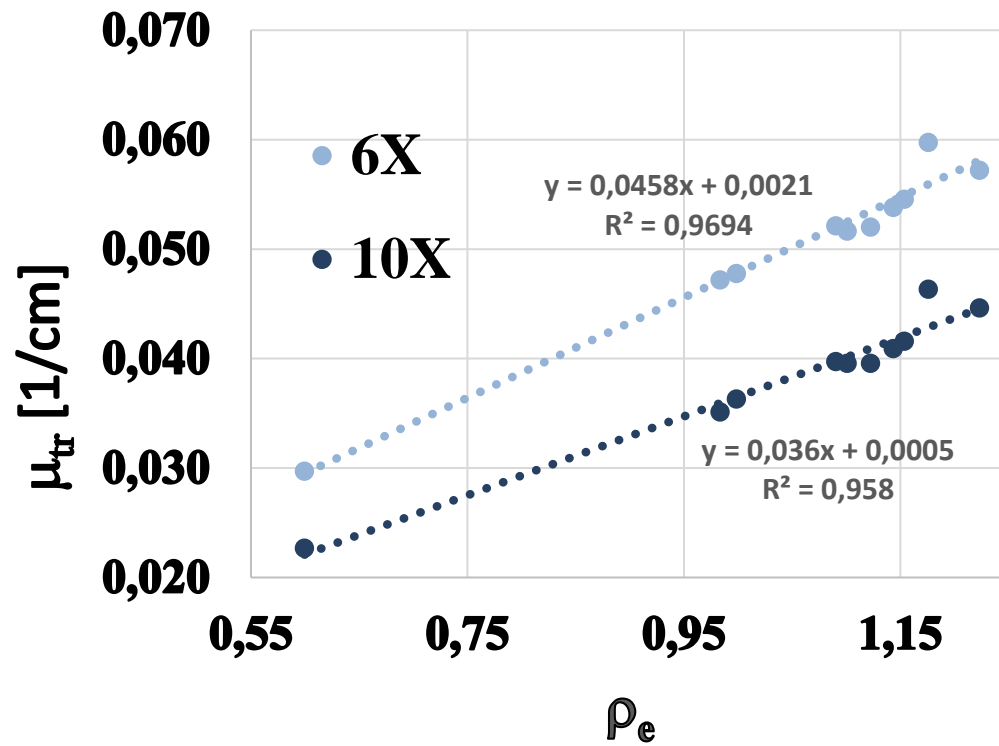
3D printed immobilization for radiotherapy of head-and-neck cancer: A pilot study on patients

V

Abstract

Background & purpose

Due to the large flexibility in object shaping, 3D printing could enhance patient immobilization in head & neck cancer (HNC) radiotherapy (RT). In intensity-modulated proton therapy (IMPT), for instance, 3D printed immobilization (3DPrIm) may allow the integration of range shifter (RS) with minimal air gap, hereby reducing spot size and hardware collision risk compared with nozzle-mounted RS. In addition, the potentially improved patient-specific approximation of the body outline with 3DPrIm may reduce inter-fractional setup variations compared with thermoplastic masks (TM). 3DPrIm, however, cannot be created in the physical presence of the patient and thus requires a new RT workflow. In addition, tolerability and comfort cannot be assumed, given the novelty of the proposed 3DPrIm device. In this pilot study, the feasibility of 3DPrIm was evaluated on patients with HNC in terms of workflow, patient comfort and setup accuracy. Being the first application on actual patients, the study focused on 3DPrIm of the head region.

Methods and Materials

3D PrIm was achieved for three HNC patients and was compared with the clinically used TM (5-points, closed face, generic headrest) using repeated CBCT on a linac. For the creation of the 3DPrIm, an additional planning CT was acquired of the patients immobilized without a TM. The segmented pristine body contour was used to design a closed posterior shell with cranial back-stop and an anterior shell with open face. Five weekly study CBCTs (3DPrIm) and clinical CBCTs (TM) of the same day were rigidly registered with the respective planning CT, based on a global, composite ROI consisting of the occiput and mandible. Residual local setup errors were determined for five sub-ROIs (occiput, mandible, C2, C6 and larynx) by subsequent rigid registration based on each individual sub-ROI and quantification of the difference relative to the global registration. At the end of the RT course, the patients and RTTs completed a questionnaire polling their experience in terms of comfort and immobilization usability.

Results

Based on the 3D-errors at population level and on the 1D error components (group mean error M and systematic error Σ), 3DPrIm achieved a setup accuracy of the occiput and mandible which appeared to be at least comparable with TM. 3DPrIm setup accuracy was reduced for the more caudally located sub-ROI's (C6 & larynx), as the current absence of lower neck immobilization resulted in considerably larger group mean errors than with TM. All patients and RTTs evaluated the 3DPrIm as usable and patient-friendly.

Conclusions

3DPrIm is feasible in terms of workflow, is tolerable by HNC patients and can achieve clinically acceptable setup accuracy for the head region. 3DPrIm therefore is a valid option to pursue enhancements in RT of HNC, such as spot-size reducing bolus in IMPT. Further optimization of the initial design, however, with added lower neck immobilization, is required towards clinical use of 3DPrIm in RT of HNC.

HEAD-AND-NECK CANCER (HNC) REQUIRES A MULTIDISCIPLINARY approach with most patients undergoing radiation therapy (RT) as an integral part of a treatment with curative intent [1]. RT of HNC, however, is often challenging due to the large, complex-shaped target volumes in close proximity to a large number of organs-at-risk (OAR). While the introduction of intensity-modulated radiotherapy using photon beams has led to reduced normal tissue irradiation, the occurrence of normal tissue complications remains frequent, with significant impact on patients' quality of life [1,2]. In this regard, the use of protons is highly promising due to their advantageous depth dose profile compared to photons. The finite range and the sharp fall-off of the dose deposition in the Bragg peak enable potentially improved sparing of normal tissues, which is expected to result in reduced normal tissue complications [3,4].

The highly conformal dose distribution of intensity-modulated proton therapy (IMPT) is associated with considerable sensitivity of the target dose coverage to patient setup uncertainties [5]. To minimize such daily setup variations in IMPT of HNC, patient positioning is typically performed using a thermoplastic mask (TM), molded around the patient's body outline during treatment simulation. Alternative patient immobilization using 3D printing, however, could offer a number of advantages compared with TMs. Specifically, 3D printed patient immobilization (3DPrIm) may allow for the integration of bolus, a range shifter (RS) technique for which clinically relevant toxicity reductions compared with conventional nozzle-mounted RS have been theoretically shown for IMPT of HNC [6]. Such integrated device also would ensure presence and correct placement of the RS for each treatment field and may simplify the overall IMPT delivery workflow by reducing the number of hardware manipulations – with collision risk – compared with nozzle-mounted RS. Added to that, a 3DPrIm may achieve a potentially improved patient-specific approximation of the body outline, which could reduce inter-fractional setup variations compared with TMs.

The proposed method of 3DPrIm, however, differs greatly from the widely adopted method using TMs. Unlike TMs, namely, a 3DPrIm cannot be created in the physical presence of the patient and thus requires a new RT workflow using any captured information on the patient's external anatomy. Moreover, tolerability and comfort

cannot be assumed, given that to date 3DPrIm of patients with HNC has not yet been reported. Moreover, any improvement in setup reproducibility with 3DPrIm remains to be shown. In this work, a pilot study of 3DPrIm on patients with HNC was performed. The aim of the study was to show the feasibility of 3DPrIm in terms of workflow and patient comfort and to quantify the obtained setup reproducibility. The clinically used immobilization technique, with a TM and a standard headrest, hereby served as a reference for comparison. Being the first application on actual patients, this pilot study focused on 3DPrIm of the head region.

V.1 Materials and methods

V.1.1 Study patients & study activities

Local ethics committee approval was obtained for a study to evaluate feasibility of 3DPrIm on patients with HNC receiving RT at the authors' institute. The study activities consisted of the acquisition of an additional planning CT for the design of a 3DPrIm, weekly cone-beam computed tomography (CBCT) imaging of the study patients immobilized with the 3DPrIm and completion of a questionnaire by the study patients and radiation therapy technologists (RTT). Three patients were included based on willingness to participate, Karnofsky performance status at least 70% and age at least 18 years old, after which written informed consent was obtained. The patient characteristics are given in Table 1.

Table 1. Characteristics of the included study patients.

	Patient A	Patient B	Patient C
Gender	Male	Male	Male
Age [years old]	62	62	66
Height [cm]	176	185	170
Weight [kg]	63.5	70	84
Tumor site	Floor of mouth	Tongue	Supraglottic larynx
TNM [8th ed. UICC]	pT2N1M0	pT3N0M0	cT3N0M0
RT type	Postop. RT	Postop. RT	Definitive chemo-RT
Dose prescription	60Gy/2Gy	60Gy/2Gy	70Gy/2Gy + 54.25Gy/1.55Gy

Abbreviations: UICC = International Union Against Cancer; Postop. = postoperative; RT = radiotherapy.

V.1.2   3D printed immobilization

<u>Study planning CT acquisition</u>

To obtain a pristine body contour for the design of the 3DPrIm, an additional planning CT – or study planning CT – was acquired of each patient immobilized without a TM. To this end, the patient was positioned as visualized in Figure 1, i.e. in supination on a treatment couch overlay that forms part of a commercially available stereotactic RT head immobilization dual-mask system (BrainLAB AG, Feldkirchen, Germany) [7]. A foam mattress (Orfit Industries, Wijnegem, Belgium) and a soft travel pillow were used as body support and headrest, respectively. A hook-and-loop fastener and inflatable cushions (Type Multipad Slim, Pearl Technology AG, Schlieren, Switzerland) were used to immobilize the chin and the temporal bones, respectively. These immobilization items were held in place with 3D printed adapter pieces, attached to the lateral sides of the treatment couch overlay with plastic clamps. A localization point was defined close to the temporal bones, to be marked on the anterior part of the 3DPrIm during the design stage. CT imaging was performed on a SOMATOM Definition EDGE scanner (Siemens Healthineers, Forchheim, Germany), in single-energy mode at 120 kVp, using 1mm slice thickness and a HR38 convolution kernel for reconstruction.
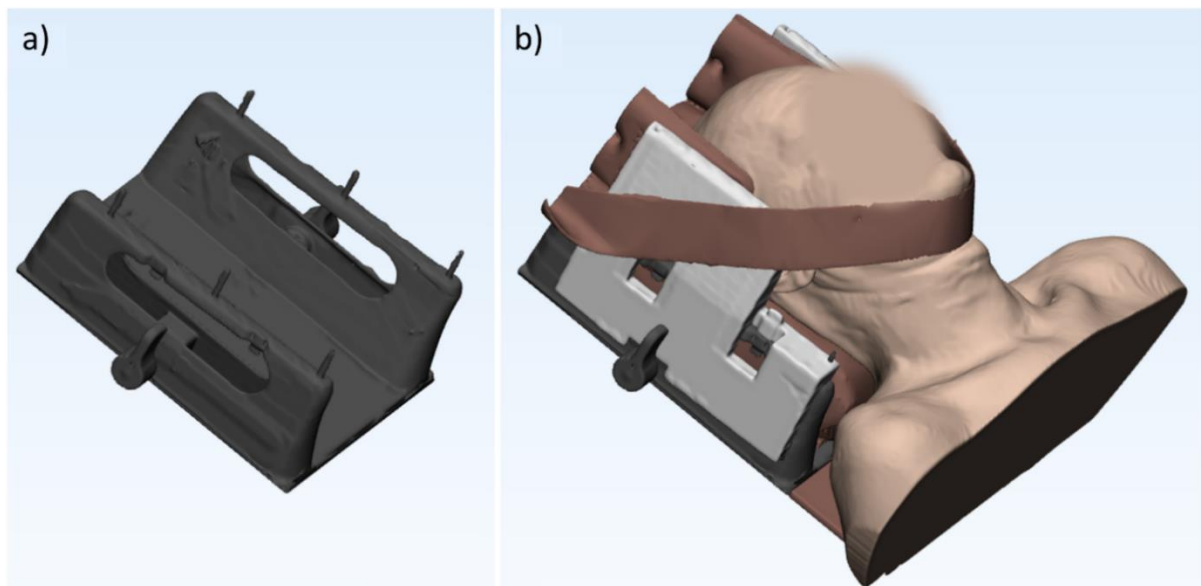
Figure 1. Patient position during acquisition of the study planning CT scan to obtain the body contour. The patient was positioned in supination on a treatment couch overlay **(a)** (visualized in dark grey), which forms part of a commercially available stereotactic RT head immobilization mask system. A foam mattress and a soft travel pillow were used as body support and headrest, respectively (visualized in brown) **(b).**

A hook-and-loop fastener and inflatable cushions were used to immobilize the chin and the temporal bones, respectively (visualized in brown). These immobilization items were held in place with 3D printed adapter pieces, attached to the lateral sides of the treatment couch overlay (visualized in light grey). Patient-specific characteristics have been censored for reasons of privacy.

Body contour segmentation

The patient's body contour was determined with image thresholding of the study planning CT in 3D Slicer (version 4.10.1, [8]), using a threshold range of [-300 HU; 3071 HU]. The lower threshold value was experimentally determined by creating several 3DPrIm assemblies for an anthropomorphic head phantom (Proton Therapy Dosimetry Head, Model 731-HN, CIRS, Norfolk, VA). Each 3DPrIm assembly was based on a different lower threshold value, incremented in steps of 50 HU starting from -350 HU, the threshold value used by the body segmentation functionality in commercially available software (Eclipse v.15.6, Varian Medical Systems, Palo Alto, CA and MIM v.6.6, MIM Software Inc., Cleveland, OH). The threshold value of -300 HU was finally retained, as this was the largest value that generated an immobilization assembly that could still be physically fit to the phantom.

Design of the 3D printed immobilization

A 3D printable immobilization assembly was designed to fit the patient's body contour using the software 3-matic (research version 13.0, Materialise NV, Leuven, Belgium). The detailed steps of the design process are shown in supplementary material 1. Figure 2 visualizes the 3DPrIm as designed for one of the study patients. The 3DPrIm assembly consisted of a posterior shell with 3 mm thickness, containing a cranial back-stop, and an anterior shell with 5 mm thickness, with cut-outs to leave the patient's face open. The anterior shell was given projection lines that mark the localization point as stored during virtual treatment simulation, for daily assistance in initial patient setup. The 3DPrIm assembly was attachable to the treatment couch overlay with plastic clamps.
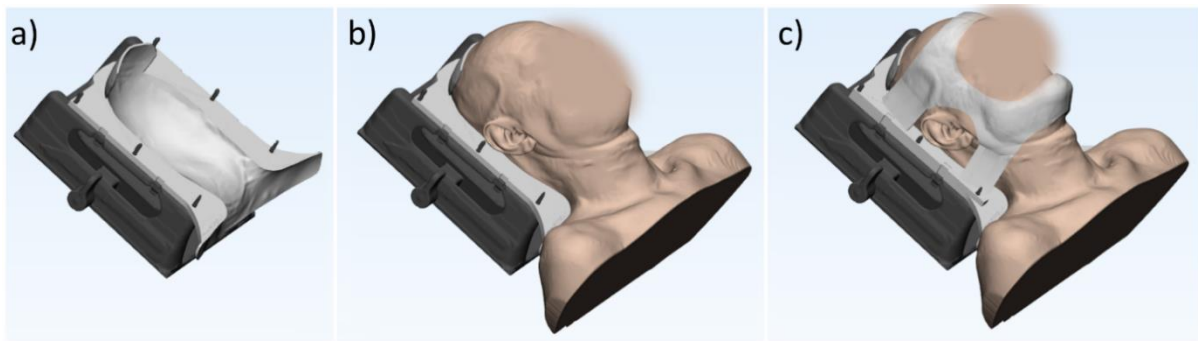
Figure 2. 3D printed immobilization assembly as designed for one of the study patients. A posterior shell with a cranial back-stop stop can be mounted on a commercially available treatment couch overlay **(a)** and serves as a patient-specific headrest **(b)**. An anterior shell is then mounted and fastened with plastic clamps **(c)**. Patient-specific characteristics have been censored for reasons of privacy.

Production of the 3D printed immobilization

The .STL-file of the posterior shell was converted to GCODE, printable on a fused depositioning modeling 3D printer (type N2 Plus, Raise3D, Costa Mesa, CA, USA), using the ideaMaker slicing engine software (version 3.1.6, Raise3D). Support structures were used for overhang angles above 60°, but support structures attached to the region touching the patient were avoided through careful orientation of the .STL during slicing. The main slicer settings were an infill density of 90%, six shells and a layer height of 0.25 mm. Polylactic acid (PLA) was used as filament material for the 3D printer, using an extrusion temperature of 215°C and a heated bed temperature of 60°C. 3D printing of the anterior shell was subcontracted to an external 3D printing service company (3D Hubs, Amsterdam, The Netherlands), due to the more complex shape of the object. The subcontractor was requested to use the same slicer settings as for the in-house 3D printed posterior shell and to likewise avoid support structures on regions touching the patient. The combined cost to obtain the 3DPrIm assembly was comparable with the price of the TM.

V.1.3   Clinical immobilization with a thermoplastic mask

The patients were treated when immobilized with the standard immobilization technique, using a reusable neck cushion (Orfit Industries) selected from a standard set to best conform to the patient's neck, and using a five-points TM with closed face (Type 33770/2MI, Orfit Industries). The TM was molded around the patient's head and shoulders prior to the acquisition of the planning CT and was mountable with

push-pins on a treatment couch overlay (Type 32148, Orfit Industries). A localization point was defined anteriorly to the C2 vertebra and was marked on the TM for daily initial patient setup. Treatment consisted of volumetric modulated arc therapy (VMAT) on a Halcyon fast-rotating O-ring linac (Varian Medical Systems) [9]. Daily initial setup in the treatment room consisted of aligning the marks on the TM with the in-room lasers. Image-guided treatment delivery was performed daily with kilovoltage (kV) CBCT, using the vendor-provided "Head" scan protocol (100 kVp, 139 mAs, full-fan, mm slice thickness) [10].

V.1.4   Evaluation of 3D printed immobilization

<u>Quality assurance of the 3D printed immobilization</u>
Weekly study CBCTs were acquired of the patients immobilized on the linac treatment couch with the 3DPrIm and compared with the clinical CBCTs of the patients immobilized with the TM on the same day. Prior to the first study CBCT-imaging of each patient, quality assurance (QA) of the 3DPrIm was performed, consisting of dry-run CBCT-imaging of the mounted 3DPrIm and subsequent in-silico evaluation of the fit to the patient's body. To this end, the 3DPrIm assembly was mounted on the treatment couch overlay, in its turn attached to the treatment couch. The treatment couch was manually moved such that the localization point marks on the 3DPrIm were aligned with the in-room lasers. The image acquisition isocenter of the study CBCT was positioned anteriorly to the C2 vertebra to match the clinically used acquisition isocenter. The same scan protocol was used as well. The described procedure thus allowed for study CBCT-imaging in a manner consistent with the clinically used image-guidance. For the QA procedure, the obtained CBCT-image of the 3DPrIm mounted on the treatment couch overlay was manually rigidly registered with the study planning CT, using six degrees of freedom (DOF) in the image registration module of the Eclipse treatment planning software (TPS) (Varian Medical Systems). Subsequently, gaps or overlapping regions between the blended images were qualitatively assessed and approximately measured manually on axial slices.

CBCT-based evaluation of setup accuracy

Regions-of-interest for setup accuracy evaluation

Evaluation of the setup accuracy achieved with either immobilization type was based on bony regions-of interest (ROI) in the head-and-neck region, as visualized in Figure 3: the occiput, mandible, C2, C6 and thyroid cartilage. These sub-ROIs were created with image thresholding of the respective planning CTs in the contouring module of the TPS, using a threshold range of [150 HU; 2000 HU] and with subsequent manual corrections.
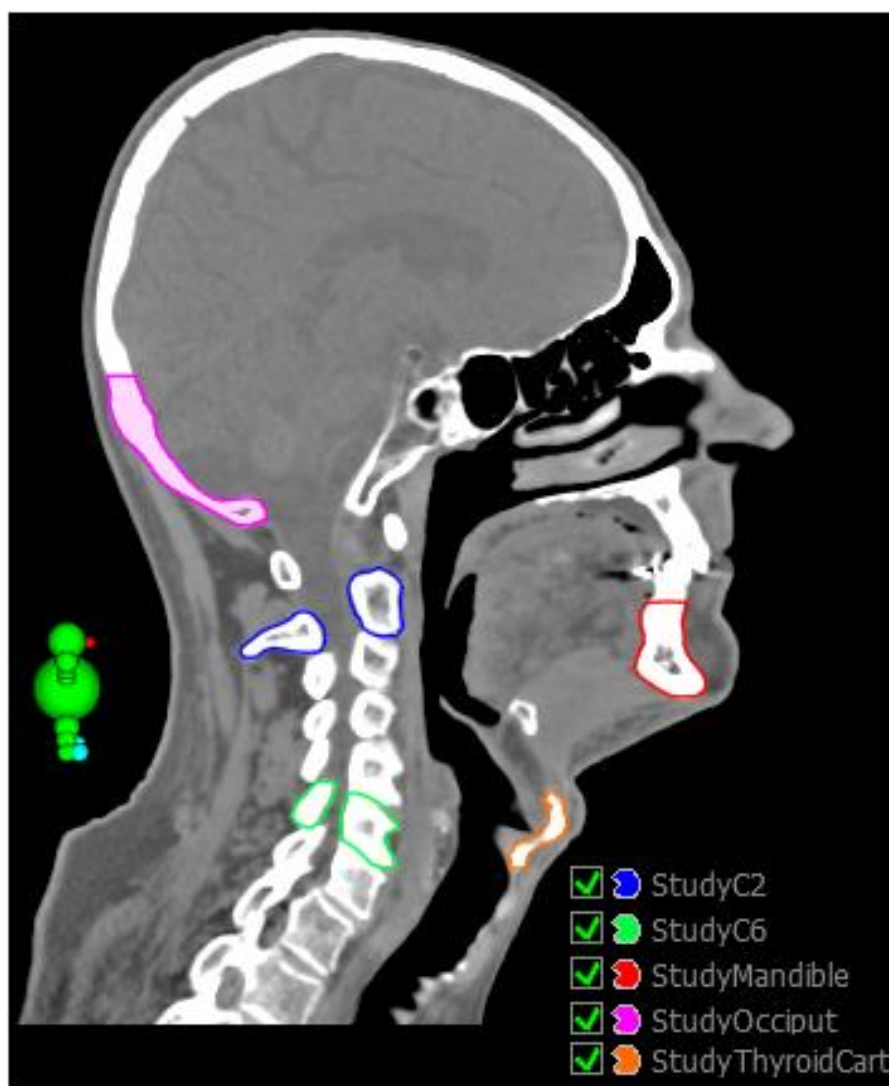
Figure 3. Sagittal view of a study planning CT, with bony landmark regions-of-interest used to evaluate setup accuracy of the 3D printed immobilization.

Global initial setup error

The global initial setup error was quantified by rigid registration of the weekly study CBCT and the clinical CBCT of the same day with their respective planning CT. The image registration was performed in the image registration module of the TPS and was based on a so-called "registration ROI (regROI)", i.e. a sub-ROI selected by the user to guide the image registration. The image registration then used six DOFs to maximize the normalized cross-correlation between the selected regROI (expanded with a 5 mm margin) on both images. As the focus of this feasibility study was on the head region, the rigid registration to quantify the global initial setup error was based on a composite regROI that consisted of the combined occiput and mandible. The obtained translations and rotations then represented the global setup error of the head region after initial patient setup in each fraction. The translations and rotations were defined as left-right (LR), anterior-posterior (AP) and cranio-caudal (CC). 3D-vector displacement errors – or 3D-errors – were calculated as well, as the root sum square of the errors in the three translational axes.

Local residual setup errors after virtual couch correction

A six DOF couch correction derived from the global registration allows to correct for the global initial setup error. Local residual setup errors remain present, however, due to the relative non-rigidity between the global, composite regROI and the individual sub-ROIs [11,12]. These local residual setup errors were quantified per sub-ROI by repeated additional registration, starting from the previous global registration. Each time, each individual sub-ROI served as the regROI for the additional registration. The local residual setup error per sub-ROI was then quantified as the difference between the global registration and the additional registration. These local residual setup errors were again quantified in the individual translational and rotational axes and the 3D-errors were calculated as well.

Statistical analysis

The 3D-errors at population level were tested for equality of the median between 3DPrIm and TM, using a Mann-Whitney U test with significance level p = 0.05. To distinguish the nature of the errors with either immobilization type, the different error components were calculated for the 3D-errors and for the errors in the individual

translational and rotational axes. The calculated error components were the group mean error M (= the mean of the intra-patient mean errors), the systematic error Σ (= the standard deviation of the intra-patient mean errors) and the random error σ (= the root means square of the intra-patient standard deviations of the error) [13]. These error components represent any bias in the patient-setup due to a deviation in the process (M), the inter-patient variation of the setup (Σ) and the inter-fraction variation of the setup (σ), respectively [13,14].

Questionnaire-based evaluation of comfort and usability

At the end of the RT course, the patients completed a questionnaire polling their experience in terms of claustrophobic feeling, experienced comfort, perceived residual movement, general experience, usability and patient-friendliness of either immobilization type. The three RTTs that were present at the largest number of study CBCTs completed a questionnaire as well, polling their experience in terms of ease of application, ease of patient positioning, perceived patient comfort, general experience, usability and patient-friendliness. The possible response to each question consisted of a five-level Likert scaling. The translated questions are listed in supplementary materials 2A and 2B.

V.2 Results

QA of the 3D printed immobilization

Figure 4 visualizes the study planning CT of a selected patient (patient B), blended with the CBCT of the 3DPrIm as used for the QA prior to the first usage. Rigid registrations to match both images required translations smaller than 5 mm in each axis and rotations smaller than 0.5° in each axis for all patients. Gaps between the 3DPrIm and the patients' body contour as measured manually were always below 1 mm for all patients.
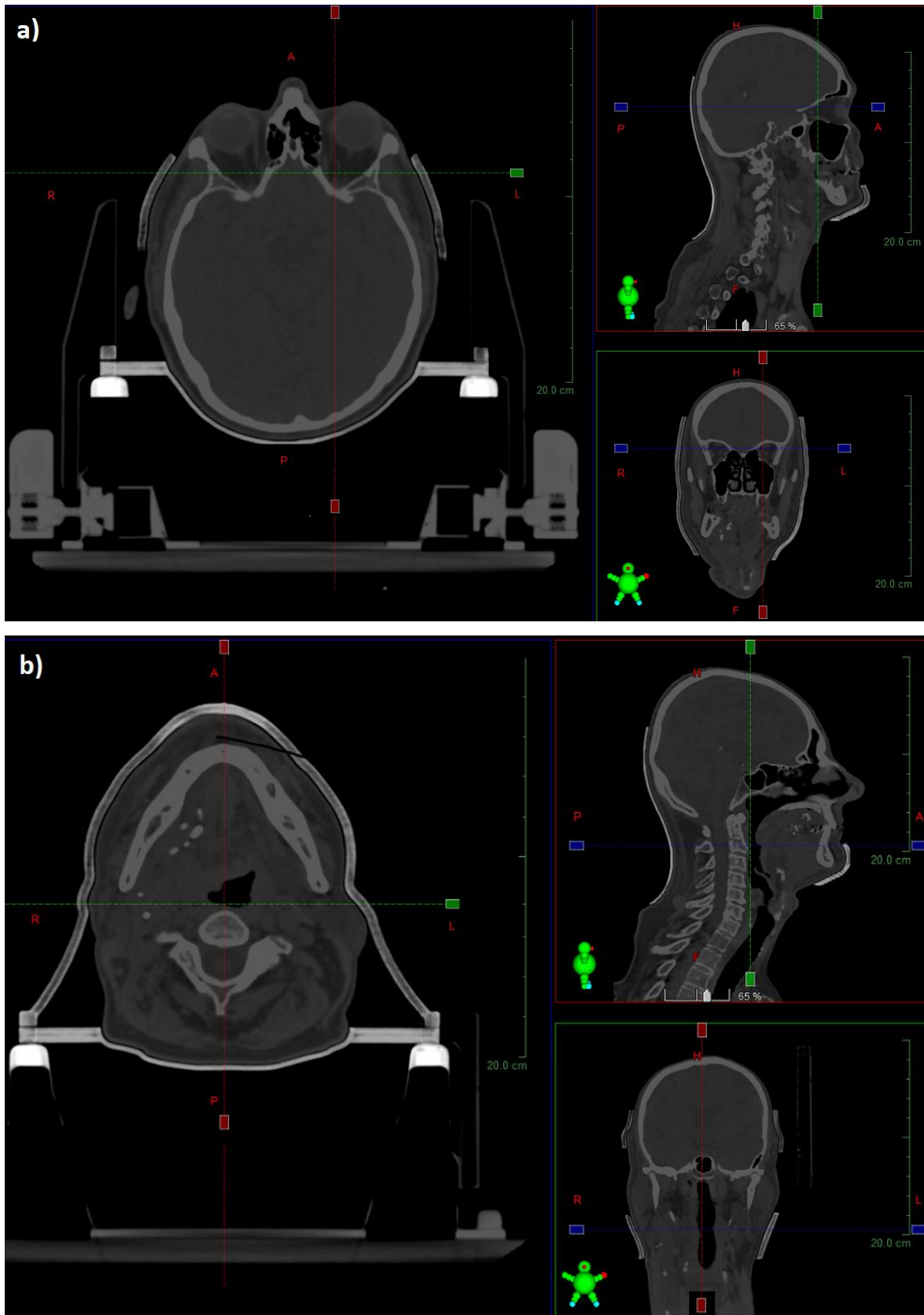
Figure 4. Visualization of the study planning CT of patient B, blended with the CBCT of the 3D printed immobilization as used for the quality assurance prior to the first usage. The visualized regions are the temporal bone region **(a)** and the mandible region **(b)**.

CBCT-based evaluation of setup accuracy

Five study CBCTs were acquired per patient. Figure 5 shows the last study CBCT, i.e. in the seventh of seven weeks of treatment, for patient B immobilized with a 3DPrIm. An enclosing fit of the 3DPrIm to the patient's head region can be observed.
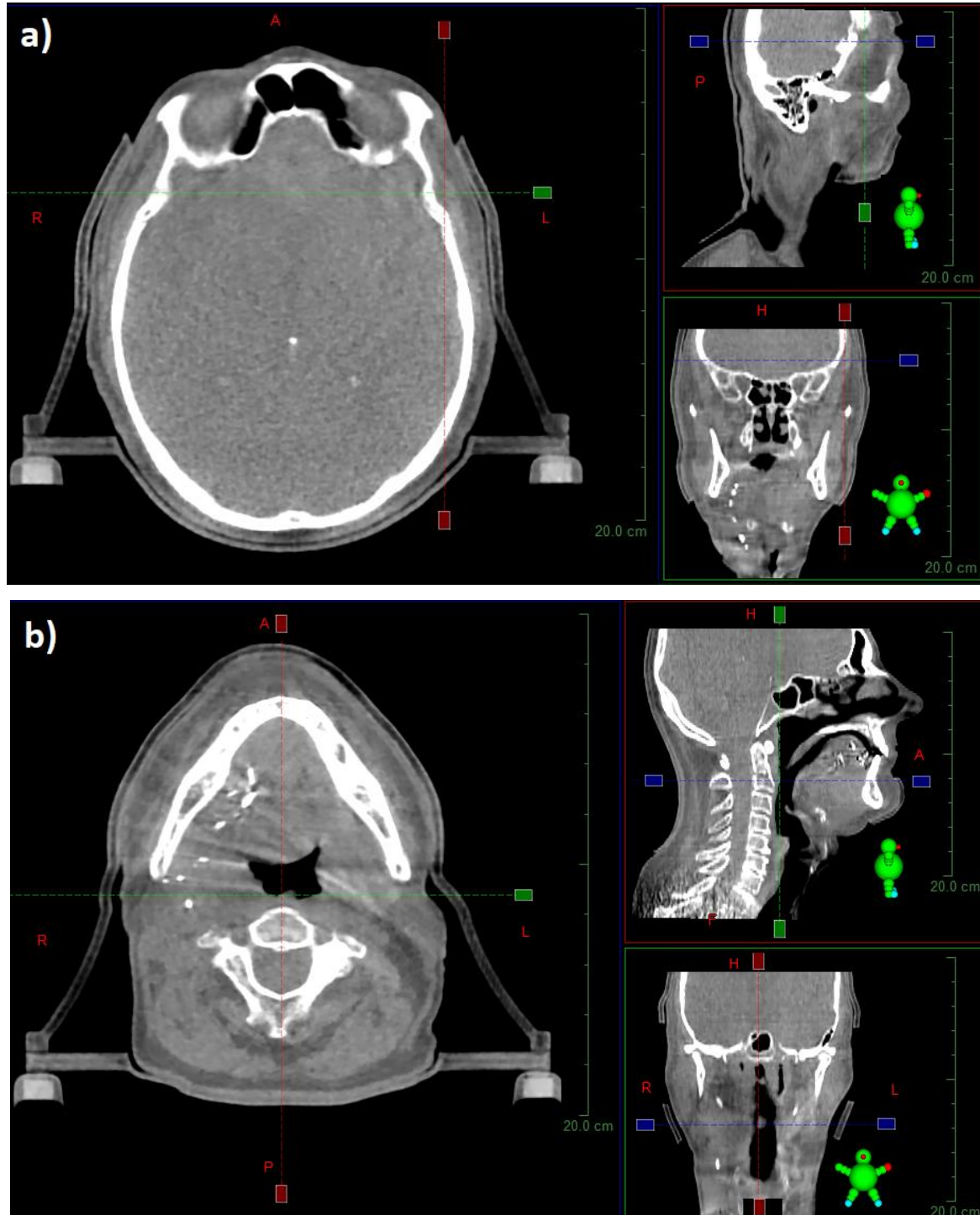
Figure 5. Visualization of the last study CBCT, i.e. in the seventh of seven weeks of treatment, for patient B immobilized with a 3D printed immobilization. The visualized regions are the temporal bone region **(a)** and the mandible region **(b)**. The study patient is the patient for which the QA of the 3D printed immobilization is shown in Figure 4.

Figure 6 shows the second study CBCT, i.e. in the second of seven weeks of treatment, for patient A immobilized with 3DPrIm. Despite the theoretical fit of the 3DPrIm to the patient's head region based on the QA, a gap can be observed in the mandible region.
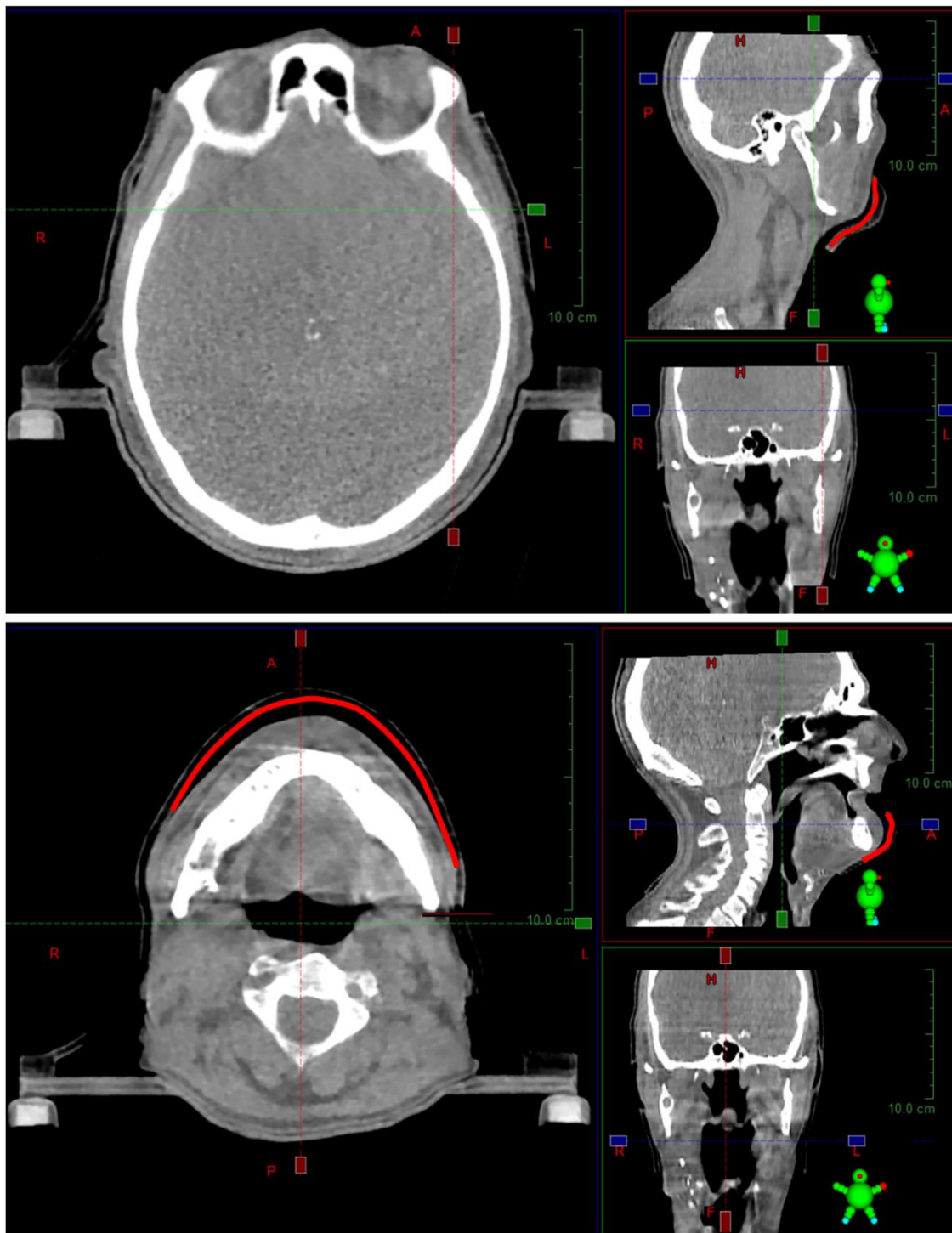
Figure 6. Visualization of the second study CBCT, i.e. in the second of seven weeks of treatment, for patient A immobilized with a 3D printed immobilization. The visualized regions are the temporal bone region **(a)** and the mandible region **(b)**. The inner border of the 3D printed immobilization is locally marked in red to highlight the gap in the mandible region observed for this particular patient.

3D-errors at population level

Figure 7(a) shows the boxplots for the global initial 3D-error of the head region, while figure 7(b) shows the local residual 3D-errors after virtual couch correction. The median of the global initial 3D-error and the median of the local residual 3D-error for the occiput and mandible were lower with 3DPrIm than with TM, but a statistically significant difference was only found for the occiput. For the more caudally located sub-ROIs, the median local residual 3D-error was comparable between both immobilization types for C2 and for the thyroid cartilage, but was notably higher with 3DPrIm for C6, although without statistical significance. The maximum local residual 3D-error for C2, C6 and the thyroid cartilage was higher as well with 3DPrIm than with TM.
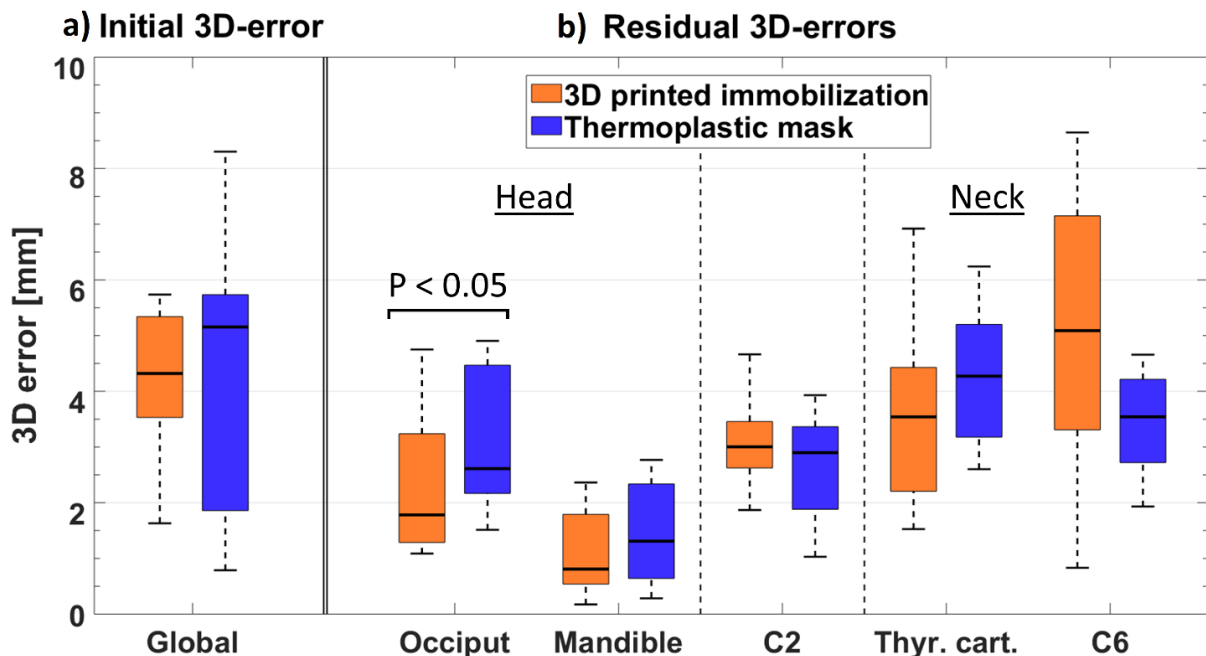
Figure 7. a) Boxplots for the global initial 3D-error of the head region, based on a global 6DOF registration of the CBCT after initial patient setup with the planning CT. **b)** Boxplots for the local residual 3D-errors per sub-ROI, based on subsequent 6 DOF registration with each individual sub-ROI serving as the registration ROI. The boxplots are based on 15 CBCTs per immobilization type.

Group mean errors M, systematic errors Σ and random errors σ

The different error components are displayed in Table 2 (global initial setup errors of the head region), in Table 3 (local residual setup errors of the sub-ROIs in the head region) and in Table 4 (local residual setup errors of the more caudally located sub-ROIs).

Figure 8 visualizes the 1D group mean error M and the systematic error Σ in two directions in the sagittal plane. Herein, the group mean error M represents any bias in the patient-setup due to a deviation in the process [13,14]. This group mean error appeared to be reduced with 3DPrIm compared with TM for the occiput and appeared to be similar between both immobilization types for the mandible and for C2. For C6 and for the thyroid cartilage, the group mean error was notably larger with 3DPrIm than with TM. Furthermore, the systematic error Σ represents the inter-patient variation in setup and therefore the inter-patient systematics in patient positioning [13,14]. For all the studied sub-ROIs, this systematic error appeared to be similar to reduced with 3DPrIm compared with TM.
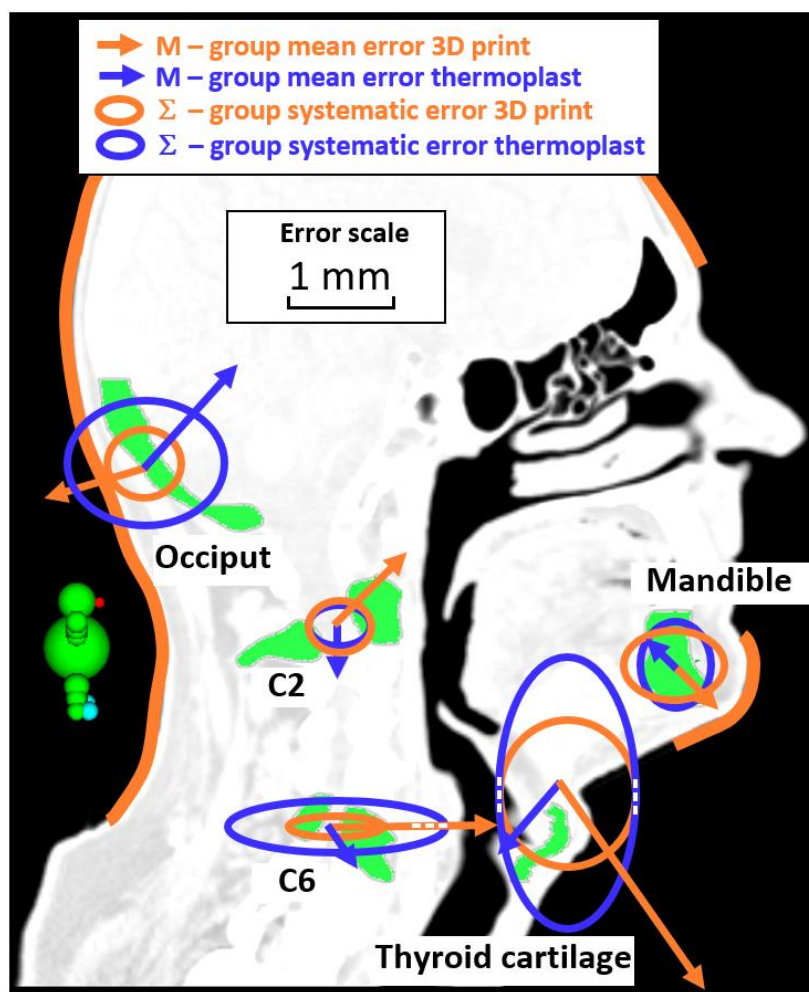
Figure 8. 1D group mean errors M and systematic errors Σ in two directions in the sagittal plane. The group mean error M is represented by the scaled arrow length. The systematic error Σ is represented by the scaled length of the two axes of each ellipse. The shown error scale does not apply to $M_{3DPrint}$ for C6 and to $Σ_{Thermoplast}$ for the thyroid cartilage: these metrics are visualized shorter than their real value to maintain clarity of the figure.

Table 2. Group mean (M), systematic (Σ) and random (σ) error components for the global initial setup errors of the head region as determined with a rigid registration between the CBCT and the respective planning CT, making use of a composite registration ROI of the occiput combined with the mandible.

		M		Σ		σ	
		3DP	TM	3DP	TM	3DP	TM
Translation	3D [mm]	4.0	4.4	1.0	2.7	1.2	1.3
	LR [mm]	1.1	-1.0	1.9	3.0	0.9	1.2
	AP [mm]	1.0	0.7	2.3	2.4	1.6	1.5
	CC [mm]	-1.0	1.3	2.5	2.3	1.2	1.6
Rotation	LR [°]	-1.2	-1.7	1.4	0.5	1.0	0.9
	AP [°]	0.5	0.1	0.4	1.6	0.4	0.5
	CC [°]	-0.1	-0.5	0.3	1.1	0.6	0.9

Abbreviations: M = group mean error; Σ = systematic error; σ = random error; 3DPrIm = 3D printed immobilization; TM = thermoplastic mask with generic headrest; LR = left-right; AP = anterio-posterior; CC = cranio-caudal.

Table 3. Group mean (M), systematic (Σ) and random (σ) error components for the local residual setup errors of the sub-ROIs in the head region.

		Occiput M 3DP	Occiput M TM	Occiput Σ 3DP	Occiput Σ TM	Occiput σ 3DP	Occiput σ TM	Mandible M 3DP	Mandible M TM	Mandible Σ 3DP	Mandible Σ TM	Mandible σ 3DP	Mandible σ TM
	3D [mm]	2.1	2.9	0.6	0.9	1.1	1.1	1.3	1.6	1.0	1.0	0.7	1.2
Translation	LR mm]	-0.5	-0.2	0.2	1.7	0.6	1.1	-0.1	-0.3	0.1	0.6	0.2	0.4
	AP [mm]	1.0	-0.9	0.7	1.5	1.4	1.4	-0.4	0.3	1.0	0.7	0.6	1.3
	CC [mm]	0.3	-1.0	0.6	1.2	0.8	0.8	0.4	-0.3	0.7	0.8	0.7	1.1
Rotation	LR [°]	-0.8	1.0	0.3	1.0	1.0	0.8	-0.1	-1.8	1.0	1.3	0.6	0.5
	AP [°]	-0.3	0.0	0.2	0.6	0.3	0.4	0.0	-1.0	0.1	1.1	0.1	0.6
	CC [°]	-0.2	0.1	0.4	1.2	0.4	0.6	-0.4	-0.3	0.9	0.4	0.4	1.1

Abbreviations: M = group mean error; Σ = systematic error; σ = random error; 3DP = 3D printed immobilization; TM = thermoplastic mask with headrest; LR = left-right; AP = anterio-posterior; CC = cranio-caudal.

Table 4. Group mean (M), systematic (Σ) and random (σ) error components for the local residual setup errors of C2 and of the sub-ROIs in the neck region.

	C2 M 3DP	C2 M TM	C2 Σ 3DP	C2 Σ TM	C2 σ 3DP	C2 σ TM	C6 M 3DP	C6 M TM	C6 Σ 3DP	C6 Σ TM	C6 σ 3DP	C6 σ TM	Thyroid M 3DP	Thyroid M TM	Thyroid Σ 3DP	Thyroid Σ TM	Thyroid σ 3DP	Thyroid σ TM
3D [mm]	3.0	2.6	0.2	0.5	0.9	1.0	4.8	3.5	0.9	0.6	2.6	1.4	3.5	4.3	1.0	0.7	1.4	1.1
LR [mm]	-0.7	0.3	0.7	1.6	1.0	1.5	-0.8	1.2	0.4	1.8	1.1	2.1	0.6	-0.3	0.1	1.7	1.0	1.8
AP[mm]	-0.7	0.0	0.6	0.6	0.9	1.8	-4.4	-0.3	0.9	2.1	2.7	1.8	-1.4	0.6	1.3	1.3	1.5	1.4
CC mm]	-0.7	0.5	0.5	0.4	1.0	1.1	-0.1	0.4	0.1	0.5	0.7	0.9	2.0	0.7	1.4	3.9	1.9	1.1
LR [°]	3.0	-0.6	1.4	0.6	2.4	1.5	-0.2	0.3	3.2	0.4	1.8	1.0	1.2	2.1	2.9	2.0	1.9	1.9
AP [°]	-0.7	0.0	0.2	0.4	0.8	0.6	-0.6	-0.1	0.6	2.5	1.5	1.2	-2.1	-1.5	0.8	2.3	2.0	1.9
CC [°]	-1.7	1.1	1.0	2.4	0.9	1.1	-0.7	0.3	1.3	1.3	1.5	1.3	-1.2	-0.9	2.0	2.7	1.4	1.1

Abbreviations: M = group mean error; Σ = systematic error; σ = random error; 3DP = 3D printed immobilization; TM = thermoplastic mask with headrest; LR = left-right; AP = anterio-posterior; CC = cranio-caudal.

Questionnaire-based evaluation of comfort and usability

The responses to the patient and RTT questionnaires are visualized in Figure 9. No patients reported feelings of claustrophobia or discomfort with 3DPrIm. One patient reported increased perceived residual movement allowed by 3DPrIm compared with TM. All three RTTs reported easy positioning of the patient with and easy application of the 3DPrIm. All patients and RTTs reported a positive general experience with 3DPrIm and evaluated 3DPrIm as a usable and patient-friendly auxiliary for immobilization.
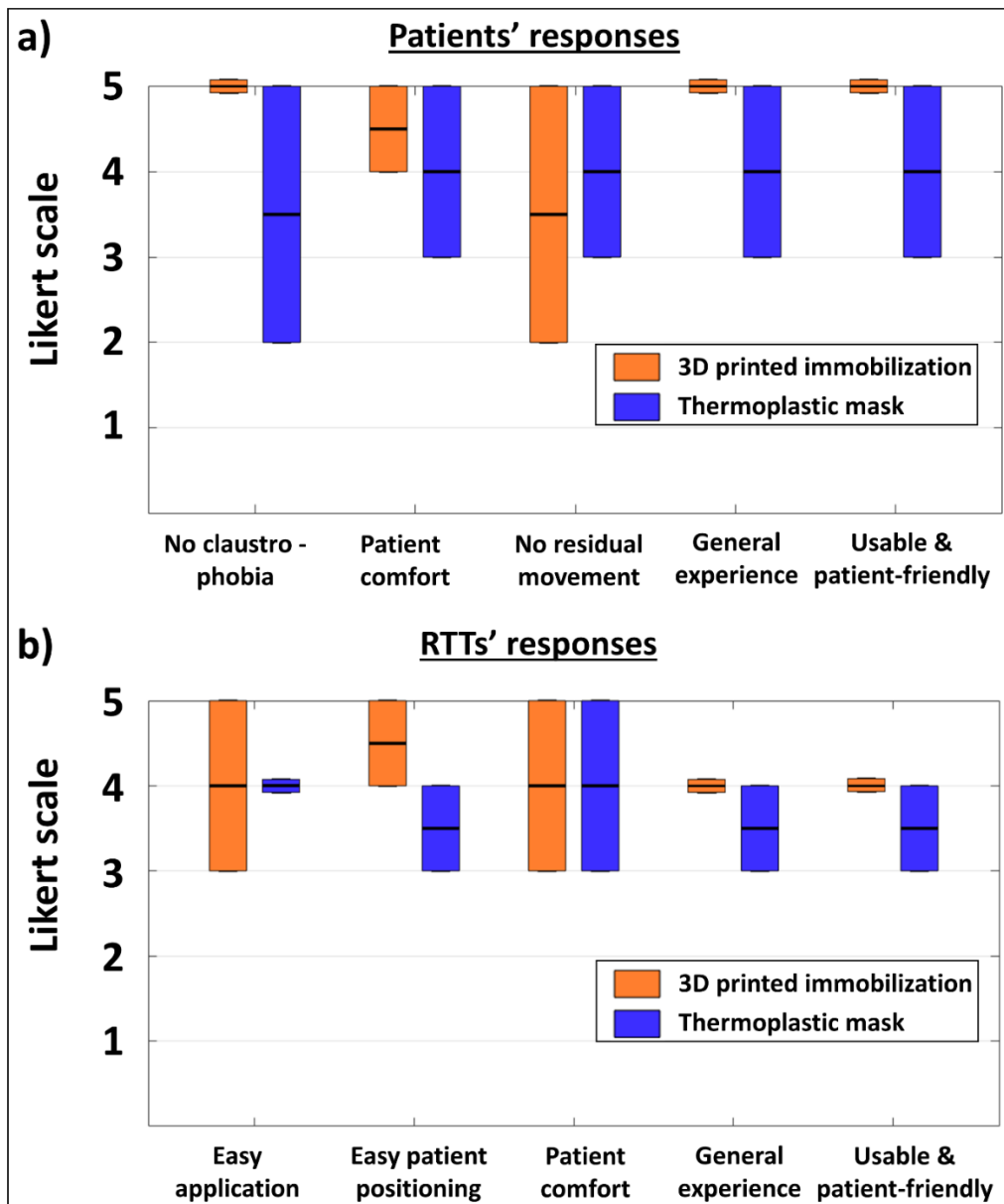
Figure 9. Questionnaire responses as given by the three study patients **(a)** and by the three most involved RTTs **(b)**. The lowest, middle and highest Likert-score per question are shown. The higher the Likert-scores, the better the immobilization performed.

V.3 Discussion

3D printing is a versatile manufacturing technology that could enhance patient immobilization for RT of HNC. The use of 3DPrIm instead of molded TMs may allow to integrate additional functionalities within the immobilization, such as bolus RS for IMPT of HNC, hereby reducing spot size and hardware collision risk compared with nozzle-mounted RS. Such integrated device also would ensure presence and correct placement of the RS for each treatment field and may simplify the overall IMPT delivery workflow by reducing the number of hardware manipulations. While 3DPrIm of the head region has been previously studied on healthy volunteers [15], to the authors' knowledge the current study is the first to report on 3DPrIm of actual patients, including CBCT-based evaluation. 3DPrIm was shown feasible in terms of workflow, was shown tolerable by patients with HNC and achieved clinically acceptable setup accuracy for the head region. Nevertheless, further optimization of the initial design, with added lower neck immobilization, is required towards clinical use of 3DPrIm in RT of HNC.

The proposed method of 3DPrIm greatly differs from the widely adopted method using TMs. Specifically, 3DPrIm cannot be made in the physical presence of the patient and thus requires a new RT workflow using any captured information on the patient's external anatomy. Other studies have used optical scanning to capture this information [16–19], but the required 360° field of view and the presence of opaque hair may limit the use of such approach for the creation of 3DPrIm for the head-and-neck region. Therefore, in the current study a mask-less planning CT acquisition workflow was established. Extraction of the body contour from this CT image, however, generates an uncertainty on the fit of the 3DPrIm to the patient. The optimal threshold value to obtain the body contour was experimentally determined on an anthropomorphic phantom, but may be different for actual patients. The QA procedure used in this study provided some level of confidence of the fit, but cannot be considered a fully independent verification method, as both the creation and the verification of the 3DPrIm were based on volumetric kV-imaging. Nevertheless, the fit of the 3DPrIm to the patients was deemed acceptable based on the study CBCT images (see for instance Figure 5). Further increasing the threshold value used for the body contour segmentation may improve the quality of the immobilization, but may go at the expense of patient comfort, a trade-off that could be optimized in further study.

As a first step towards 3DPrIm of patients with HNC, the current study focused on immobilization of the head region. Both the residual 3D-errors (Figure 7) and the 1D error components (Figure 8) for the sub-ROIs in this region suggested a setup accuracy of the head with 3DPrIm which was at least comparable to that with a TM and a standard headrest. The small patient sample size, however, only allowed for a limited statistical comparison. In addition, the immobilization technique used as a reference for comparison may be considered sub-optimal, as the use of an individualized headrest has been shown to improve patient setup reproducibility compared with a standard headrest [20]. Nevertheless, this reference technique is clinically used to effectively treat patients with HNC and showed local residual setup errors similar to those reported elsewhere [11]. In this regard, the presented data on setup accuracy achieved with 3DPrIm, combined with the positive general experience reported by all study patients, indicate feasibility of 3DPrIm of patients with HNC, which was the purpose of this study.

The potentially increased patient-specific approximation of the body outline with 3DPrIm may be expected to reduce inter-fractional setup variations compared with TMs. For high-precision TM solutions, however, using a patient-specific headrest and biteblock, smaller local residual setup errors have been reported than the group errors found for the 3DPrIm in the current study [21]. A large conceptual difference exists between both types of immobilization, however, as only for the 3DPrIm the face region remains open. On one hand, open face immobilization may increase patient comfort and allows for intra-fraction motion monitoring using optical surface scanning [22,23]. On the other hand, open face immobilization allows for more degrees of freedom for the head position prior to application of the immobilization, which may increase inter-fractional positional variation. In the current study, this has been observed for a number of study CBCTs for patient A, of which an example was shown in Figure 6. Although the QA of the 3DPrIm for this patient showed no notable gaps between the 3DPrIm and the patient's body, considerable (>1 mm) gaps at the level of the mandible were seen on three out of the five study CBCTs. Such effects may be mitigated by the use of optical surface scanning to guide initial patient positioning prior to application of the anterior part of the 3DPrIm assembly. In addition, the 3DPrIm design may be further optimized, for instance by further enclosing the anterior shell around the patient, at the level of the cranial back-stop, the nose bridge and the upper lip.

The systematic errors Σ with 3DPrIm were similar to reduced compared with a clinically used TM solution for all the studied sub-ROI's. Such reduced Σ may result from a more systematic immobilization approach achieved with a fully patient-specific 3DPrIm compared with a TM and a generic headrest. On the other hand, considerably larger group mean errors M could be observed with 3DPrIm compared with TM for the more caudally located sub-ROIs (C6 and thyroid cartilage and to a lower extent C2). Such increased M may indicate a deviation at the process level, with inherent position differences between the study planning CT and the study CBCT [13,14]. Indeed, the current design of the 3DPrIm provided no immobilization of the shoulders and lower neck, such that for instance relaxation as the RT course evolves may result in different positions of C6 between the study CBCTs and the study planning CT. The use of hand grip poles during both the planning CT and study CBCTs and caudal extension of both shells of the 3DPrIm assembly, down to the lower neck region, therefore presumably are necessary improvements steps for 3DPrIm to serve as a valid immobilization option for RT of HNC.

A caudal extension of the 3DPrIm likewise is necessary to provide clinically relevant bolus RS integration options, since IMPT of HNC commonly involves superficial irradiation of the lower neck levels [6,24–27]. 3DPrIm extended to the neck area, however, is likely not attachable to the treatment couch overlay used in the current study. In addition, the used treatment couch overlay presents geometric and potentially stopping power related gradients perpendicular to the proton beam directions, which are to be avoided in clinical IMPT [28–30]. Further development of 3DPrIm for IMPT of HNC, therefore, would require adaptation of the current design to be attachable to a suitable treatment couch overlay or insert.

In conclusion of this study, 3DPrIm of the head region is feasible in terms of workflow, is tolerable by HNC patients during their course of RT and can achieve clinically acceptable setup accuracy for the head region. 3DPrIm therefore is a valid option to pursue enhancements in RT of HNC, such as spot-size reducing bolus in IMPT. Although HNC patients were subject of this 3DPrIm study, the proposed design requires further optimization and extension to the lower neck region to serve as a valid immobilization option for RT of HNC.

Acknowledgments
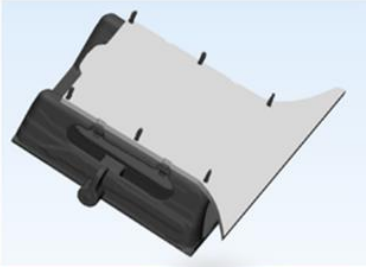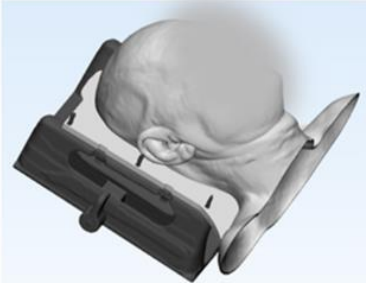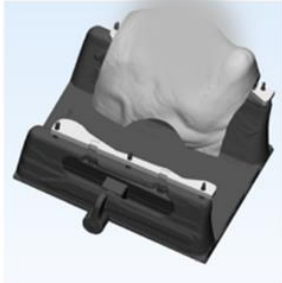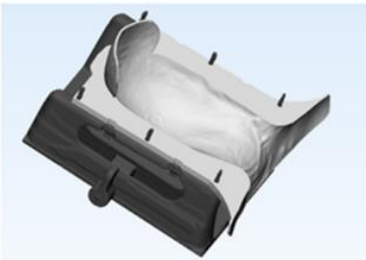
References

[1]   Leeman JE, Romesser PB, Zhou Y, McBride S, Riaz N, Sherman E, et al. Proton therapy for head and neck cancer: expanding the therapeutic window. Lancet Oncol 2017;18:e254−65.

[2]   Langendijk JA, Doornaert P, Verdonck-de Leeuw IM, Leemans CR, Aaronson NK, Slotman BJ. Impact of late treatment-related toxicity on quality of life among patients with head and neck cancer treated with radiotherapy. J Clin Oncol 2008;26:3770−6.

[3]   Van De Water TA, Lomax AJ, Bijl HP, De Jong ME, Schilstra C, Hug EB, et al. Potential benefits of scanned intensity-modulated proton therapy versus advanced photon therapy with regard to sparing of the salivary glands in oropharyngeal cancer. Int J Radiat Oncol Biol Phys 2011;79:1216−24.

[4]   Eekers DBP, Roelofs E, Jelen U, Kirk M, Granzier M, Ammazzalorso F, et al. Benefit of particle therapy in re-irradiation of head and neck patients. Results of a multicentric in silico ROCOCO trial. Radiother Oncol 2015;121:387−94.

[5]   van de Water S, van Dam I, Schaart DR, Al-Mamgani A, Heijmen BJM, Hoogeman MS. The price of robustness; impact of worst-case optimization on organ-at-risk dose and complication probability in intensity-modulated proton therapy for oropharyngeal cancer patients. Radiother Oncol 2016;120:56−62.

[6]   Michiels S, Barragán AM, Souris K, Poels K, Crijns W, Lee JA, et al. Patient-specific bolus for range shifter air gap reduction in intensity- modulated proton therapy of head-and-neck cancer studied with Monte Carlo based plan optimization. Radiother Oncol 2018;128:161−6.

[7]   Ali I, Tubbs J, Hibbitts K, Algan O, Thompson S, Herman T, et al. Evaluation of the setup accuracy of a stereotactic radiotherapy head immobilization mask system using kV on-board imaging. J Appl Clin Med Phys 2010;11:26−37.

[8]   Fedorov A, Beichel R, Kalpathy-Cramer J, Finet J, Fillion-Robin JC, Pujol S, et al. 3D

Slicer as an image computing platform for the Quantitative Imaging Network. Magn Reson Imaging 2012;30:1323–41.

[9] Michiels S, Poels K, Crijns W, Delombaerde L, De Roover R, Vanstraelen B, et al. Volumetric modulated arc therapy of head-and-neck cancer on a fast-rotating O-ring linac: Plan quality and delivery time comparison with a C-arm linac. Radiother Oncol 2018;128:479–84.

[10] Cai B, Laugeman E, Mazur TR, Park JC, Henke LE, Kim H, et al. Characterization of a prototype rapid kilovoltage x-ray image guidance system designed for a ring shape radiation therapy unit. Med Phys 2019;46:1355–70.

[11] van Kranen S, van Beek S, Rasch C, van Herk M, Sonke JJ. Setup Uncertainties of Anatomical Sub-Regions in Head-and-Neck Cancer Patients After Offline CBCT Guidance. Int J Radiat Oncol Biol Phys 2009;73:1566–73.

[12] Giske K, Stoiber EM, Schwarz M, Stoll A, Muenter MW, Timke C, et al. Local setup errors in image-guided radiotherapy for head and neck cancer patients immobilized with a custom-made device. Int J Radiat Oncol Biol Phys 2011;80:582–9.

[13] Van Herk M. Errors and Margins in Radiotherapy. Semin Radiat Oncol 2004;14:52–64.

[14] Yan D, Lockman D, Martinez A, Wong J, Brabbins D, Vicini F, et al. Computed tomography guided management of interfractional patient variation. Semin Radiat Oncol 2005;15:168–79.

[15] Haefner MF, Giesel FL, Mattke M, Rath D, Wade M, Kuypers J, et al. 3D-Printed masks as a new approach for immobilization in radiotherapy-a study of positioning accuracy. Oncotarget 2018;9:6490–8.

[16] Sasaki DK, Mcgeachy P, Aviles JEA, Mccurdy B, Koul R, Dubey A. A modern mold room: Meshing 3D surface scanning, digital design, and 3D printing with bolus fabrication. J Appl Clin Med Phys 2019;20:78–85.

[17] Sharma A, Sasaki D, Rickey DW, Leylek A, Harris C, Johnson K, et al. Low-cost optical scanner and 3D printing technology to create lead shielding for radiotherapy of facial skin cancer: first clinical case series. Adv Radiat Oncol 2018;3:288–96.

[18] Arimura T, Ogino T, Yoshiura T, Matsuyama M, Kondo N, Miyazaki H, et al. A feasibility study of a hybrid breast-immobilization system for early breast cancer in proton beam therapy: Med Phys 2017;44:1268–74.

[19] Dipasquale G, Poirier A, Sprunger Y, Uiterwijk JWE, Miralbell R. Improving 3D-printing of megavoltage X-rays radiotherapy bolus with surface-scanner. Radiat Oncol 2018;13:203.

[20] Houweling AC, van der Meer S, van der Wal E, Terhaard CHJ, Raaijmakers CPJ. Improved immobilization using an individual head support in head and neck cancer patients. Radiother Oncol 2010;96:100–3.

[21] Mesko S, Wang H, Tung S, Wang C, Pasalic D, Chapman B V., et al. Estimating PTV margins in head and neck stereotactic ablative radiation therapy (SABR) through target site analysis of positioning and intrafractional accuracy. Int J Radiat Oncol Biol Phys 2019:In press.

[22] Dekker J, Rozema T, Böing-Messing F, Garcia M, Washington D, de Kruijf W. Whole-brain radiation therapy without a thermoplastic mask. Phys Imaging Radiat Oncol 2019;11:27−9.

[23] Zhao B, Maquilan G, Jiang S, Schwartz DL. Minimal mask immobilization with optical surface guidance for head and neck radiotherapy. J Appl Clin Med Phys 2018;19:17−24.

[24] Cubillos-Mesías M, Troost EGC, Lohaus F, Agolli L, Rehm M, Richter C, et al. Including anatomical variations in robust optimization for head and neck proton therapy can reduce the need of adaptation. Radiother Oncol 2019;131:127−34.

[25] Hamming-Vrieze O, Depauw N, Craft DL, Chan AW, Rasch CRN, Verheij M, et al. Impact of setup and range uncertainties on TCP and NTCP following VMAT or IMPT of oropharyngeal cancer patients. Phys Med Biol 2019;64:095001.

[26] Frank SJ, Cox JD, Gillin M, Mohan R, Garden AS, Rosenthal DI, et al. Multifield optimization intensity modulated proton therapy for head and neck tumors: A translation to practice. Int J Radiat Oncol Biol Phys 2014;89:846−53.

[27] Kraan AC, Van De Water S, Teguh DN, Al-Mamgani A, Madden T, Kooy HM, et al. Dose uncertainties in IMPT for oropharyngeal cancer in the presence of anatomical, range, and setup errors. Int J Radiat Oncol Biol Phys 2013;87:888−96.

[28] Olch AJ, Gerig L, Li H, Mihaylov I, Morgan A. Dosimetric effects caused by couch tops and immobilization devices: report of AAPM Task Group 176. Med Phys 2014;41:061501.

[29] Wroe AJ, Bush DA, Slater JD. Immobilization Considerations for Proton Radiation Therapy. Technol Cancer Res Treat 2013;13:217−26.

[30] Wroe AJ, Ghebremedhin A, Gordon IR, Schulte SRW, Slater JD. Water Equivalent Thickness Analysis of Immobilization Devices for Clinical Implementation in Proton Therapy. TCRT Express 2013;1:83−8.

POSTERIOR

ANTERIOR

Design step	Used software functionality
Creation of attachment plates	
- 8mm thick plate, with plate thickness, hole dimensions and hole positions adopted from a commercial dual-mask system	Sketch > Create line Design > Extrude
- Outline adjusted to follow the projection of the patient's body contour	Sketch > Import references Design > Extrude Design > Boolean subtraction
Creation of complete patient shell	
- Uniform expansion of the patient's body contour, using a distance value of 3 mm and 5 mm for the posterior and anterior shell, respectively	Design > Uniform offset"
- Patient's body contour subtracted to obtain shell	Design > Boolean subtraction

- For the anterior part:
  - Manual removal of regions of convex curvature
    preventing application of the shell on the patient's head
	Design > Boolean subtraction

Creation of anterior and posterior shell	
- For the posterior part - Removal of anterior part of the shell, with the exception of a cranial stop	Design > Boolean subtraction
- For the anterior part - Removal of face covering parts	Finish > Trim
- Creation of connecting parts	Design > Revolve
- Creation of laser lines with 0.5 mm thickness	Design > Create box at laser origins Design > Uniform offset" Design > Boolean intersect"

Supplementary material 1. Design steps to create a 3D printable immobilization assembly fit to the patient's body contour. Patient-specific characteristics have been censored for reasons of privacy.

Supplementary material 2A. Questionnaires polling the experience of the three <u>study patients</u> in terms of comfort, perceived immobilization quality and usability of either type of immobilization.

- The used immobilization made me feel **claustrophobic**.
- The used immobilization is **comfortable.**
- The used immobilization still allowed for **residual movement**.
- The used immobilization gave me a **good general experience**.
- The used immobilization is a **usable** and **patient-friendly** auxiliary for immobilization during radiotherapy.

Strongly disagree	Disagree	Neutral	Agree	Strongly agree

Supplementary material 2B. Questionnaires polling the experience of the three <u>radiation therapy technologists</u> in terms of comfort, perceived immobilization quality and usability of either type of immobilization.

- The used immobilization can be **easily applied**.
- The used immobilization allows for **easy positioning** of the patient.
- The used immobilization allows to realize **patient comfort**.
- The used immobilization gave me a **good general experience**.
- The used immobilization is a **usable** and **patient-friendly** auxiliary for immobilization during radiotherapy.

Strongly disagree	Disagree	Neutral	Agree	Strongly agree

General discussion & future perspectives VI

The general aim of this thesis was to improve radiotherapy (RT) of head-and-neck cancer (HNC) by the optimization and the implementation of **emerging technologies**. To this end, a fast-rotating **O-ring linac,** optimized for fast image-guided delivery of intensity-modulated photon beams, was clinically implemented for volumetric modulated arc therapy (VMAT) of HNC. The fast-rotating O-ring linac was demonstrated to maintain the plan quality of a conventional C-arm linac, while reducing the volumetric image acquisition and plan delivery time. Next, the potential of **3D printing technology** to optimize **intensity-modulated proton therapy** (IMPT), with the use of range shifter (RS) air gap minimizing bolus integrated within the patient immobilization, was shown. Firstly, the development of patient-specific bolus RS for IMPT of HNC was motivated by theoretically showing clinically relevant toxicity reductions compared with conventional snout-mounted RS. Secondly, an in-depth characterization of different 3D printing materials and technologies was performed and a proof-of-concept for use of 3D printed RS in a clinical workflow was presented. Lastly, the use of 3D printing to realize immobilization of patients with HNC was proven feasible in terms of workflow, patient comfort and setup reproducibility. As such, with the implementation of 3D printing technology, important steps were taken towards a single, patient-specific device that achieves spot size reduction, hardware manipulation minimization and patient immobilization for IMPT of HNC.

VI.1 Clinical implementation of O-ring linac technology

VI.1.1 Specific objectives and main findings

In recent years, the use of O-ring linac systems in RT has been gradually increasing. The enclosed and toroidal geometry of such systems allows for designs with specific advantages compared with conventional C-arm linacs [1,2]. A commercially available fast-rotating O-ring linac with fast-moving leaves, for instance, was optimized for time-efficient image-guided delivery of intensity-modulated photon beams. The first objective of this thesis was to compare the fast-rotating O-ring linac with a conventional C-arm linac in terms of plan quality and delivery time for VMAT of HNC, as elaborated in chapter II. For a cohort of 30 patients with HNC, triple-arc VMAT on

the fast-rotating O-ring linac achieved the target coverage objectives while minorly reducing the expected xerostomia probability (median reduction 0.8%]) and dysphagia probability (median reduction 1.0%) compared with the commonly used dual-arc VMAT on a C-arm linac. In addition, plan delivery accuracy of triple-arc VMAT on the fast-rotating O-ring linac was proven with $\Gamma_{3\%,3mm}$ agreement scores for helical diode array measurements never below 95.2%. Lastly, volumetric imaging and plan delivery time was reduced with 53s on average compared with a C-arm linac. The presented study hereby was the first to show **at least maintained plan quality for VMAT of HNC on the fast-rotating O-ring linac while improving time-efficiency compared with a C-arm linac**.

VI.1.2   Clinical implementation and system evolution

Based on the results of presented study, **daily CBCT-guided triple-arc VMAT of HNC was implemented on the fast-rotating O-ring linac at the authors' institute**. Prior to actual patient treatment, a complementary study independently verified plan delivery accuracy with end-to-end testing using radiochromic film and ionization chamber measurements on an anthropomorphic head phantom [3].

The studied fast-rotating O-ring linac contains a jawless multi-leaf collimator, composed of two staggered layers of 28 leaf pairs. The Eclipse (Varian Medical Systems, Palo Alto, CA) treatment planning software (TPS) version 15.1 as used for the study in chapter II, however, allowed for the field shaping to be performed only by the distal leaves, while the corresponding proximal leaves were obliged to assume the same position. Independent optimization of both leaf layers, allowed by Eclipse version 15.6, could increase the effective modulation resolution and could therefore improve organ-at-risk (OAR) sparing [4]. Nevertheless, even with independent leaf layer optimization, Cozzi et al. found only minor differences in plan quality for VMAT of HNC on the fast-rotating O-ring linac compared with a C-arm linac [5]. The improvement in OAR sparing associated with independent leaf layer optimization, therefore, presumably is negligible for VMAT of large, complex target geometries such as in HNC.

Since the start of treatments on the fast-rotating O-ring linac, **kV imaging has become available on the system**. Cai et al. [6] performed an in-depth characterization of the mechanical accuracy, geometric accuracy, image quality and

dosimetry of the kV imaging system, all of which met the AAPM recommendations [7–9]. The reported acquisition time for a full-fan kV-CBCT was 3s longer than for MV-CBCT, an increase which is negligible compared with the total image acquisition and plan delivery time. On the other hand, the improved soft tissue contrast of kV-CBCT [8] may facilitate the online image-guidance process compared with MV-CBCT. Overall, the transition from MV-CBCT to kV-CBCT can be expected to maintain the time-efficiency for VMAT of HNC on the fast-rotating O-ring linac reported in chapter II of this thesis.

VI.1.3   Clinical relevance

The presented plan quality and delivery time achieved with VMAT of HNC on the fast-rotating O-ring linac should be put into clinical perspective. Firstly, although the reductions in expected toxicities compared with a C-arm linac showed statistical significance, differences actually observed in clinical practice presumably are negligible. Secondly, a reduction in image acquisition and plan delivery time of roughly one minute could be considered limited compared with reported treatment slots of 12 minutes [10–12].

Added to the reduced image acquisition and plan delivery time, however, overall workflow efficiency may be advantageous for the fast-rotating O-ring linac as well, due to an increased number of automated steps and due to the continuous readiness of the imaging devices. Resulting treatment time recordings (n=40, 7 patients) for triple-arc MV CBCT-guided VMAT of HNC on the fast-rotating O-ring linac showed a group mean of 8m50s ± 1m17s. In contrast, Kapur et al. recently reported an average time of 12.3 minutes for non-stereotactic treatments on three C-arm linacs, after a dedicated time-efficiency improvement process [11]. In addition, time recordings (n=5) of kV CBCT-guided dual-arc VMAT of HNC on a C-arm linac at the authors' institute showed a group mean of 11m12s ± 01m12s. Therefore, although a statistical comparison of a sufficient number of paired samples is lacking, a relevant reduction in treatment time for VMAT of HNC can be expected with the fast-rotating O-ring linac. The use of dual- instead of triple-arc VMAT may further reduce treatment times on the fast-rotating O-ring linac while still maintaining the plan quality of a C-arm linac. **O-ring linac technology thus enables fast, CBCT-guided, highly conformal RT of HNC, which may hold a number of clinical implications.**

VI.1.4 Potential implications

VI.1.4.1 Increased throughput of high-quality RT for HNC

RT is considered a cornerstone in the treatment of HNC. To reduce treatment-related toxicities in RT of HNC, the use of image-guided, highly conformal IMRT/VMAT has been shown crucial [13,14]. These more complex treatment approaches demand more time, however, which reflects in the lower patient numbers for all personnel categories in actual RT practice [15]. At the same time, the actual utilization of RT already is significantly lower than the optimal use, for instance due to shortage of resources. As the need for RT will continue increasing, this field of tension between quality and time-efficiency can be expected to become even more pronounced [16–18].

Reduced treatment times achieved with fast-rotating O-ring linac technology may increase clinical throughput, hereby closing the gap between demand and access to image-guided, highly conformal RT of HNC. Increasing clinical throughput, however, would require increased time-efficiency of the treatment preparation phase as well. The treatment preparation phase, namely, still consists of a large number of manual, time-consuming steps, such as target volume and OAR delineation, treatment planning and quality assurance. In this regard, the increasing application of automation in RT through artificial intelligence may provide reductions in time required for the different preparation steps as well.

Automatic delineation of high-risk clinical target volumes and OARs using convolutional neural networks (CNN), for instance, has been shown more time-efficient and more consistent than full manual delineation in RT of HNC [19,20]. Likewise, the use of automated treatment planning of VMAT for HNC using a knowledge-based approach [21,22] has demonstrated improvements in time-efficiency and consistency compared with full manual treatment planning. The workload of treatment plan quality assurance for VMAT of HNC also may be safely reduced, as a random forest classification model was validated to accurately (100% specificity) predict unacceptable plan delivery accuracy without having to actually perform the measurements [23].

The treatment preparation for VMAT of HNC thus may be performed more time-efficiently using automation, which could complement the improved time-efficiency of the treatment delivery shown in chapter II of this thesis. Successful broad application of artificial intelligence in RT, however, requires attending to a number of potential pitfalls [24]. For instance, building high-quality prediction models requires extensive, peer-reviewed and standardized datasets as input. In addition, generalizability of models cannot be assumed and model performance is to be extensively validated beyond the training data prior to deployment. Moreover, the developed models themselves require regular quality assurance [25].

VI.1.4.2 Enhanced patient comfort

Patients with HNC receiving (chemo-)RT commonly experience acute side-effects during treatment, such as mucositis, nausea, dysphagia and xerostomia [26,27]. Under these circumstances, spending less time per fraction on the treatment couch may be beneficial for the experienced patient comfort. This especially may hold true for a treatment during which the patient's head-and-neck region is immobilized during each fraction and in which the delivery of two fractions daily actually is considered the standard of care [28,29]. **In this context, reduced treatment times with fast-rotating O-ring linac technology could contribute to improved patient comfort in standard or hyper-fractionated RT of HNC.**

VI.1.4.3 Inherent availability of daily volumetric images

Anatomic deformations are a known challenge in highly-conformal RT of HNC, as the resulting differences between the delivered and the planned dose distributions may cause underdosage of the target [30−34]. Nevertheless, target coverage robustness against anatomic deformations was theoretically shown in VMAT of HNC when a 5 mm planning target volume margin was used [33]. **A margin reduction to 3 mm, on the other hand, has been shown to reduce toxicity in VMAT of HNC while maintaining locoregional control [13], but is suggested to require repeated volumetric imaging in an adaptive radiotherapy (ART) approach [13,33,35,36].** Indeed, anatomic changes resulting in loss of target coverage require to be flagged, in order to select patients for treatment plan adaptation [13,33,35]. In addition, volumetric imaging biomarkers have been identified for patient-specific

prediction of late toxicities [37,38], such that the acquired volumetric information may be used to trigger specific OAR-sparing ART. Patient-specific evaluation of the need for plan adaptation may be based on dose recalculation on repeated fan-beam CT-imaging scheduled throughout the treatment course. The optimal time point(s) for repeat CT-imaging, however, remains to be determined [39]. In addition, the absence of robust and validated criteria to select patients for plan adaptation likewise may result in unnecessary repeat CT-imaging [30,40]. Alternatively, treatment plan adaptation may be triggered based on measured weight loss, poor fit of the immobilization or anatomic changes judged significant on visual examination [39,41]. Such criteria, however, are only qualitative, which may result in false positive or false negative plan adaptation triggering [39,41].

A more time-efficient and objective ART decision-making process could be established using the daily volumetric information acquired during CBCT-guided VMAT of HNC. These CBCT's, namely, could be used for daily dose accumulation, based on which plan adaptation could be quantitatively triggered if predefined dosimetric criteria are violated [39]. Moreover, CBCT-measured image biomarkers have been shown predictive for late xerostomia [38], such that on-board volumetric imaging could also be used to identify patients eligible for specific OAR-sparing ART. An American survey report from 2014, however, stated that CBCT was acquired on a daily basis only in 55% of HNC RT fractions [42]. The fast-rotating O-ring linac studied in chapter II of this thesis, on the other hand, imposes daily imaging and the time expense to acquire volumetric imaging can be considered negligible. **Fast-rotating O-ring linac technology thus provides inherent availability of daily volumetric images, which may facilitate clinical deployment of ART of HNC.**

Exploitation of the inherent availability of daily CBCT's for ART decision-making still necessitates overcoming a number of challenges. Dose accumulation based on daily CBCT's, namely, requires the presence of the relevant contours on the CBCT, subsequent dose calculation on the CBCT, followed by warping of the contours and dose to the reference CT. In addition, these processes ideally run in an automated way in the background, allowing for easy evaluation before the next treatment fraction. Contour segmentation and dose calculation on CBCT's, however, are hampered by the inferior image quality compared with fan-beam CT, requiring for instance conversion

of the CBCT's to synthetic CT's using CNN's. In addition, dose warping from CBCT to CT is not straightforward due to the non-rigid nature of the anatomic deformations, requiring more complex deformable image registration (DIR) techniques. While proof of concepts to overcome these limitations have been presented [43–45], uncertainties and inaccuracies remain, so that manual corrections and intensive quality assurance of the techniques used for automated ART decision making currently are still needed [39,43,46–48].

Besides for dose accumulation or image biomarkers in HNC ART decision-making, daily acquired CBCT's could as well be used for the treatment plan adaptation itself. An average anatomy model can be constructed based on the daily CBCT's during a full week of treatment, for instance, to deform the initial planning CT for weekly plan adaptation [49]. A more extreme ART strategy that could be envisioned, is daily online plan adaptation[50]. Such online ART strategy holds the same challenges as daily dose accumulation, with a number of additional complexities. Besides online contouring or contour propagation and dose calculation, namely, online treatment planning is required as well. In addition, the physician is to formally correct and approve the contours and the treatment plan online. Lastly, quality assurance of the newly generated plan is to be performed online as well, prior to the delivery to the patient.

The added complexity and workload of online ART for HNC should be weighed against the potential benefits. On one hand, given the slowly progressive nature of the anatomic changes in HNC [51], less frequent treatment plan adaptations may suffice. On the other hand, in case aggressive PTV margin reduction or even elimination is pursued in VMAT of HNC [33,36], daily online ART may be a necessity to maintain target coverage. In any case, while the inherent availability of daily volumetric images offered by O-ring linac technology may facilitate ART of HNC in general, the added complexity of online ART still requires a number of technical hurdles to be taken prior to clinical deployment. In addition, potential reductions in toxicity achieved with aggressive margin reduction in combination with online ART in standard fractionated VMAT of HNC remains to be confirmed in prospective studies.

VI.1.5 Future research & development

Based on the described potential implications of fast, CBCT-guided, highly conformal RT of HNC enabled by fast-rotating O-ring linac technology, a number of future developments and improvements of the studied system can be identified:

- Utilization of the daily volumetric images for treatment monitoring using dose accumulation and image biomarkers, including subsequent ART decision-making and execution, requires associated processing and visualization software. Given the governing uncertainties of the required algorithms (DIR, CNN), the user preferably is visually informed on the dose confidence intervals for the different anatomic regions to guide the decision-making process [52,53].
- Utilization of the improved time-efficiency requires the fast-rotating O-ring linac technology to be used for RT of other indications than HNC as well. A limited number of treatment planning studies have been reported in that regard, showing plan quality equivalent to C-arm linacs for standard fractionated whole-breast and prostate RT [5,54]. Improved time-efficiency for these indications, however, remains to be confirmed.
- Effective utilization of the 4 rpm maximum rotation speed of the fast-rotating linac instead of the current restriction to 2 rpm would further improve the time-efficiency of VMAT delivery. This, however, would again require increased dose rate and leaf speed, necessitating re-design of the beam production system and the multi-leaf collimator (MLC).
- A limitation of the fast-rotating O-ring linac is that the treatment couch only allows for three instead of six degrees-of-freedom (DoF) corrections. Implementation of a 6 DoF couch would increase the possibilities for patient setup correction [55,56]. On the other hand, the necessity of patient-individualized immobilization may be more stringent to increase setup accuracy in RT of HNC [56–58], as rigid couch rotations cannot correct for the encountered non-rigid deformations.

VI.2 Optimization of proton therapy by implementing 3D printing technology

VI.2.1 Rationale

Ongoing technical improvements, such as the implementation of O-ring linac technology as previously discussed, may optimize the delivery of photon beam RT. Ultimately, however, the differential irradiation of malignant and normal tissue achievable with photons is physically limited by the governing exponential dose deposition profile. In this regard, the finite range of protons could improve target dose conformity, which may reduce toxicities compared with state-of-the-art photon beam RT while achieving the same tumor control. It is expected that increased clinical throughput and improved treatment quality could facilitate access to IMPT [59–64] and could hereby facilitate clinical evidence gathering. **In chapters III, IV and V of this thesis, 3D printing technology was implemented for the creation of a patient-specific device to improve target dose conformity and workflow efficiency in IMPT of HNC.**

VI.2.2 Specific objectives and main findings

Pre-absorbing RS is necessary for the delivery of IMPT to superficial targets, but the air gap between conventional snout-mounted RS and the patient increases the proton pencil beam size and hence the lateral penumbra. The second objective of this thesis was to quantify the dosimetric advantage of spot size minimizing, patient-specific bolus RS compared with conventional snout-mounted RS. **In chapter III of this thesis, Monte Carlo based IMPT plan optimization for five patients with HNC showed a theoretical reduction in grade 2 xerostomia and dysphagia probability by on average 3.0% and 2.7%, respectively, when bolus RS was used instead of snout-mounted RS.** As these results motivated the development of patient-specific bolus RS in IMPT of HNC, the third objective was to characterize 3D printing materials and technologies for use as bolus RS. **In chapter IV, a proof-of-concept for clinical use of 3D printed RS was presented by performing dual-energy CT-based range shift predictions and subsequent verification with proton beam measurements.** The fourth and the last objective was to show the feasibility of 3D printed immobilization, as this could allow to integrate

functionalities within the immobilization, such as integrated bolus RS to simplify IMPT workflow. **In chapter V it was shown in a patient study that 3D printed immobilization of the head region is feasible in terms of workflow, is tolerable by HNC patients during their course of RT and can achieve clinically acceptable setup accuracy for the head region.** As such, with the implementation of 3D printing technology, important steps were taken towards a single, patient-specific device that achieves spot size reduction, hardware manipulation minimization and patient immobilization for IMPT of HNC.

VI.2.3 Clinical relevance

The lateral penumbra achieved with pencil beam scanning is generally acknowledged as one of the key areas to improve IMPT treatment quality [59−64]. In this regard, the use of bolus RS (chapter III) theoretically showed reduced normal tissue irradiation in IMPT of HNC, which translated into expected reductions in normal tissue complication probabilities (NTCP). Although the used NTCP models are "photon-derived" [65], these models have been externally validated for IMPT of HNC [65] and are clinically used to cost-effectively select patients for IMPT of HNC [66]. Indeed, it has been argued that the increased cost of IMPT is only justified if a large enough benefit is expected, such as certain NTCP reductions exceeding a predefined threshold [66−68].

The consensus in the Netherlands, for instance, is to select a patient for IMPT of HNC if the expected joint grade 2 xerostomia and dysphagia probability is at least 15% lower than with photon beam RT ánd if each individual probability is at least 5% lower than with photon beam RT [69]. The average expected xerostomia and dysphagia reductions of 3.0% and 2.7%, respectively, found in chapter III, were for bolus RS IMPT compared with snout-mounted RS IMPT, nót for IMPT compared with photon beam RT. The use of bolus RS thus represents an improvement in IMPT treatment quality, in the same order of magnitude as the Dutch consensus' thresholds to decide between IMPT and photon beam RT. **As such, bolus RS could increase the overall number of patients with HNC eligible for IMPT, which shows the clinical relevance of the proposed method to optimize IMPT treatment quality.**

Besides improving IMPT treatment quality to increase the benefit with respect to photon beam RT, reducing the treatment time likewise could contribute to making IMPT more cost-effective [59–64]. In this regard, the proof-of-concept for 3D printed RS (chapter IV) and 3D printed immobilization of the head region (chapter V) provided the necessary steps towards integration of bolus RS and patient immobilization within a single device. As such, the workflow for IMPT delivery could be simplified compared with the conventional workflow using snout-mounted RS: field-per-field snout movements for air gap reduction would no longer be needed, field-per-field presence and correct placement of RS would be automatically ensured and potential collisions between the RS and the couch would no longer be an issue. **The elements provided towards RS-integrated patient immobilization using 3D printing technology, thus, could offer improvements in treatment time for IMPT of HNC.** Effective integration of the RS and immobilization functionality, including clinical implementation, is yet to be achieved, however. In the meantime, any potential reduction in treatment time likewise remains to be confirmed.

VI.2.4 Related studies

The potential benefits of RS-integrated patient immobilization for IMPT of HNC should be weighed against alternative developments. Improved treatment quality by lateral penumbra reduction, namely, is being pursued with other techniques as well. It would be interesting to reflect on the applicability of each of these techniques for IMPT of locally-advanced HNC (LAHNC) and on the advantages and disadvantages of each technique compared with the proposed RS-integrated patient immobilization.

A first alternative approach for penumbra reduction in IMPT is collimation, which could be achieved with a custom aperture [70–72]. Aperture-based collimation, however, provides optimal collimation only for the energy layer with the largest cross-sectional size of the target in the beam's eye view. The spots at the target edge in other energy layers are either sub-optimally collimated or not collimated at all [73]. A more flexible, layer-specific collimation could be achieved with an MLC [74,75] or with a dynamic collimation system (DCS) consisting of two orthogonal pair of trimmer blades [73,76]. While the dosimetric advantage of DCS has been theoretically shown for IMPT of brain tumors [76,77], the proposed design only allows for a maximum field size of

15 x 15 cm², which generally is not sufficient for IMPT of LAHNC. Moreover, air gap reduction for the superficial layers delivered with RS remains important [72,76], which would still be problematic in case a larger field size could be obtained.

A second alternative approach for penumbra reduction is the so-called 'automated RS' [78,79]. In this technique, the nozzle- or snout mounted RS is automatically removed when it is not needed, i.e. for the delivery of spot layers at a greater range than the minimally deliverable range. As such, the spot size degradation due to the combination RS/air gap is avoided for the deeper delivered spots. Automated RS effectively has been reported as clinically used for cranio-spinal, intra-cranial and abdominal IMPT [78–80]. This 'automatic RS' approach is not possible with an RS-integrated patient immobilization, which represents a limitation of the solution proposed in this thesis. On the other hand, even with 'automatic RS, the amplifying effect of the air gap on the RS spot size degradation would still be present for the shallow layers of IMPT of HNC. In addition, the use of 'automatic RS' needs to be supported by the treatment planning system, which is not trivial [78]. Moreover, the complexity added to the delivery has been reported to moderately increase treatment time [80]. Nevertheless, it would be interesting to compare the differences in NTCP obtained with automated RS and with RS-integrated patient immobilization in IMPT of HNC.

A third alternative approach for penumbra reduction in IMPT is edge-enhancing optimization, in which the spots in a layer are positioned on a pattern following the target contour instead of a traditional rectangular grid [72,77]. During treatment plan optimization, the lateral spots are then preferentially weighted such that the lateral field penumbra approaches that of a single spot, i.e. the smallest possible. The benefit of combining edge-enhancing optimization with collimation, as opposed to the individual use of each technique, has been theoretically shown in a water phantom study and for a selection of intra-cranial IMPT plans [72,77]. Based on the results presented for the water phantom study [72], it may be hypothesized that edge-enhanced optimization likewise could be complementary to the use of bolus RS, which warrants further study.

VI.2.5 Clinical implementation

With the theoretical demonstration of clinically relevant NTCP reductions using bolus RS (chapter III), the proof-of-concept of 3D printed materials used as RS in a clinical workflow (chapter IV) and the feasibility of 3D printed immobilization of the head shown on patients (chapter V), necessary steps were taken towards RT-integrated patient immobilization for IMPT of HNC. In order to effectively achieve the associated potential benefits, however, the proposed device is to be clinically implemented and clinically used. To this end, a number of subsequent steps are yet to be carried out.

Firstly, while 3D printed immobilization achieved clinically acceptable setup accuracy for the head region, excessive positional variations of the studied sub-regions-of-interest in the neck region were observed (chapter V). This finding was expected, given the absence of immobilization of the lower neck and shoulders with the studied 3D printed assembly. The 3D printed immobilization therefore requires caudal extension in order to serve as a valid immobilization option for IMPT of patients with HNC. Such extension likewise is necessary to provide clinically relevant bolus integration options, since IMPT of HNC commonly involves superficial irradiation of the lower neck levels with anterior oblique fields [81–85]. Successful immobilization of the lower neck and shoulder using a caudally extended 3D printed assembly remains to be shown in future work.

Secondly, a commercially available treatment couch overlay, dedicated for immobilization of the head, was preliminarily used to show the feasibility of 3D printed immobilization (chapter V). 3D printed immobilization extended to the neck and shoulders area, however, is likely not attachable to the used treatment couch overlay. In addition, the used treatment couch overlay presents geometrical and stopping power related gradients perpendicular to the proton beam directions, which are to be avoided in IMPT [86–88]. Further development of 3D printed immobilization for IMPT of HNC, therefore, would require adaptation of the current design to be attachable to a suitable treatment couch overlay or insert. A commercially available BoS™ insert (QFix, Avondale, PA), for instance, is already dosimetrically optimized for clinical use in IMPT of HNC [88,89] and facilitates the attachment of immobilization material over a large cranio-caudal extent. Given that it was already shown feasible to

customize a 3D printed immobilization assembly such that it attached to a selected treatment couch overlay (chapter V), feasibility of attachment to a BoS™ insert likewise can be assumed.

Thirdly, the range of protons is very sensitive to the thickness and the stopping power of the traversed material. The use of patient-specific, 3D printed bolus RS thus requires accurate knowledge of the geometric and range shifting properties of the selected 3D printed material and technique prior to clinical use. In this regard, the orientation dependency of the range shift as observed for instance for ABS (chapter IV), created with fused deposition modeling (FDM), cannot be easily anticipated and therefore presumably renders this material or even this printing technique unusable for use as bolus RS. Two other, independent studies likewise advised against the use of FDM to create proton beam modification devices, due to geometric dependency [90] and internal inhomogeneities [91]. While FDM was the 3D printing technique used for the feasibility study of 3D printed immobilization (chapter V), Tusk material created with stereolithography would be a viable alternative for effective clinical use (chapter IV): no orientation dependency of the RS was observed and large enough build volumes to create an extended 3D printed immobilization assembly are possible.

Fourthly, the feasibility study of 3D printed immobilization (chapter V) involved a labor-intensive design process, which may not be justified in clinical use of 3D printed immobilization on a routine basis. The used software, however, does allow to design patient-specific devices based only on a number of landmarks input by the user to define the intended geometry. Such semi-automation may improve the time-efficiency of the design process and could facilitate clinical introduction of 3D printed immobilization. In any case, the range shifting effect of the designed immobilization is to be taken into account during treatment planning. This can be achieved by converting the .STL-file of the designed immobilization to a DICOM RT structure and subsequent importing in the TPS. The dimensions of the to be integrated bolus RS, however, are to be defined during treatment planning itself, in function of the patient-specific target volume and the used beam angles. Therefore, the design of the RS-integrated immobilization ideally occurs in the TPS, simultaneously with the treatment planning. Commercially available TPS currently provide such functionality for patient-specific design of IMPT apertures, but not for RS-integrated patient immobilization.

Fifthly, RS-integrated patient immobilization for IMPT of HNC requires thorough commissioning prior to clinical use, like any conventional immobilization or RS device [86]. Hereto, for the candidate 3D printed material (Tusk) and technique (stereolithography), extensive range shift measurements should be performed for various geometries and orientations with respect to the proton beam, to exclude any geometric and orientation dependency of the range shift. In addition, any measured range shift should correspond with the TPS-predicted range shift. In this regard, the measured range shift for Tusk, created with stereolithography, deviated more than 1 mm or 5 % from the dual-energy CT based range shift prediction (chapter IV). In clinical practice this could be corrected for, however, by overriding the RS material properties in the TPS during commissioning such that correspondence between prediction and measurement is achieved [86]. In any case, the commissioning process is preferably concluded with an end-to-end verification test with multiple detector measurements in an anthropomorphic phantom, immobilized with a 3D printed, RS-integrated device. During routine clinical use, quality assurance of each newly created patient-specific device could be performed with a pre-treatment CT-scan, by verifying correspondence of the Hounsfield units with those of the 3D printed device used for commissioning.

VI.2.6 Future research & development

Besides clinical implementation of RS-integrated patient immobilization for IMPT of HNC, a number of research questions currently remain open:

- The future use of RS-integrated patient immobilization would have an impact on the general clinical workflow for RT of HNC in case a model-based approach is used [68]. In this approach, namely, it is not yet known whether a patient will receive photon beam RT or IMPT, at the moment the planning CT is acquired. The proposed methodology to create RS-integrated patient immobilization for IMPT of HNC, however, assumes the planning CT being acquired without a thermoplastics mask on the patient (chapter V). Acquisition of a mask-less planning CT in a model-based approach, consequentially, would imply consistent use of 3D printed immobilization, which would unnecessarily add cost and workload to a photon beam RT treatment of HNC. On the other hand, 3D printed immobilization could show benefits for photon beam RT of HNC as well. Specifically, 3D printed immobilization

may be better able to approximate the patient's body outline than a thermoplastic mask, which could reduce inter-fractional setup variations.

While this could allow for reduced margins/robustness settings in both photon beam RT and IMPT of HNC, reduced setup variations with 3D printed immobilization could not be conclusively shown in this thesis. Therefore, the pilot feasibility study of 3D printed immobilization on patients (chapter V) could be elaborated in further study, with a larger patient sample size and with an improved immobilization design and setup procedure. Potential improvements compared with the methodology used in chapter V could be:

- o Optimization of the threshold value used for the body segmentation, as to obtain a tighter fit of the 3D printed immobilization around the patient
- o Further enclosing the 3D printed immobilization assembly around the patient, for instance at the level of the upper lip, the nose bridge and the temporal bone
- o Use of optical surface scanning to guide the patient positioning prior to applying the anterior 3D printed shell

- Owing to the distinct dose deposition profile of protons, the sensitivity of the dose distribution to anatomic changes presumably is even more pronounced in IMPT than in photon beam RT of HNC [81,82,84,92,93]. The previous comments on ART of HNC with a fast-rotating O-ring linac, therefore, all the more apply to IMPT of HNC. As the availability of in-room volumetric imaging in IMPT has been lagging significantly behind photon beam RT [59], anatomic changes currently are often assessed based on weekly out-of-room verification CT scans [81,92]. This situation is rapidly changing, however, since in-room CT- or CBCT-imaging is becoming more common [59]. Like in photon beam RT of HNC, the feasibility of both online [93] and offline [94] plan adaptation based on on-board CBCT-images already has been reported for IMPT of HNC. Therefore, increased patient-individual treatment delivery monitoring and plan adaptation, based on daily volumetric imaging, likewise could be expected in IMPT of HNC.

The occurrence of anatomic changes, however, can not only compromise the dose delivered dose distribution but also the immobilization quality in RT of HNC [51]. Loss of immobilization may be corrected for, which however requires additional

labor-intensive and online workflow steps. The flexibility on object shaping of 3D printing technology compared with conventional thermoplastic masks may be used to increase the robustness of immobilization against anatomic changes. A 3D printed design could allow to mainly immobilize on regions with high anatomical stability, such as bony structures surrounded by few soft tissue. The hypothesis of increased robustness of immobilization against anatomic changes, however, remains to be shown in further study.

VI.3 Other developments in radiotherapy of head-and-neck cancer

The efforts presented in this thesis to improve RT of HNC, by the optimization and the implementation of emerging technologies, are accompanied by many other ongoing developments. For instance, the favorable prognosis of human papillomavirus positive HNC has led to the exploration of **treatment de-intensification strategies,** in order to reduce toxicities while maintaining treatment control for this sub-population of patients [95]. Attempts to increase tumor control in HNC subtypes with a less favorable prognosis include **local dose escalation based on multi-modal imaging** such as positron emission tomography with ^{18}F-deoxyglucose, dynamic contrast-enhanced magnetic resonance imaging (MRI) and diffusion-weighted MRI [96,97]. The combined use of RT and **molecular-targeting agents** is increasingly investigated in the treatment of HNC [98], also in ultra-hypofractionated salvage RT of recurrent HNC [99]. To conclude this non-exhaustive listing of actual research topics in RT of HNC, the suggested **increased normal tissue sparing of RT at ultra-high dose rate** (> 40 Gy/s) is promising but still requires solid evidence, clinical translation and technological advances [100,101].

References

[1]   Kamino Y, Takayama K, Kokubo M, Narita Y, Hirai E, Kawawda N, et al. Development of a four-dimensional image-guided radiotherapy system with a gimbaled X-ray head. Int J Radiat Oncol Biol Phys 2006;66:271–8.

[2]   Raaymakers BW, Lagendijk JJW, Overweg J, Kok JGM, Raaijmakers AJE, Kerkhof EM, et al. Integrating a 1.5 T MRI scanner with a 6 MV accelerator: Proof of concept. Phys Med Biol 2009;54:N229.

[3]   De Roover R, Crijns W, Poels K, Michiels S, Nulens A, Vanstraelen B, et al. Validation and IMRT/VMAT delivery quality of a preconfigured fast-rotating O-ring linac system. Med Phys 2019;46:328–39.

[4]   Lyu Q, Neph R, Yu VY, Ruan D, Sheng K. Single-arc VMAT optimization for dual-layer MLC. Phys Med Biol 2019;64:095028.

[5]   Cozzi L, Fogliata A, Thompson S, Franzese C, Franceschini D, de Rose F, et al. Critical appraisal of the treatment planning performance of volumetric modulated arc therapy by means of a dual layer stacked multileaf collimator for head and neck, breast, and prostate. Technol Cancer Res Treat 2018;17:1–11.

[6]   Cai B, Laugeman E, Mazur TR, Park JC, Henke LE, Kim H, et al. Characterization of a prototype rapid kilovoltage x-ray image guidance system designed for a ring shape radiation therapy unit. Med Phys 2019;46:1355–70.

[7]   Klein EE, Hanley J, Bayouth J, Yin FF, Simon W, Dresser S, et al. Task group 142 report: Quality assurance of medical accelerators. Med Phys 2009;36:4197–212.

[8]   Bissonnette J-P, Balter PA, Dong L, Langen KM, Lovelock DM, Miften M, et al. Quality assurance for image-guided radiation therapy utilizing CT-based technologies: a report of the AAPM TG-179. Med Phys 2012;39:1946–63.

[9]   Langen KM, Papanikolaou N, Balog J, Crilly R, Followill D, Goddu SM, et al. QA for helical tomotherapy: Report of the AAPM Task Group 148. Med Phys 2010;37:4817–53.

[10]   Bertelsen A, Hansen CR, Johansen J, Brink C. Single Arc Volumetric Modulated Arc Therapy of head and neck cancer. Radiother Oncol 2010;95:142–8.

[11]   Kapur A, Adair N, O'Brien M, Naparstek N, Cangelosi T, Zuvic P, et al. Improving efficiency and safety in external beam radiation therapy treatment delivery using a Kaizen approach. Pract Radiat Oncol 2017;7:e499–506.

[12]   Van Dyk J, Zubizarreta E, Lievens Y. Cost evaluation to optimise radiation therapy implementation in different income settings : A time-driven activity-based analysis. Radiother Oncol 2017;125:178–85.

[13]   Navran A, Heemsbergen W, Janssen T, Hamming-Vrieze O, Jonker M, Zuur C, et al. The impact of margin reduction on outcome and toxicity in head and neck cancer patients treated with image-guided volumetric modulated arc therapy (VMAT). Radiother Oncol

2019;130:25–31.

[14] Nutting CM, Morden JP, Harrington KJ, Urbano TG, Bhide SA, Clark C, et al. Parotid-sparing intensity modulated versus conventional radiotherapy in head and neck cancer (PARSPORT): A phase 3 multicentre randomised controlled trial. Lancet Oncol 2011;12:127–36.

[15] Lievens Y, Defourny N, Coffey M, Borras JM, Dunscombe P, Slotman B, et al. Radiotherapy staffing in the European countries : Final results from the ESTRO-HERO survey 2014;112:178–86.

[16] Grau C, Defourny N, Malicki J, Dunscombe P, Borras JM, Coffey M, et al. Radiotherapy equipment and departments in the European countries : Final results from the ESTRO-HERO survey 2014;112:155–64.

[17] Borras JM, Lievens Y, Dunscombe P, Coffey M, Malicki J, Corral J, et al. The optimal utilization proportion of external beam radiotherapy in European countries : An ESTRO-HERO analysis. Radiother Oncol 2015;116:38–44.

[18] Borras JM, Grau C, Corral J, Wong K, Barton MB, Ferlay J, et al. Estimating the number of fractions by tumour site for European countries in 2012 and 2025: An ESTRO-HERO analysis. Radiother Oncol 2017;126:198–204.

[19] Cardenas CE, McCarroll RE, Court LE, Elgohari BA, Elhalawani H, Fuller CD, et al. Deep Learning Algorithm for Auto-Delineation of High-Risk Oropharyngeal Clinical Target Volumes With Built-In Dice Similarity Coefficient Parameter Optimization Function. Int J Radiat Oncol Biol Phys 2018;101:468–78.

[20] van der Veen J, Willems S, Deschuymer S, Robben D, Crijns W, Maes F, et al. Benefits of deep learning for delineation of organs at risk in head and neck cancer. Radiother Oncol 2019;138:68–74.

[21] Tol JP, Delaney AR, Dahele M, Slotman BJ, Verbakel WFAR. Evaluation of a knowledge-based planning solution for head and neck cancer. Int J Radiat Oncol Biol Phys 2015;91:612–20.

[22] Krayenbuehl J, Norton I, Studer G, Guckenberger M. Evaluation of an automated knowledge based treatment planning system for head and neck. Radiat Oncol 2015;10:226.

[23] Li J, Wang L, Zhang X, Liu L, Li J, Chan MF, et al. Machine Learning for Patient-Specific Quality Assurance of VMAT: Prediction and Classification Accuracy. Int J Radiat Oncol Biol Phys 2019.

[24] Thompson RF, Valdes G, Fuller CD, Carpenter CM, Morin O, Aneja S, et al. Artificial intelligence in radiation oncology: A specialty-wide disruptive transformation? Radiother Oncol 2018;129:421–6.

[25] El Naqa I, Ruan D, Valdes G, Dekker A, McNutt T, Ge Y, et al. Machine learning and

modeling: Data, validation, communication challenges. Med Phys 2018;45:e834–40.

[26]   Siddiqui F, Movsas B. Management of Radiation Toxicity in Head and Neck Cancers. Semin Radiat Oncol 2017;27:340–9.

[27]   Givens DJ, Lucy B;, Karnell H, Gupta AK, Clamon GH, Pagedar NA, et al. Adverse Events Associated With Concurrent Chemoradiation Therapy in Patients With Head and Neck Cancer. Arch Otolaryngol Head Neck Surg 2009;135:1209–17.

[28]   Lacas B, Bourhis J, Overgaard J, Zhang Q, Grégoire V, Nankivell M, et al. Role of radiotherapy fractionation in head and neck cancers (MARCH): an updated meta-analysis. Lancet Oncol 2017;18:1221–37.

[29]   Nuyts S. The true value of altered fractionation in head and neck cancer. Lancet Oncol 2017;18:1147–8.

[30]   Brouwer CL, Steenbakkers RJHM, Langendijk JA, Sijtsema NM. Identifying patients who may benefit from adaptive radiotherapy: Does the literature on anatomic and dosimetric changes in head and neck organs at risk during radiotherapy provide information to help? Radiother Oncol 2015;115:285–94.

[31]   Hong TS, Tomé WA, Chappell RJ, Chinnaiyan P, Mehta MP, Harari PM. The impact of daily setup variations on head-and-neck intensity-modulated radiation therapy. Int J Radiat Oncol Biol Phys 2005;61:779–88.

[32]   Brouwer CL, Steenbakkers RJHM, van der Schaaf A, Sopacua CTC, van Dijk L V., Kierkels RGJ, et al. Selection of head and neck cancer patients for adaptive radiotherapy to decrease xerostomia. Radiother Oncol 2016;120:36–40.

[33]   van Kranen S, Hamming-Vrieze O, Wolf A, Damen E, van Herk M, Sonke JJ. Head and Neck Margin Reduction With Adaptive Radiation Therapy: Robustness of Treatment Plans Against Anatomy Changes. Int J Radiat Oncol Biol Phys 2016;96:653–60.

[34]   Schwartz DL, Garden AS, Thomas J, Chen Y, Zhang Y, Lewin J, et al. Adaptive Radiotherapy for Head-and-Neck Cancer: Initial Clinical Outcomes from a Prospective Trial. Int J Radiat Oncol Biol Phys 2012;83:986–93.

[35]   Chen AM, Daly ME, Cui J, Mathai M, Benedict S, Purdy JA. Clinical outcomes among patients with head and neck cancer treated by intensity-modulated radiotherapy with and without adaptive replanning. Head Neck 2014;36:1541–6.

[36]   Samuels SE, Eisbruch A, Vineberg K, Lee J, Lee C, Matuszak MM, et al. Methods for Reducing Normal Tissue Complication Probabilities in Oropharyngeal Cancer: Dose Reduction or Planning Target Volume Elimination. Int J Radiat Oncol Biol Phys 2016;96:645–52.

[37]   van Dijk L V., Brouwer CL, van der Laan HP, Burgerhof JGM, Langendijk JA, Steenbakkers RJHM, et al. Geometric Image Biomarker Changes of the Parotid Gland Are Associated With Late Xerostomia. Int J Radiat Oncol Biol Phys 2017;99:1101–10.

[38] Rosen BS, Hawkins PG, Polan DF, Balter JM, Brock KK, Kamp JD, et al. Early Changes in Serial CBCT-Measured Parotid Gland Biomarkers Predict Chronic Xerostomia After Head and Neck Radiation Therapy. Int J Radiat Oncol Biol Phys 2018;102:1319–29.

[39] Sonke JJ, Aznar M, Rasch C. Adaptive Radiotherapy for Anatomical Changes. Semin Radiat Oncol 2019;29:245–57.

[40] Castelli J, Simon A, Lafond C, Perichon N, Rigaud B, Chajon E, et al. Adaptive radiotherapy for head and neck cancer. Acta Oncol (Madr) 2018;57:1284–92.

[41] Heukelom J, Fuller CD. Head and Neck Cancer Adaptive Radiation Therapy (ART): Conceptual Considerations for the Informed Clinician. Semin Radiat Oncol 2019;29:258–73.

[42] Nabavizadeh N, Elliott DA, Chen Y, Kusano AS, Mitin T, Thomas CR, et al. Image Guided Radiation Therapy (IGRT) practice patterns and IGRT's impact on workflow and treatment planning: Results from a national survey of american society for radiation oncology members. Int J Radiat Oncol Biol Phys 2016;94:850–7.

[43] Peroni M, Ciardo D, Spadea MF, Riboldi M, Comi S, Alterio D, et al. Automatic segmentation and online virtualCT in head-and-neck adaptive radiation therapy. Int J Radiat Oncol Biol Phys 2012;84:e427-33.

[44] Liang X, Chen L, Nguyen D, Zhou Z, Gu X, Yang M, et al. Generating Synthesized Computed Tomography (CT) from Cone-Beam Computed Tomography (CBCT) using CycleGAN for Adaptive Radiation Therapy. Phys Med Biol 2019;64:125002 (13pp).

[45] Veiga C, McClelland J, Moinuddin S, Lourenço A, Ricketts K, Annkah J, et al. Toward adaptive radiotherapy for head and neck patients: Feasibility study on using CT-to-CBCT deformable registration for "dose of the day" calculations. Med Phys 2014;41:0317031–12.

[46] Chetty IJ, Fontenot J. Adaptive Radiation Therapy: Off-Line, On-Line, and In-Line? Int J Radiat Oncol 2017;99:689–91.

[47] Chetty IJ, Rosu-Bubulac M. Deformable Registration for Dose Accumulation. Semin Radiat Oncol 2019;29:198–208.

[48] Mencarelli A, Van Kranen SR, Hamming-Vrieze O, Van Beek S, Nico Rasch CR, Van Herk M, et al. Deformable image registration for adaptive radiation therapy of head and neck cancer: Accuracy and precision in the presence of tumor changes. Int J Radiat Oncol Biol Phys 2014;90:680–7.

[49] Van Kranen S, Mencarelli A, Van Beek S, Rasch C, Van Herk M, Sonke JJ. Adaptive radiotherapy with an average anatomy model: Evaluation and quantification of residual deformations in head and neck cancer patients. Radiother Oncol 2013;109:463–8.

[50] Lim-Reinders S, Keller BM, Al-ward S, Kim A. Online Adaptive Radiation Therapy. Int J Radiat Oncol Biol Phys 2017;99:994–1003.

[51] Barker JL, Garden AS, Ang KK, O'Daniel JC, Wang H, Court LE, et al. Quantification of volumetric and geometric changes occurring during fractionated radiotherapy for head-and-neck cancer using an integrated CT/linear accelerator system. Int J Radiat Oncol Biol Phys 2004;59:960–70.

[52] Nassef M, Simon A, Cazoulat G, Duménil A, Blay C, Lafond C, et al. Quantification of dose uncertainties in cumulated dose estimation compared to planned dose in prostate IMRT. Radiother Oncol 2016;119:129–36.

[53] Bohoudi O, Lagerwaard FJ, Bruynzeel AME, Niebuhr NI, Johnen W, Senan S, et al. End-to-end empirical validation of dose accumulation in MRI-guided adaptive radiotherapy for prostate cancer using an anthropomorphic deformable pelvis phantom. Radiother Oncol 2019;141:200–7.

[54] Kennedy C, Freedman G, Taunk N, Scheuermann R, Dong L, Metz J, et al. Whole Breast Irradiation with Halcyon™ 2.0: Workflow and Efficiency of Field-in-Field Treatment with Dynamic Beam Flattening Technique and kV Cone Beam Computed Tomography. Cureus 2018;10:e3510.

[55] Rodrigues MF, Veen S, van Egmond J, van Hameren M, van Oorschot T, de Vet S, et al. The influence of a six degrees of freedom couch and an individual head support in patient positioning in radiotherapy of head and neck cancer. Phys Imaging Radiat Oncol 2019;11:30–3.

[56] Njeh CF, Snyder KC, Cai J. The use of six degrees of freedom couch is only clinically beneficial in stereotactic radio surgery. Med Phys 2019;46:415–8.

[57] Li H, Zhu XR, Zhang L, Dong L, Tung S, Ahamad A, et al. Comparison of 2D Radiographic Images and 3D Cone Beam Computed Tomography for Positioning Head-and-Neck Radiotherapy Patients. Int J Radiat Oncol Biol Phys 2008;71:916–25.

[58] Houweling AC, van der Meer S, van der Wal E, Terhaard CHJ, Raaijmakers CPJ. Improved immobilization using an individual head support in head and neck cancer patients. Radiother Oncol 2010;96:100–3.

[59] Lomax A. What will the medical physics of proton therapy look like 10 yr from now? A personal view. Med Phys 2018;45:e984–93.

[60] Farr JB, Flanz JB, Gerbershagen A, Moyers MF. New horizons in particle therapy systems. Med Phys 2018;45:e953–83.

[61] Mohan R, Das IJ, Ling C. Empowering Intensity Modulated Proton Therapy Through Physics and Technology: An Overview. Int J Radiat Oncol Biol Phys 2017;99:304–16.

[62] Engelsman M, Schwarz M, Dong L. Physics Controversies in Proton Therapy. Semin Radiat Oncol 2013;23:88–96.

[63] Flanz J, Bortfeld T. Evolution of technology to optimize the delivery of proton therapy: The third generation. Semin Radiat Oncol 2013;23:142–8.

[64] Lievens Y, Pijls-Johannesma M. Health economic controversy and cost-effectiveness of proton therapy. Semin Radiat Oncol 2013;23:134–41.

[65] Blanchard P, Wong AJ, Gunn GB, Garden AS, Mohamed ASR, Rosenthal DI, et al. Toward a model-based patient selection strategy for proton therapy: External validation of photon-derived normal tissue complication probability models in a head and neck proton therapy cohort. Radiother Oncol 2016;121:381–6.

[66] Langendijk JA, Boersma LJ, Rasch CRN, van Vulpen M, Reitsma JB, van der Schaaf A, et al. Clinical Trial Strategies to Compare Protons With Photons. Semin Radiat Oncol 2018;28:79–87.

[67] Widder J, van der Schaaf A, Lambin P, Marijnen CAM, Pignol JP, Rasch CR, et al. The Quest for Evidence for Proton Therapy: Model-Based Approach and Precision Medicine. Int J Radiat Oncol Biol Phys 2016;95:30–6.

[68] Langendijk JA, Lambin P, De Ruysscher D, Widder J, Bos M, Verheij M. Selection of patients for radiotherapy with protons aiming at reduction of side effects: The model-based approach. Radiother Oncol 2013;107:267–73.

[69] Kanayama N, Kierkels RGJ, van der Schaaf A, Steenbakkers RJHM, Yoshioka Y, Nishiyama K, et al. External validation of a multifactorial normal tissue complication probability model for tube feeding dependence at 6 months after definitive radiotherapy for head and neck cancer. Radiother Oncol 2018;129:403–8.

[70] Moteabbed M, Yock TI, Depauw N, Madden TM, Kooy HM, Paganetti H. Impact of Spot Size and Beam-Shaping Devices on the Treatment Plan Quality for Pencil Beam Scanning Proton Therapy. Int J Radiat Oncol Biol Phys 2016;95:190–8.

[71] Bäumer C, Janson M, Timmermann B, Wulff J. Collimated proton pencil-beam scanning for superficial targets : impact of the order of range shifter and aperture Collimated proton pencil-beam scanning for superficial targets : impact of the order of range shifter and aperture. Phys Med Biol 2018;63:085020.

[72] Winterhalter C, Lomax A, Oxley D, Weber DC, Safai S. A study of lateral fall-off (penumbra) optimisation for pencil beam scanning (PBS) proton therapy. Phys Med Biol 2018;63:025022.

[73] Hyer DE, Hill PM, Wang D, Smith BR, Flynn RT. A dynamic collimation system for penumbra reduction in spot-scanning proton therapy: Proof of concept. Med Phys 2014;41:0917011–9.

[74] Daartz J, Bangert M, Bussìre MR, Engelsman M, Kooy HM. Characterization of a mini-multileaf collimator in a proton beamline. Med Phys 2009;36:1886–94.

[75] Winterhalter C, Meier G, Oxley D, Weber DC, Lomax AJ, Safai S. Contour scanning , multi-leaf collimation and the combination thereof for proton pencil beam scanning Contour scanning , multi-leaf collimation and the combination thereof for proton pencil

beam scanning. Phys Med Biol 2019;64:015002.

[76]   Moignier A, Gelover E, Wang D, Smith B, Flynn R, Kirk M, et al. Theoretical Benefits of Dynamic Collimation in Pencil Beam Scanning Proton Therapy for Brain Tumors: Dosimetric and Radiobiological Metrics. Int J Radiat Oncol Biol Phys 2016;95:171–80.

[77]   Winterhalter C, Meier G, Oxley D, Weber DC, Lomax AJ, Safai S. Contour scanning, multi-leaf collimation and the combination thereof for proton pencil beam scanning. Phys Med Biol 2019;64:015002.

[78]   Farace P, Bizzocchi N, Righetto R, Fellin F, Fracchiolla F, Lorentini S, et al. Supine craniospinal irradiation in pediatric patients by proton pencil beam scanning. Radiother Oncol 2017;123:112–8.

[79]   Lomax A. What will the medical physics of proton therapy look like 10 yr from now? A personal view. Med Phys 2018;45:e984–93.

[80]   Fracchiolla F, Fellin F, Innocenzi M, Lipparini M, Lorentini S, Widesott L, et al. A pre-absorber optimization technique for pencil beam scanning proton therapy treatments. Phys Medica 2019;57:145–52.

[81]   Cubillos-Mesías M, Troost EGC, Lohaus F, Agolli L, Rehm M, Richter C, et al. Including anatomical variations in robust optimization for head and neck proton therapy can reduce the need of adaptation. Radiother Oncol 2019;131:127–34.

[82]   Hamming-Vrieze O, Depauw N, Craft DL, Chan AW, Rasch CRN, Verheij M, et al. Impact of setup and range uncertainties on TCP and NTCP following VMAT or IMPT of oropharyngeal cancer patients. Phys Med Biol 2019;64:095001.

[83]   Frank SJ, Cox JD, Gillin M, Mohan R, Garden AS, Rosenthal DI, et al. Multifield optimization intensity modulated proton therapy for head and neck tumors: A translation to practice. Int J Radiat Oncol Biol Phys 2014;89:846–53.

[84]   Kraan AC, Van De Water S, Teguh DN, Al-Mamgani A, Madden T, Kooy HM, et al. Dose uncertainties in IMPT for oropharyngeal cancer in the presence of anatomical, range, and setup errors. Int J Radiat Oncol Biol Phys 2013;87:888–96.

[85]   Michiels S, Barragán AM, Souris K, Poels K, Crijns W, Lee JA, et al. Patient-specific bolus for range shifter air gap reduction in intensity- modulated proton therapy of head-and-neck cancer studied with Monte Carlo based plan optimization. Radiother Oncol 2018;128:161–6.

[86]   Olch AJ, Gerig L, Li H, Mihaylov I, Morgan A. Dosimetric effects caused by couch tops and immobilization devices: report of AAPM Task Group 176. Med Phys 2014;41:061501.

[87]   Wroe AJ, Bush DA, Slater JD. Immobilization Considerations for Proton Radiation Therapy. Technol Cancer Res Treat 2013;13:217–26.

[88]   Wroe AJ, Ghebremedhin A, Gordon IR, Schulte SRW, Slater JD. Water Equivalent

Thickness Analysis of Immobilization Devices for Clinical Implementation in Proton Therapy. TCRT Express 2013;1:83–8.

[89] Wroe AJ, Bush DA, Schulte RW, Slater JD. Clinical Immobilization Techniques for Proton Therapy. Technol Cancer Res Treat 2013;14:71–9.

[90] Lindsay C, Kumlin J, Jirasek A, Lee R, Martinez DM, Schaffer P, et al. 3D printed plastics for beam modulation in proton therapy. Phys Med Biol 2015;60:N231–40.

[91] Zou W, Fisher T, Zhang M, Kim L, Chen T, Narra V, et al. Potential of 3D printing technologies for fabrication of electron bolus and proton compensators. J Appl Clin Med Phys 2015;16:90–8.

[92] Yang Z, Zhang X, Wang X, Zhu XR, Gunn B, Frank SJ, et al. Multiple-CT optimization: An adaptive optimization method to account for anatomical changes in intensity-modulated proton therapy for head and neck cancers. Radiother Oncol 2019:Article in press.

[93] Botas P, Kim J, Winey B, Paganetti H. Online adaption approaches for intensity modulated proton therapy for head and neck patients based on cone beam CTs and Monte Carlo simulations. Phys Med Biol 2019;64:015004.

[94] Kurz C, Nijhuis R, Reiner M, Ganswindt U, Thieke C, Belka C, et al. Feasibility of automated proton therapy plan adaptation for head and neck tumors using cone beam CT images. Radiat Oncol 2016;11:1–9.

[95] Chera BS, Amdur RJ. Current Status and Future Directions of Treatment Deintensification in Human Papilloma Virus-associated Oropharyngeal Squamous Cell Carcinoma. Semin Radiat Oncol 2018;28:27–34.

[96] Berwouts D, Madani I, Duprez F, Olteanu AML, Vercauteren T, Boterberg T, et al. Long-term outcome of 18F-fluorodeoxyglucose-positron emission tomography-guided dose painting for head and neck cancer: Matched case-control study. Head Neck 2017;39:2264–75.

[97] Teng F, Aryal M, Lee J, Lee C, Shen X, Hawkins PG, et al. Adaptive Boost Target Definition in High-Risk Head and Neck Cancer Based on Multi-imaging Risk Biomarkers. Int J Radiat Oncol Biol Phys 2018;102:969–77.

[98] Cho J, Johnson DE, Grandis JR. Therapeutic Implications of the Genetic Landscape of Head and Neck Cancer. Semin Radiat Oncol 2018;28:2–11.

[99] Vargo JA, Ferris RL, Ohr J, Clump DA, Davis KS, Duvvuri U, et al. A prospective phase 2 trial of reirradiation with stereotactic body radiation therapy plus cetuximab in patients with previously irradiated recurrent squamous cell carcinoma of the head and neck. Int J Radiat Oncol Biol Phys 2015;91:480–8.

[100] Maxim PG, Keall P, Cai J. FLASH radiotherapy: Newsflash or flash in the pan? Med Phys 2019;46:4287–90.

[101] Bourhis J, Montay-Gruel P, Gonçalves Jorge P, Bailat C, Petit B, Ollivier J, et al. Clinical translation of FLASH radiotherapy: Why and how? Radiother Oncol 2019;139:11–7.

Personal contribution & Conflicts of interest

Personal contribution

- **Chapter 1: Introduction**
  Steven Michiels, Kenneth Poels, Sandra Nuyts, Tom Depuydt

  SM wrote the chapter (with valuable input and comments of the co-authors).

- **Chapter 2: Volumetric modulated arc therapy of head-and-neck cancer on a fast-rotating O-ring linac: Plan quality and delivery time comparison with a C-arm linac**
  Steven Michiels, Kenneth Poels, Wouter Crijns, Laurence Delombaerde, Robin De Roover, Bianca Vanstraelen, Karin Haustermans, Sandra Nuyts, Tom Depuydt

  SM co-defined the study methodology, created the treatment plans, co-performed the quality assurance measurements of the treatment plans, performed the data gathering and analysis, co-interpreted the results, wrote the chapter (with valuable input and comments of the co-authors) and performed the journal correspondence during the publication process.

- **Chapter 3: Patient-specific bolus for range shifter air gap reduction in intensity-modulated proton therapy of head-and-neck cancer studied with Monte Carlo based plan optimization**
  Steven Michiels, Anna Barragán Montero, Kevin Souris, Kenneth Poels, Wouter Crijns, John Aldo Lee, Edmond Sterpin, Sandra Nuyts, Karin Haustermans, Tom Depuydt

  SM co-defined the study methodology, created the treatment plans, performed the data gathering and analysis, co-interpreted the results, wrote the chapter (with valuable input and comments of the co-authors) and performed the journal correspondence during the publication process.

- **Chapter 4: Towards range shifter integrated immobilization for proton therapy: Characterization of 3D printed materials**
  Steven Michiels, Antoine D'Hollander, Nicolas Lammens, Matthias Kersemans, Guozhi Zhang, Jean-Marc Denis, Kenneth Poels, Edmond Sterpin, Sandra Nuyts, Karin Haustermans, Tom Depuydt

  SM co-defined the study methodology, performed the dimension measurements, co-performed the DECT acquisitions and performed the associated calculations of radiologic properties, co-performed the proton and photon beam measurements, performed the data gathering and analysis, co-interpreted the results, wrote the chapter (with valuable input and comments of the co-authors) and performed the journal correspondence during the publication process.

163

- **Chapter 5: 3D printed immobilization for radiotherapy of head-and-neck cancer: A pilot study on patients**
  Steven Michiels, Kenneth Poels, Sandra Nuyts, Tom Depuydt

  SM co-defined the study methodology, wrote the local ethics committee application, performed the design of the 3D printed immobilization devices, co-performed the planning CT and CBCT acquisitions, performed the data gathering and analysis, co-interpreted the results and wrote the chapter (with valuable input and comments of the co-authors).

- **Chapter 6: General discussion & future perspective**
  Steven Michiels, Kenneth Poels, Sandra Nuyts, Tom Depuydt

  SM wrote the chapter (with valuable input and comments of the co-authors).

Conflicts of interest

Curriculum

<u>Short career description</u>

Steven Michiels was born on January 3rd, 1985 in Bonheiden, Belgium. He received Latin-Math as pre-university education at the Sint-Romboutscollege in Mechelen, which he completed in 2003. In 2008, he obtained a Master's degree in Applied Sciences: Energy Engineering with great distinction at the University of Leuven, after which he worked as an operational engineer for three years in the construction industry. In 2012, he obtained a Master's degree in Sciences: Medical Radiation Physics with great distinction at the University of Leuven. Afterwards he worked as a research & development engineer for a major vendor of proton therapy systems. In 2015, he initiated a research project at the department of oncology at the University of Leuven, under the supervision of prof. Depuydt, which resulted in this doctoral thesis.

<u>List of publications</u>

- <u>Michiels S</u>, Poels K, Crijns W, Delombaerde L, De Roover R, Vanstraelen B, Haustermans K, Nuyts S, Depuydt T (2018). Volumetric modulated arc therapy of head-and-neck cancer on a fast-rotating O-ring linac: Plan quality and delivery time comparison with a C-arm linac. Radiotherapy and Oncology 128(3):479-484. doi: 10.1016/j.radonc.2018.04.021.

- <u>Michiels S</u>, Mangelschots B, De Roover R, Devroye C, Depuydt T (2018). Production of patient-specific electron beam aperture cut-outs using a low-cost, multi-purpose 3D printer. Journal of Applied Clinical Medical Physics 19(5):756-760. doi: 10.1002/acm2.12421.

- <u>Michiels S</u>, Barragán AM, Souris K, Poels K, Crijns W, Lee JA, Sterpin E, Nuyts S, Haustermans K, Depuydt T (2018). Patient-specific bolus for range shifter air gap reduction in intensity-modulated proton therapy of head-and-neck cancer studied with Monte Carlo based plan optimization. Radiotherapy and Oncology 128(1):161-166. doi: 10.1016/j.radonc.2017.09.006.

- <u>Michiels S</u>, D'Hollander A, Lammens N, Kersemans M, Zhang G., Denis J-M., Poels K., Sterpin E., Nuyts S., Haustermans K., Depuydt T (2016). Towards 3D printed multifunctional immobilization for proton therapy: Initial materials characterization. Medical Physics 43(10):5392. doi: 10.1118/1.4962033.

- De Roover R, Crijns W, Poels K, <u>Michiels S</u>, Nulens A, Vanstraelen B, Petillion S, De Brabandere M, Haustermans K, Depuydt T (2019). Validation and IMRT/VMAT delivery quality of a preconfigured fast-rotating O-ring linac system. Medical Physics 46(1): 328-339. doi: 10.1002/mp.13282.

- Delombaerde L, Petillion S, <u>Michiels S</u>, Weltens C, Depuydt T (2019). Development and accuracy evaluation of a single-camera intra-bore surface scanning system for radiotherapy in an O-ring linac. Physics and Imaging in Radiation Oncology 11: 21-26. doi: 10.1016/j.phro.2019.07.003

International conference abstracts

- Michiels S, Poels K, Nuyts S, Depuydt T (2020). 3D printed immobilization for head and neck cancer radiotherapy: A pilot study on patients. Accepted for presentation at ESTRO 39, 03-07 April 2020, Vienna, Austria. Poster PO-1623.

- De Roover R, Crijns W, Michiels S, Draulans C, Poels K, Haustermans K, Depuydt T (2019). Focal boost dose escalated prostate SBRT on the Halcyon fast-rotating O-ring linac. Presented at ESTRO 38, 26-30 April 2019, Milan, Italy. Poster PO-0929.

- Michiels S, Poels K, Crijns W, Vanstraelen B, Haustermans K, Nuyts S, Depuydt T (2018). VMAT treatment planning for head-and-neck cancer with the novel fast-rotating linac Halcyon. Presented at ESTRO 37, 20-24 April 2018, Barcelona, Spain. Oral communication OC-0514.

- Michiels S, Mangelschots B, Devroye C, Depuydt T (2018). Use of 3D printing to generate patient-specific electron beam aperture blocks. Presented at ESTRO 37, 20-24 April 2018, Barcelona, Spain. Electronic poster EP-2182.

- Michiels S, Barragán AM, Souris K, Poels K, Crijns W, Lee JA, Sterpin E, Nuyts S, Haustermans K, Depuydt T (2017). Clinical impact of range shifter air gap: Can bolus range shifting improve plan quality in IMPT of head-and-neck cancer? Presented at PTCOG 56, Kanagama, Japan, 08-13 May 2017. Poster PTC17-0242.

- Michiels S, Barragán AM, Souris K, Poels K, Crijns W, Lee JA, Sterpin E, Nuyts S, Haustermans K, Depuydt T (2017). Can bolus range shifting improve plan quality in the IMPT of head and neck cancer? Presented at ESTRO 36, 05-09 May 2017, Vienna, Austria. Electronic poster EP-1590.

- Michiels S, D'Hollander A, Lammens N, Kersemans M, Zhang G, Denis JM, Sterpin E, Nuyts S, Haustermans K, Depuydt T (2016). Poels K, Crijns W, Defraene G, Nuyts S, Haustermans K, Depuydt . (2016). Integration of range shifter in immobilization for proton therapy: 3D printed materials characterization. Presented at PTCOG 55, Prague, Czech Republic, 22-28 May 2016. Poster P-114.

- Michiels S, D'Hollander A, Lammens N, Kersemans M, Poels K, Crijns W, Defraene G, Nuyts S, Haustermans K, Depuydt . (2016). Integrate range shifting in immobilisation for proton therapy: 3D printed materials characterisation. Presented at ESTRO 35, 29 April-03 May 2016, Turin, Italy. Oral communication OC-0164.

Awards

- Best Oral Presentation, Belgian Hadron Therapy Centre Conference (2016)

- Fellowship Emmanuel van der Schueren, Kom Op Tegen Kanker (2016)

Dankwoord

"Alone we can do so little;
together we can do so much."
Helen Keller

Dit proefschrift was niet mogelijk geweest zonder de ondersteuning, de medewerking en de inbreng van vele personen, waarvoor ik mijn oprechte dank en waardering wil betuigen. Vooreerst heb ik de vruchten kunnen plukken van 4,5 jaar lang deel uit te maken van de dienst radiotherapie, waar artsen, fysici en ingenieurs, verpleegkundigen, technologen en dosimetristen, administratieve krachten, laboranten en collega-onderzoekers zich dagelijks inzetten om het leven van zorgbehoevenden te verbeteren. Daarnaast heb ik het geluk om mij in een bevoorrechte privésituatie te bevinden, met liefdevolle en goedhartige ouders, broers & schoonfamilie, volop kansen tot opleiding, een handvol échte vrienden en een partner uit de duizend.

Ook al is het onmogelijk om iedereen expliciet bij naam te noemen, toch wil ik een aantal mensen in het bijzonder bedanken voor hun bijdrage aan dit proefschrift. Tom, bedankt om het intensieve traject, dat een doctoraat ontegensprekelijk is, als promotor met mij bewandeld te hebben. Ik bewonder jouw visionaire en strategische manier van denken op verschillende niveaus, hetgeen meermaals heeft geleid tot ideeën de moeite waard om uit te werken, zo is gebleken. Ik waardeer ten volle jouw bepalende rol op meerdere sleutelmomenten, van het binnenbrengen van opkomende technologieën op de dienst tot het doen landen van een artikel in het juiste wetenschappelijke tijdschrift. Karin, bedankt voor jouw initiële rol in dit doctoraatstraject, in het bijzonder mijn aanwerving en de onderzoeksfinanciering.

Sandra en Kenneth, ik had mij oprecht geen betere co-promotoren voor mij kunnen inbeelden en zal jullie hiervoor nooit genoeg kunnen bedanken. Sandra, ik heb zoveel respect voor de combinatie van klinische/wetenschappelijke competentie, organisatietalent, menselijkheid en nuchterheid die je verpersoonlijkt. Bedankt om mij het gevoel te hebben gegeven steeds bij je terecht te kunnen, zelfs terwijl je eigen werk nooit gedaan is, en bedankt om mijn onderzoek financieel mede mogelijk te hebben gemaakt. Kenneth, het leek je echt nooit teveel om van ideeën te wisselen, om feedback te geven of om mij een portie klinisch denken mee te geven. Ik heb zoveel van jou geleerd en dan nog heb ik een hele weg af te leggen. Bedankt om leren van je toe te laten en om mijn mentor te zijn geweest, waarbij ik steeds de ruimte en het respect voelde voor mijn eigen denkproces en persoonlijkheid.

Prof. Bogaerts, prof. Daelemans, prof. Duprez, prof. van Lenthe and prof. Lomax, thank you for your willingness to serve as Members of the Examination Committee and

"The birds they sang
At the break of day
Start again
I heard them say
Don't dwell
On what has passed away
Or what is yet to be

Yeah the wars they will
Be fought again
The holy dove
She will be caught again
Bought and sold
And bought again
The dove is never free

Ring the bells that still can ring
Forget your perfect offering
There is a crack in everything
That's how the light gets in
That's how the light gets in
That's how the light gets in."

L. Cohen